Towards the Reconstruction of Fiber Tracts in the Human Brain by Means of 3D Polarized Light Imaging

Melanie Dohmen

Dissertation
zur Erlangung des Doktorgrades (Dr. rer. nat.)

im Fachbereich C - Mathematik und Naturwissenschaften
an der Bergischen Universität Wuppertal
Mai 2013

Die Dissertation kann wie folgt zitiert werden:

urn:nbn:de:hbz:468-20131125-120753-1
[http://nbn-resolving.de/urn/resolver.pl?urn=urn%3Anbn%3Ade%3Ahbz%3A468-20131125-120753-1]

Abstract

3D Polarized Light Imaging (PLI) is a method to measure the nerve fiber orientation in thin sections of human post-mortem brains. The birefringence of the myelin sheaths allows the derivation of the in-section direction angle as well as the absolute value of the out-of-section inclination angle. In this thesis, the reconstruction of fiber tracts based on PLI measurements is approached. The development of a suitable simulation framework forms a central point of this work. Furthermore, the inclination sign ambiguity is investigated with additional tilted measurements and the solution is optimized in a Markov Random Field framework. At last, a suitable tractography algorithm is developed for PLI. The results illustrate that random errors in the direction angle can be compensated by a particle filter. The simulation of complex fiber arrangements is able to reproduce important sources of errors, which are approached in the future development of 3D Polarized Light Imaging.

Zusammenfassung

3D Polarized Light Imaging (PLI) ist eine Methode zur Messung der Nervenfaserorientierung in histologischen Schnitten des menschlichen Gehirns. Durch die Doppelbrechung der Myelinscheiden kann die Richtung in der Ebene (Direktion) und die Richtung aus der Ebene heraus (Inklination), welche ohne Vorzeichen bestimmt wird, abgeleitet werden. Diese Arbeit beschäftigt sich mit der Rekonstruktion von Nervenfasertrakten basierend auf PLI-Messungen. Ein Schwerpunkt besteht in der Entwicklung eines Simulationsprogramms. Weiterhin wird die Vorzeichenambiguität des Inklinationswinkels mit zusätzlichen gekippten Messungen untersucht und eine Lösung mit Hilfe eines Markov Random Fields optimiert. Zuletzt wird ein geeignetes Traktographie-Verfahren für PLI entwickelt. Die Ergebnisse zeigen, dass zufällige Fehler des Direktionswinkels durch ein Partikelfilter ausgeglichen werden können. Die Simulation von komplexen Faseranordnungen kann wichtige Fehlerquellen reproduzieren, welche bei der zukünftigen Entwicklung der PLI Methode in Angriff genommen werden.

Danksagung

Da ich im Laufe meiner Doktorandenzeit von vielen Menschen Unterstützung erfahren habe, möchte ich die Gelegenheit nutzen meinen Dank auszusprechen.

Prof. Katrin Amunts danke ich für die Möglichkeit in ihrem Institut ein Thema zu bearbeiten, das so gut zu meinem Hintergrund passt, und für die kontinuierliche Unterstützung, Beratung und Förderung des PLI-Projekts zusammen mit Prof. Karl Zilles.
Weiterhin möchte ich Prof. Uwe Pietrzyk für die Begleitung meiner Promotion als Doktorvater danken. Besonders schätze ich seine Begeisterung für das interdisziplinär angesiedelte Thema zwischen medizinischer Bildgebung, Mathematik und Informatik. Als Betreuer meiner Promotion und Leiter des PLI-Projekts möchte ich mich ganz herzlich bei Dr. Markus Axer für die stetige Unterstützung während meiner Arbeit danken. Die vielen Diskussionen und Gespräche haben meine wissenschaftliche und persönliche Entwicklung begleitet und vorangebracht.
Für die Mitwirkung in der Prüfungskommision möchte ich Prof. Kathrin Klamroth und Prof. Andreas Frommer danken, der außerdem freundlicherweise das Zweitgutachten anfertigte.
Herrn Prof. Gerhard Dikta an der Fachhochschule Jülich möchte ich danken für die Möglichkeit mein Thema vorzustellen und für wichtige Anregungen.
Meinen PLI-Kollegen im Forschungszentrum Jülich danke ich für die kritischen Diskussionen meiner Ideen, die gute Zusammenarbeit, und das angenehme Arbeitsklima, insbesondere Julia Reckfort, Dr. Timo Dickscheid, Hendrik Wiese, Tim Hütz und Martin Schober.

Contents

1 Introduction **1**

2 PLI Basics **7**

2.1 Preparation of Brain Tissue 8
2.2 Polarimeter 9
2.3 Application of the Jones Calculus 11
2.4 Fourier Analysis of the PLI Signal 12
2.5 Calculation of the Inclination Angle 14
2.6 Registration 15
2.7 Vector Fields and Tractography 16

3 PLI Simulation **19**

3.1 Simulation Components 20
3.1.1 Generation of Synthetic Fibers 21
3.1.2 Sampling of a Vector Field from Fibers 21
3.1.3 Simulation of the Tilting Process 23
3.1.4 Simulation of the PLI Signal from a Vector Field . . . 24
3.1.5 Simulation of Noise and Artifacts 26
3.2 Simulation of Homogeneous Tissue 26
3.2.1 Results 29
3.2.2 Discussion 39
3.3 Simulation of Crossing Fibers 39
3.3.1 Results 44
3.3.2 Discussion 47

4 PLI Inclination Sign Ambiguity **53**
4.1 Tilting Setup 54
4.1.1 Comparison of Tilted Images 55
4.1.2 Derivation of the Inclination Sign by Tilted Measurements 55
4.1.3 Reliability of the Derived Inclination Sign 57
4.2 Inclination Sign Enhancement 62
4.2.1 Markov Random Fields for Image Enhancement 62
4.2.2 Design of Data and Smoothness Energy Functions 63
4.2.3 Experiments 71
4.2.4 Results 73
4.3 Discussion 78

5 PLI Tractography **89**
5.1 Tractography Algorithms for DW-MRI 89
5.1.1 Classification of Tractography Algorithms 90
5.1.2 Tractography Based on Bayesian Inference 95
5.2 Tractography Based on 3D-PLI 97
5.2.1 Prior Knowledge About Fiber Tracts 99
5.2.2 Observation Likelihood in PLI Data 99
5.2.3 Particle Filtering 100
5.3 Evaluation on Synthetic Data 102
5.3.1 Results 104
5.3.2 Discussion 107

6 Conclusions and Outlook **117**

Appendix **121**

Bibliography **123**

Chapter 1

Introduction

The human brain is of special interest for both fundamental and clinical researchers. Understanding its structure and function is connected with many expectations. From a clinical point of view, the investigation of brain connectivity is very promising. For many neurological and psychiatric diseases, the exact cause is unknown, e.g. depression, and for most neurodegenerative diseases, there is no cure, e.g. for Parkinson's disease. Often, there are only very limited therapeutic options, e.g. for Alzheimer's disease. An essential aspect of brain structure is the connectivity of cells, which process and transmit information in the brain. In neurosurgery, the knowledge of connecting fiber tracts is extremely important for surgical planning. For these reasons, the idea has been raised to construct a complete network model, to describe the connections in the human brain [51], [15]. This model was named the *connectome* [121], analogously to the full genetic information, the genome. The investigation of the human connectome is also interesting from a methodological point of view. Fundamental research aims to decode one of the most complex phenomena of nature. New concepts for building effective networks in computer technology could be discovered. The exact knowledge of brain connections could enable simulations of the human brain, that could inspire artificial intelligence.

Currently, the information about the connections in the human brain is limited by the available imaging modalities. Therefore, *structural*, *functional* and *effective connectivity* are differentiated [120]. *Structural connectivity*

describes the shape and location of connecting fibers, the fiber architecture. *Functional connectivity* is defined by temporarily correlated brain activity. The description of directed influences is referred to as *effective connectivity*. In addition to different modes of connectivity, the connectome must be assessed on different scales.

On the smallest scale, electron microscopy is able to show cell structures below $1\,\mu$m. Thereby, the locations and the structure of single synapses, where neural information is transmitted, can be examined. This allows the tracking of each axon separately [72]. However, the construction of a whole connectome on the scale of single neurons and synapses seems unfeasible to date [36], because there are approximately 10 billion neurons and 60 trillion synaptic connections [116].

Histological sections can be viewed with light microscopy on a scale of $1 - 100\,\mu$m. Staining of myelin, which surrounds nerve fibers, allows the delineation of major fiber tracts [25]. Myelin staining is the most popular anatomical approach for the validation of other methods, such as magnetic resonance imaging (MRI), today. The compilation of a structure tensor from the image contrast of digitized, myelin stained brain sections allows the automatic derivation of the in-plane fiber direction [85], [24]. For tracking fibers along the determined orientation, the missing out-of-plane fiber orientation is a clear disadvantage.

The tracking of axons beyond single brain sections is possible by dying fiber tracts before sectioning. Suitable substances, called tracers, are injected into the brain and are then transported along fibers [76]. The transport is best in the living brain. Therefore, neuroanatomical tract tracing has been extensively applied in non-humans, for example in the macaque monkey [123], [31], which can be sacrificed in a defined period of time after tracer injection. Apparently, tract tracing cannot be applied to humans in vivo. Only a few studies have applied tract tracing in human post-mortem brains limited by the distance of axonal transport [125], [95]. The resulting histology provides a comparable scale as myelin stains.

On a more course scale, fiber tracts in post-mortem brains can be examined by dissection. Klingler [75] introduced a method, that simplifies the preparation of white matter by freezing. With this technique, which is

commonly referred to as Klingler dissection, major fiber tracts have been described [129], [103]. A major advantage is the conservation of the three-dimensional relationships [105]. However, fiber dissection is not suitable for the study of very thin fiber tracts, also due to the limited number of available human brains. Another disadvantage is the lack of quantitative information.

The only method to assess the orientation of nerve fibers in vivo is diffusion weighted MRI (DW-MRI). By applying a gradient magnetic field, the diffusion of water molecules can be tracked [122]. Even though increasing magnetic field gradients are becoming available, the spatial resolution of DW-MRI in vivo hardly reaches 1 mm [61]. Post mortem, higher resolutions can be achieved, but on small tissue samples only [16]. DW-MRI allows to measure the orientation of water diffusion in biological tissues. In regions with homogeneously orientated nerve fibers, the main direction of water diffusion corresponds to the fiber orientation [12]. However, the diffusion directions provide little validated information about the fiber orientation in case of complex fiber constellations. The most simple approach to describe the measured diffusion orientations is a three-dimensional tensor, which is able to represent a three-dimensional Gaussian distribution [10], [9]. Diffusion Tensor Imaging (DTI) is the most frequently used technique for clinical applications, because the measurement is fast and the tensor representation is simple to process. However, a single tensor is not able to adequately describe mixtures of multiple fiber orientations. Therefore, extended measurement protocols and extended descriptions of fiber orientations have been developed [52]. Orientation distribution functions (ODFs) have become a common representation of mixed fiber orientations, although the measurement and reconstruction methods in the neuroscientific research environment remain heterogeneous. The resolution of DW-MRI is relatively low compared to the investigated structures, which leads to strong partial volume effects. The high availability of MR scanners, also in the clinical environment, have put DW-MRI and thereby the macroscopic scale into the focus of connectome research [15], [51]. However, for the correct interpretation of complex fiber architectures, and the investigation of very small fiber paths, post-mortem methods are needed.

The present work is focussed on 3D-Polarized Light Imaging (3D-PLI),

which is able to reveal the fiber architecture on a microscopic scale ($1-100\,\mu$m). The value of polarized light for the examination of nervous tissue was discovered already a century ago. The inclusion of colored paper in the optical path of polarizing microscopes allowed to color fibers by their orientation [47]. The method was advanced significantly, when the relation between the transmitted light amplitude and the out-of-plane fiber orientation was discovered [5]. The current method of 3D-PLI, that requires histological unstained brain sections and is therefore limited to post-mortem brains, allows the quantitative measurement of fiber orientations in three dimensions on a scale of micrometers [6]. There is a clear potential of 3D-PLI as a bridging technology between microscopic and macroscopic scale. Both scales are needed for a complete understanding of the connectome and it is even more important to find methods to link both scales. It is a major benefit of 3D-PLI, that the in-plane resolution of fiber orientations covers a large range of scales. This opens up the possibility to compare fiber orientations with DW-MRI, as well as to investigate fiber orientations on a scale, that is not accessible by DW-MRI. The reconstruction of a series of brain sections into a three-dimensional volume remains one of the main challenges.

The reconstruction of fiber tracts based on 3D-PLI was first examined by Lindemeyer as a matter of feasibility [87]. The present work aims to improve the reliability and accuracy of reconstructed fiber tracts. The basic setup and analysis concepts are introduced in Chapter 2. In order to identify potentials for improvements, the orientational information needed to be examined closely. This is done by simulation of two representative data sets, which are analyzed extensively in Chapter 3.

The reliability of the measured orientational data is limited by the unknown sign of one vector component. This *inclination sign ambiguity* has not been treated systematically with a tiltable specimen stage before. The disambiguation is a prerequisite for the reliable reconstruction of fiber tracts. Therefore, the inclination sign ambiguity is approached in Chapter 4.

Finally, fiber tracts are reconstructed in Chapter 5. For DW-MRI, a huge variety of tractography algorithms has been developed. Existing algorithms are reviewed regarding their suitability for transfer to PLI, and a strategy

for reconstruction is suggested. The selected approach is able to use the information about accuracy and reliability, that was gathered by simulation in Chapter 3. The results show improved fiber reconstruction, but open issues remain, which are discussed comprehensively. A conclusion and outlook is given in Chapter 6. The progress that this work has achieved is stressed, and several challenges for the future are discussed.

Chapter 2

Fundamentals of 3D Polarized Light Imaging (3D-PLI)

3D Polarized Light Imaging (3D-PLI) is based on the birefringence of nervous tissue. The myelin sheaths, which surround most of the axons of neurons, consist of different kinds of lipids (cholesterol and phospholipids). The anisotropic chemical and molecular constitution of myelin is the reason for its birefringence, which is characterized by an optical axis. This axis is aligned with the orientation of the axon [26]. The birefringent property of nervous tissue was already examined by Göthlin in 1913 [47], later by Schmidt [113], Schnabel [114] and Axer [5]. The polarization state of light is defined by the orientation of the electric field vector. Birefringent materials, such as myelin, change the polarization state of passing light depending on the orientation of the optical axis relative to the incidence of the light. This change can be quantified by the Jones calculus ([70], see Section 2.3) and allows the derivation of the optical axis and thereby the determination of the three-dimensional fiber orientation. For a complete and comprehensive introduction into the physics of birefringence, the reader is referred to textbooks on optics [60]. Polarized light is also used for the examination of collagen in histopathologic tissue samples by polarization microscopy [131] or the examination of skin by optical coherence tomography [112].

In the following, the processing chain will be described (Fig. 2.1). It begins with the preparation and sectioning of a human post-mortem brain

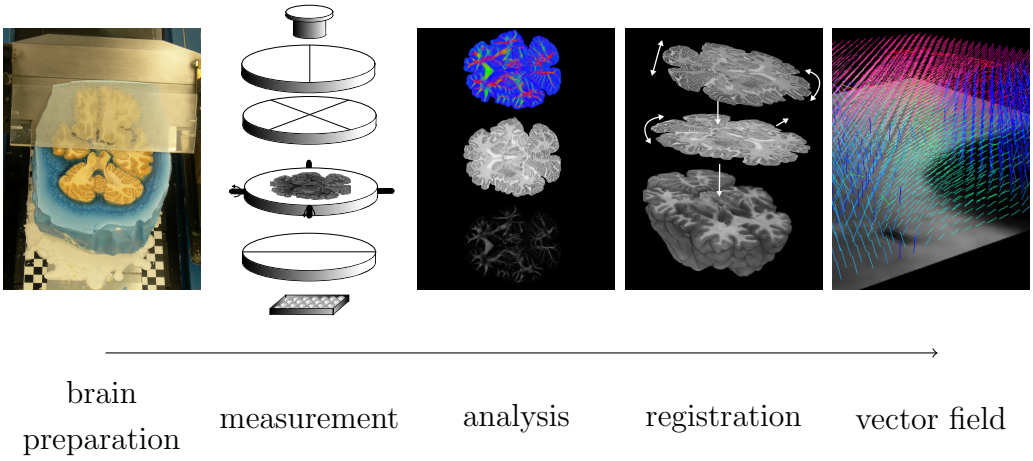

Figure 2.1: Overview of the workflow

(Section 2.1). The brain sections are then measured with a polarimeter (Section 2.2), and analyzed with the Jones calculus (Section 2.3). The inclination angle is calculated (Section 2.5), and the brain sections are aligned. The process of aligning differently transformed images is also called *image registration* (Section 2.6). The resulting 3D vector field of fiber orientations is the basis for the reconstruction of fiber tracts (Section 2.7). Since polarized light imaging is a continuously evolving neuroimaging technique, the workflow presented here is a snap-shot of the current status, which will certainly continue to improve in the future. However, the presented workflow will be termed *standard PLI measurement* and *standard PLI analysis* as a point of reference. When tissue or data is processed differently, this will be indicated in the following chapters.

2.1 Preparation of Brain Tissue

3D-PLI has been developed to analyze the light transmitted through a tissue sample. This demands for sectioning of the tissue into thin slices. Therefore, the current methodology is restricted to the tissue of post-mortem brains and begins with the preparation and sectioning of the post-mortem brain into very thin slices.

In order to conserve birefringence and prevent decay, brain tissue must

be fixated as soon as possible after death. Within 24 hours maximum, the brain is extracted and immersed in formalin (4% formaldehyde solution). Due to the size of human brains, the fixation time should be at least three months. Before sectioning in a cryotome, the brain is immersed in glycerin for cryoprotection or embedded into gelatine. It is frozen to $-80\,^{\circ}\mathrm{C}$, which allows the cryotome to cut sections with a thickness of $50 - 150\,\mu\mathrm{m}$. Each section is melted in water, mounted on a glass slide and dried.

2.2 Polarimeter

The polarimeter consists of a green LED (light emitting diode) grid with a diffusor as a light source, a linear polarizer, a tiltable specimen stage containing the tissue to be measured, a quarter-wave retarder, another linear polarizer and the camera (Fig. 2.2). The direction of polarization of the second polarizer is perpendicular to the direction of the first one and is therefore called analyzer. The retarder allows a disambiguation of the fiber in-plane direction [82], [6]. The polarizing filters, i.e. the polarizer, the quarter-wave retarder and the analyzer can be rotated simultaneously. This allows the acquisition of a series of images for different rotation angles ρ. Additionally, the specimen stage is tiltable in two axes, i.e. in four directions $\psi \in \{N, W, S, E\}$. Tilting changes the fiber orientation in order to solve the inclination sign ambiguity [81], [7], which is elaborated in Chapter 4. The standard PLI measurement acquires 18 images for $\rho_i \in \{0^{\circ}, 10^{\circ}, 20^{\circ}, \ldots, 170^{\circ}\}^*$ in each tilting position, which results in $5 \cdot 18 = 90$ images. Filter inhomogeneities are compensated by calibration with a large series of blank images (measurements without specimen stage). The calibrated series of 18 measurements will be referred to as *PLI image series*.

*Although the sine and cosine function are typically defined on angles given in radians, angles will be given in degrees in most cases, because this seems to simplify spatial understanding.

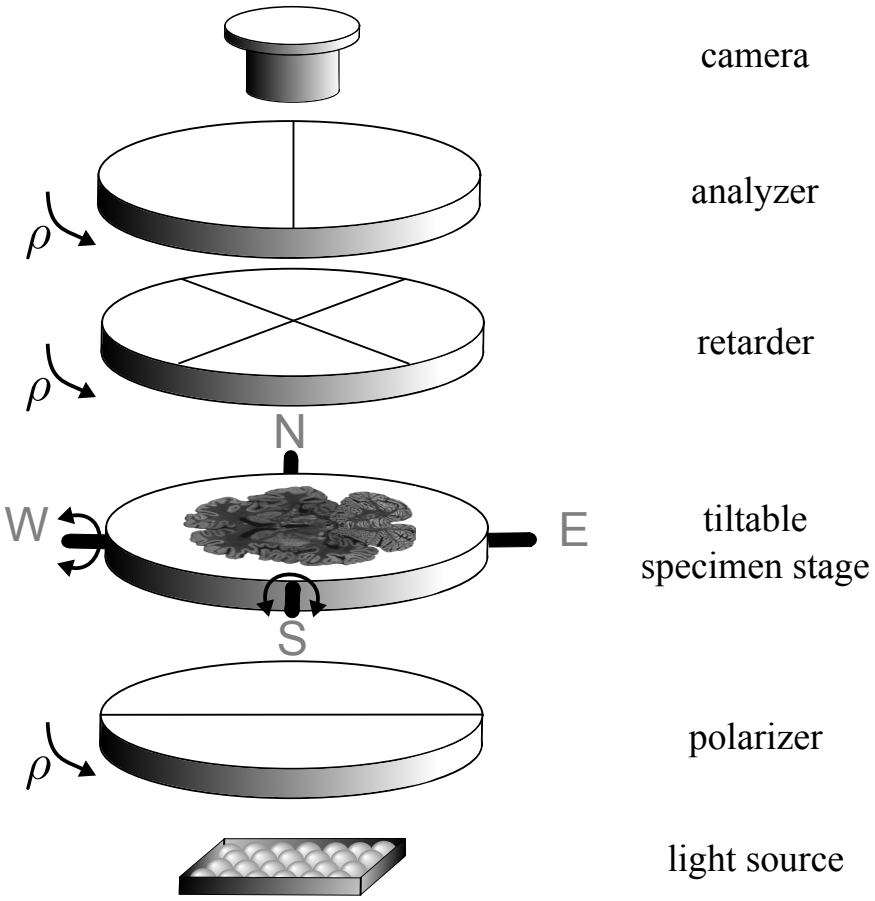

Figure 2.2: Polarimeter setup

2.3 Application of the Jones Calculus

The Jones calculus [70] describes the influence of linear polarizing filters on the electric field vector by expressing each optical element along the optical path as a matrix. The Jones calculus requires fully polarized light. The polarizing filters fulfill this requirement on a very high level. As a simplification, the biological tissue is assumed to act as a single retarder. The formulation of the PLI measurement setup in the Jones calculus is

$$\boldsymbol{E_1} = \boldsymbol{A} \cdot \boldsymbol{R}_{\frac{\lambda}{4}} \cdot \boldsymbol{M} \cdot \boldsymbol{P} \cdot \boldsymbol{E_0} \tag{2.1}$$

where $\boldsymbol{E_0}$ and $\boldsymbol{E_1}$ are the incoming and outgoing electric field vectors, $\boldsymbol{P}$ and $\boldsymbol{A}$ are orthogonal linear polarizers denoted as polarizer and analyzer, $\boldsymbol{R}_{\frac{\lambda}{4}}$ is a quarter-wave retarder and $\boldsymbol{M}$ is a retarder element, that models an in-plane rotated birefringent tissue sample. $\boldsymbol{M}$ is composed as

$$\boldsymbol{M} = \boldsymbol{R}(-(\rho - \varphi)) \cdot \begin{pmatrix} e^{\frac{j}{2}\delta} & 0 \\ 0 & e^{-\frac{j}{2}\delta} \end{pmatrix} \cdot \boldsymbol{R}(\rho - \varphi)\,, \tag{2.2}$$

with j as imaginary unit. The in-plane rotation is defined by the rotation matrix $\boldsymbol{R}(\rho - \varphi)$, depending on the in-plane fiber direction denoted by φ.

$$\boldsymbol{R}(\rho - \varphi) = \begin{pmatrix} \cos(\rho - \varphi) & \sin(\rho - \varphi) \\ -\sin(\rho - \varphi) & \cos(\rho - \varphi) \end{pmatrix} \tag{2.3}$$

The phase difference δ depends on the section thickness d, the uniaxial birefringence Δn, the wavelength λ and the out-of-plane fiber inclination α. The following approximation was shown by Larsen [82]:

$$\delta \approx 2\pi \cdot \frac{d \cdot \Delta n}{\lambda} \cdot \cos^2 \alpha \tag{2.4}$$

The relation of the electric field vectors in the Jones calculus can be transferred to the transmitted light intensity [82]:

$$I(\rho) = I_t \cdot (\frac{1}{2} + r \cdot \sin(2\rho - 2\varphi))\,, \tag{2.5}$$

where I_t[†] is called *transmittance* and $r = \sin(\delta)$ is called *retardation*. The fiber in-plane direction φ can be derived directly from (2.5). The fiber out-of-plane

[†]In previous publications ([6], [7]), the transmittance was denoted by I_0, which was replaced here by I_t. In Chapter 3, I_0 will be needed to refer to the incoming light intensity.

inclination α is correlated with the retardation r [5], following (2.4), which can be rearranged to

$$r = |\sin\delta| = |\sin(\frac{\pi}{2} \cdot d_{\text{rel}} \cdot \cos^2(\alpha))| \,. \tag{2.6}$$

The parameter d_{rel} is an aggregation of the section thickness d, the birefringence Δn and the wavelength λ:

$$d_{\text{rel}} = \frac{4 \cdot \Delta n \cdot d}{\lambda} \tag{2.7}$$

By modeling multiple layers of tissue as multiple retarder elements with the Jones calculus, the PLI signal is simulated in Chapter 3.

2.4 Fourier Analysis of the PLI Signal

The transmitted light intensity $I(\rho)$ can be expressed by a Fourier series [6]:

$$I(\rho) = a_0 + a_1 \sin(2\rho) + b_1 \cos(2\rho) \tag{2.8}$$

Then, the Fourier coefficients a_0, a_1 and b_1 can be calculated from the standard PLI image series with $N = 18$ and $\rho_i \in \{0°, 10°, \ldots, 170°\}$ as a discrete approximation.

$$a_0 = \frac{1}{N} \sum_{i=1}^{N} I(\rho_i) \tag{2.9}$$

$$a_1 = \frac{2}{N} \sum_{i=1}^{N} \sin(2\rho_i) I(\rho_i) \tag{2.10}$$

$$b_1 = \frac{2}{N} \sum_{i=1}^{N} \cos(2\rho_i) I(\rho_i) \tag{2.11}$$

Given the Fourier coefficients and (2.5), the retardation r (Fig. 2.3b), the transmittance I_t (Fig. 2.3c), and the fiber in-plane direction φ (Fig. 2.3a) can be obtained:

$$I_t = 2 \cdot a_0 \tag{2.12}$$

$$\varphi = \frac{1}{2} \operatorname{atan2}(-b_1, a_1) \tag{2.13}$$

$$r = \frac{\sqrt{a_1^2 + b_1^2}}{a_0} \tag{2.14}$$

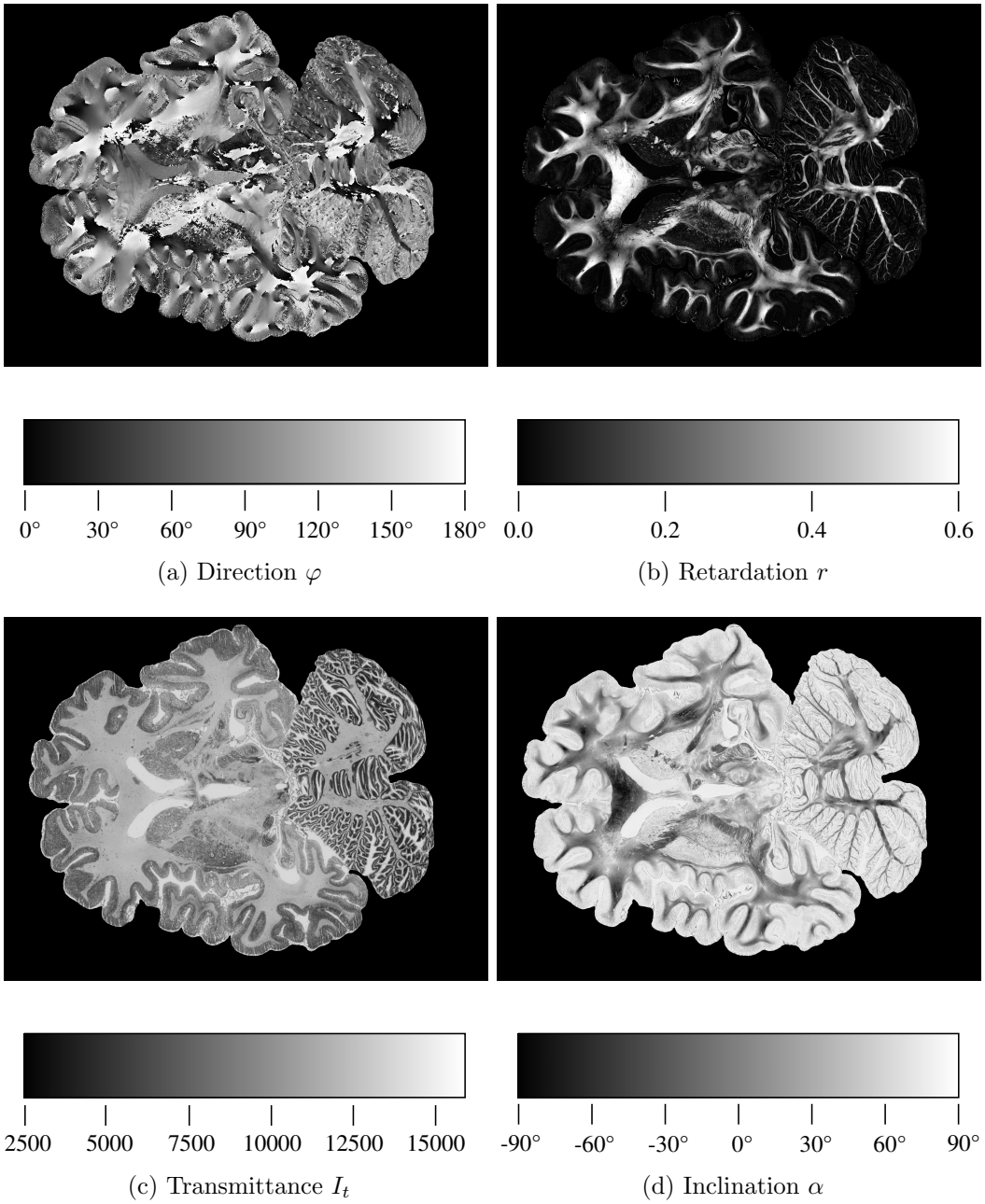

(a) Direction φ (b) Retardation r

(c) Transmittance I_t (d) Inclination α

Figure 2.3: Standard modalities, which are generated by standard PLI analysis

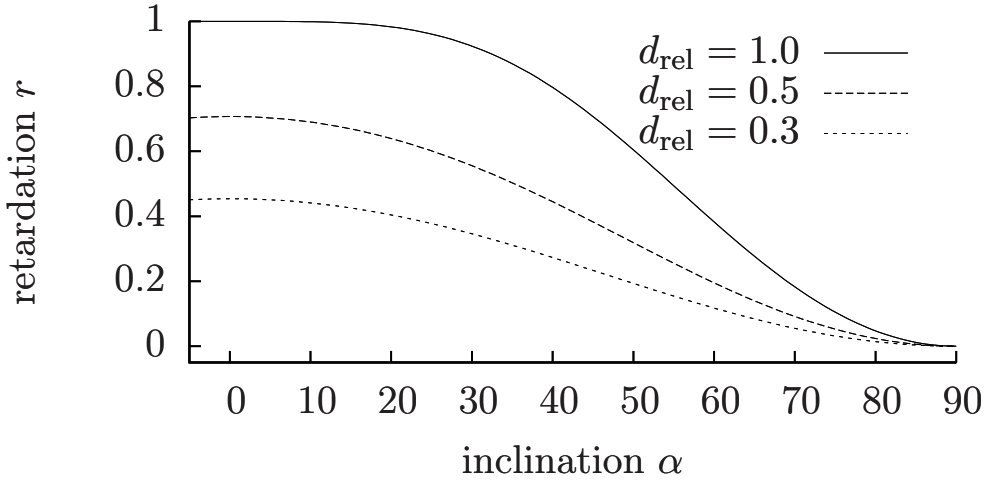

Figure 2.4: Relation between retardation r and inclination α

2.5 Calculation of the Inclination Angle

The fiber out-of-plane inclination angle α (Fig. 2.3d) can be derived from r by (2.6), if d_{rel} is known. In standard PLI analysis, d_{rel} is determined by finding a retardation reference value r_{ref} for flat fibers ($\alpha = 0°$). In a tissue sample that contains a complete distribution of all possible fiber inclination angles, flat fibers can be identified by their maximum retardation. However, the absolute maximum value in the retardation histogram is not a robust reference value, because it is easily distorted by an outlier. Therefore, a special logistic function,

$$f(x) = \frac{a + bx}{e^{\frac{x-c}{d}} + 1}, \tag{2.15}$$

which models a symmetric decrease, is fitted into the tail of the retardation histogram [6]. This fit allows the objective and reproducible estimation of a retardation reference value $r_{\text{ref}} = c$, and thereby determines the relating function between retardation and inclination depending on d_{rel} (see (2.6)).

$$d_{\text{rel}} = \frac{2 \arcsin(r_{\text{ref}})}{\pi} \tag{2.16}$$

The non-linear relation between retardation and inclination is strictly decreasing for $d_{\text{rel}} \leq 1.0$ (Fig. 2.4, see also [6] Fig. 4a). When the inclination

angle is very low or very high, the retardation value corresponding to different inclination angles is almost the same. Therefore, very small errors in the retardation value are amplified, when the inclination angle is derived from the retardation. This motivates the following excursus on error propagation regarding the inclination angle.

Error propagation When performing experiments, the measurement device naturally introduces random errors into the measured quantities. Typically, these errors are distributed according to the normal distribution, and the uncertainty of the measured variable can be estimated by the empirical standard deviation. If the variable of interest is not measured directly, but derived from a measured variable by a non-linear function, then the uncertainty of the measured variable must be propagated to the derived variable of interest [48].

The retardation r is measured with an approximately normal distributed random error $\Delta r = 0.006$, which was determined in 30 repeated measurements. But the inclination angle α is derived from r by (2.6), and therefore, the uncertainty of α must be propagated from $r \pm \Delta r$ to $\alpha \pm \Delta\alpha$. A linearized approximation of $\Delta\alpha$ is

$$\Delta\alpha = \sqrt{\left(\frac{\partial\alpha}{\partial r}\Delta r\right)^2} \tag{2.17}$$

The differentiation of (2.6) yields

$$\frac{\partial\alpha}{\partial r} = \frac{-1}{(\arcsin(r_{\text{ref}}) - \arcsin(r)) \cdot \arcsin(r) \cdot (1 - r^2)}\,. \tag{2.18}$$

In Section 3.2, the uncertainty of the inclination angle α will be examined in detail by simulations (see Fig. 3.11a).

2.6 Registration

During the sectioning process, each section is mounted onto a specimen stage. The position and rotation of consecutive sections on their specimen stages is variable. Additionally, the tissue may be deformed. In order to reconstruct the series of sections into a consistent three-dimensional volume,

these transformations and distortions must be corrected. This is a typical task in medical image registration [62]. For the registration of histological sections such as PLI images, it is advantageous to take photos of the brain block surface before sectioning. Blockfaces can be registered onto their consecutive sections more easily, because there are no sectioning distortions. The registered blockface images then serve as references for the registration of the histological sections [30]. The simultaneous registration of histological and blockface images seems to be superior to sequential registration [99], [38], but has not been implemented for PLI images, yet [98]. Special care must be taken when applying the determined transformations to PLI images, since they contain directional information. The directional information must be adjusted accordingly.

2.7 Vector Fields and Tractography

Currently, the registration is applied to pairs of fiber angles (φ, α), which are then converted to unit vectors.

$$\begin{aligned} x &= \cos\alpha \cdot \cos\varphi \\ y &= \cos\alpha \cdot \sin\varphi \\ z &= \sin\alpha \end{aligned} \tag{2.19}$$

The fiber orientation is ambiguous in respect to 180°, i.e. the direction of signal transport in a fiber cannot be detected. Therefore, the unit vectors are normalized such that $y > 0$. For visualization, two types of color-coded fiber orientation maps (FOMs) have established themselves (Fig. 2.5). The RGB (x = red, y = green, z = blue) FOM is a common colored representation of diffusion tensor data [59]. The HSV (φ = hue, α = saturation, 1 = value) FOM is used in addition, because it shows a very good contrast on single sections and is able to distinguish symmetric orientations on the x-y-plane with respect to the x- and the y-axis.

By composing all registered sections of unit vectors to a three-dimensional vector field, the basis for the reconstruction of fiber tracts in the human brain is provided. The generation of fiber paths from a fiber orientation

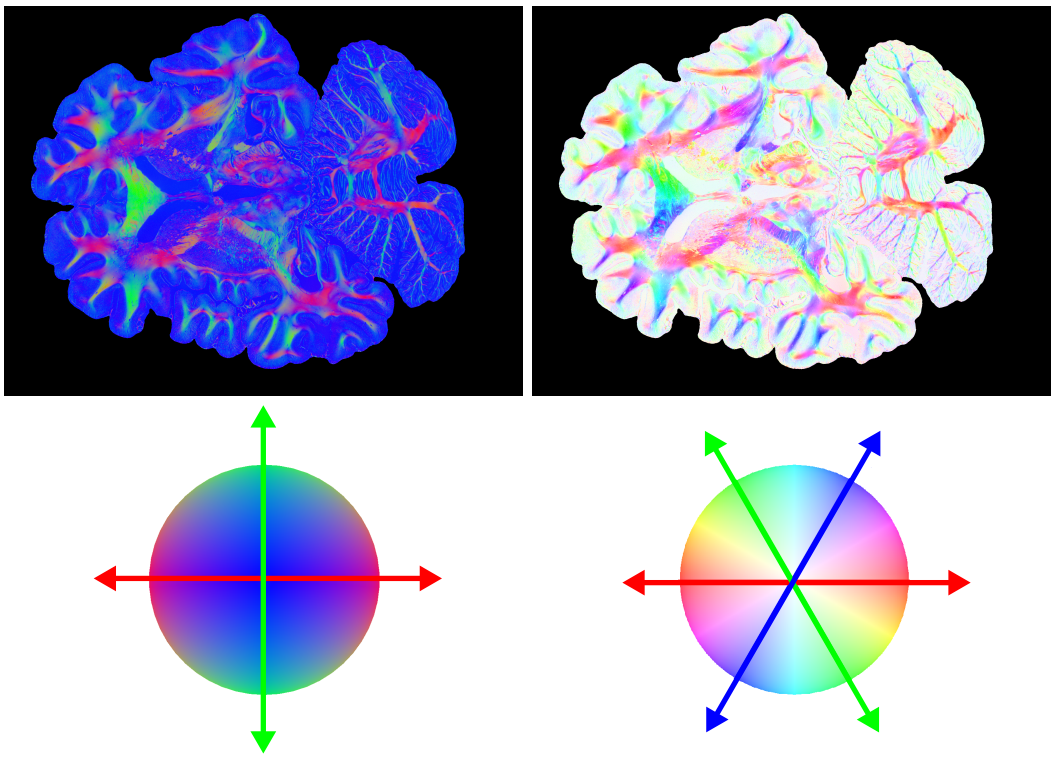

(a) RGB FOM (b) HSV FOM

Figure 2.5: The unit vectors, that are derived from fiber in-plane direction φ and out-of-plane inclination α determined by standard PLI analysis, are presented as color coded fiber orientation maps (FOMs). There are two common color-codings, RGB (red, green, blue) and HSV (hue, saturation, value).

vector field is dealt with in Chapter 5. There is no standard approach to PLI tractography, however the first tractography results of PLI made use of streamline methods [87], [7].

Chapter 3

PLI Simulation

As explained in the previous chapter, 3D-Polarized Light Imaging is based on some simplifications regarding the tissue sample. The potential eerrors and limitations that arise thereby have not been investigated before. This is also due to the lack of an alternative method, that can quantify the fiber orientation of nervous tissue in a similar scale. Moreover, human and animal nervous tissue is very complex and an appropriate phantom serving as a standard for PLI is not available, yet. Thus, the only possibility to compare the fiber orientations measured by PLI with a known underlying fiber model is by implementation of a simulation framework. This is a popular approach to assess errors, also in diffusion weighted magnetic resonance imaging (DW-MRI) [84].

There are three sources of errors, that can be derived directly from the simplifications made for PLI analysis. First, errors are expected to appear when fiber orientations are mixed inside one measured pixel. Second, errors are expected from assuming the wrong tissue properties, i.e. the imprecise determination of the relative section thickness d_{rel}. Third, the camera sensors are noisy. This might seem insignificant, but there are certain tissue properties and fiber arrangements that severely decrease the PLI signal. Thereby the derived fiber orientations become sensitive to this noise. The influence of these sources of errors will be evaluated systematically by simulation in this chapter.

Another major issue, that is approached by simulation, is the validation

of software tools and algorithms of PLI analysis. The previously presented analysis pipeline is very complex and every bug or failure may introduce errors into the final vector field. The correct interpretation of the resulting vector field crucially relies both on the knowledge about measurement errors and the elimination of potential bugs in the analysis pipeline.

In this chapter, a simulation framework for PLI is presented, that reproduces the main parts of the PLI measurement process. It consists of the generation of synthetic fibers, the sampling of a vector field, the tilting of the vector field, the computation of a synthetic PLI image series, and the simulation of blurring, resampling effects and sensor noise. The simulation tool is explained in detail in Section 3.1. Two fiber arrangements were realized to investigate the aforementioned sources of errors. In Section 3.2, a homogeneous tissue sample was simulated, consisting of uniformly distributed fiber orientations. In this data set, the influence of sensor noise and estimation of tissue properties can be examined for all possible fiber orientations. The second data set, which is presented in Section 3.3, consists of a crossing fiber arrangement. This demonstrates the effects mixed fiber orientations. The synthetic fiber crossing arrangement is compared with real measurements of fiber crossings in the optic chiasm of a hooded seal (*Cystophora cristata*). The true fiber arrangement of the optic chiasm in this species is not known precisely. The interpretation of the measurements is discussed by comparison with simulations.

3.1 Simulation Components

The concept of simulation for PLI was first described in a master's thesis by Lindemeyer [87]. The core of his simulation scheme was a rebinning procedure, that allowed the mixture of more than one fiber orientation. The idea of sampling a synthetic fiber at a higher resolution to mix fiber orientations is conserved here, but the mixture of fiber orientations is now transferred to the simulation of the optical path. An overview of the four main simulation components is shown in Fig. 3.1. The simulation of a fiber arrangement begins with the generation of synthetic fibers in a three-dimensional volume. These fibers must be transformed into a three-dimensional vector field. For

homogeneous fiber orientations, that are not produced by single fibers, the vector field may be generated directly as a starting point. The tilting process is simulated optionally by tilting each vector without moving it. The Jones calculus is the theoretical basis for the calculation of a PLI signal of birefringent, homogeneous tissue sections. For simulation of inhomogeneous tissue, a section is modeled as a series of homogeneous sections with different birefringence properties. In this way, tissue with mixed fiber orientations can be simulated. Similar approaches for the simulation of the interaction of polarized light in biological tissues have been presented [130], [43]. As a last step, the measurement of the PLI signal with a camera is simulated by blurring, resampling and adding noise. These four main steps will be described in more detail in the following sections.

3.1.1 Generation of Synthetic Fibers

The simulation tool is able to construct synthetic fibers in a fixed three-dimensional volume. The image size $s = (s_x \times s_y \times s_z)$ is defined in pixels, with s_z restricted to 1. This represents the size of a measured tissue section. The spacing $m = (m_x \times m_y \times m_z)$ can be chosen freely in physical units. For a typical brain section captured by the camera of a large-area polarimeter this yields $s = (2776 \times 2080 \times 1)$ pixels and $m = (64\,\mu\text{m} \times 64\ \mu\text{m} \times 100\,\mu\text{m})$. Synthetic fibers are represented as a series of consecutive coordinates. The fiber radius r_f is chosen globally for the complete fiber arrangement, which currently restricts the simulated fiber arrangements to those with equally thick fibers.

3.1.2 Sampling of a Vector Field from Fibers

In order to generate a vector field from synthetic fibers, the aforementioned image size is upsampled to a spacing of $m' = (m'_x \times m'_y \times m'_z)$. This implies $m'_x \leq m_x$, $m'_y \leq m_y$, and $m'_z \leq m_z$ and leads to an increased image size $s' = (s'_x \times s'_y \times s'_z)$. The fiber radius r_f defines the neighborhood of voxels that is assigned with this fiber's orientation. The fiber orientation of a pixel i is determined by a fiber path segment $\overline{f_i^1 f_i^2}$, if either the distance between

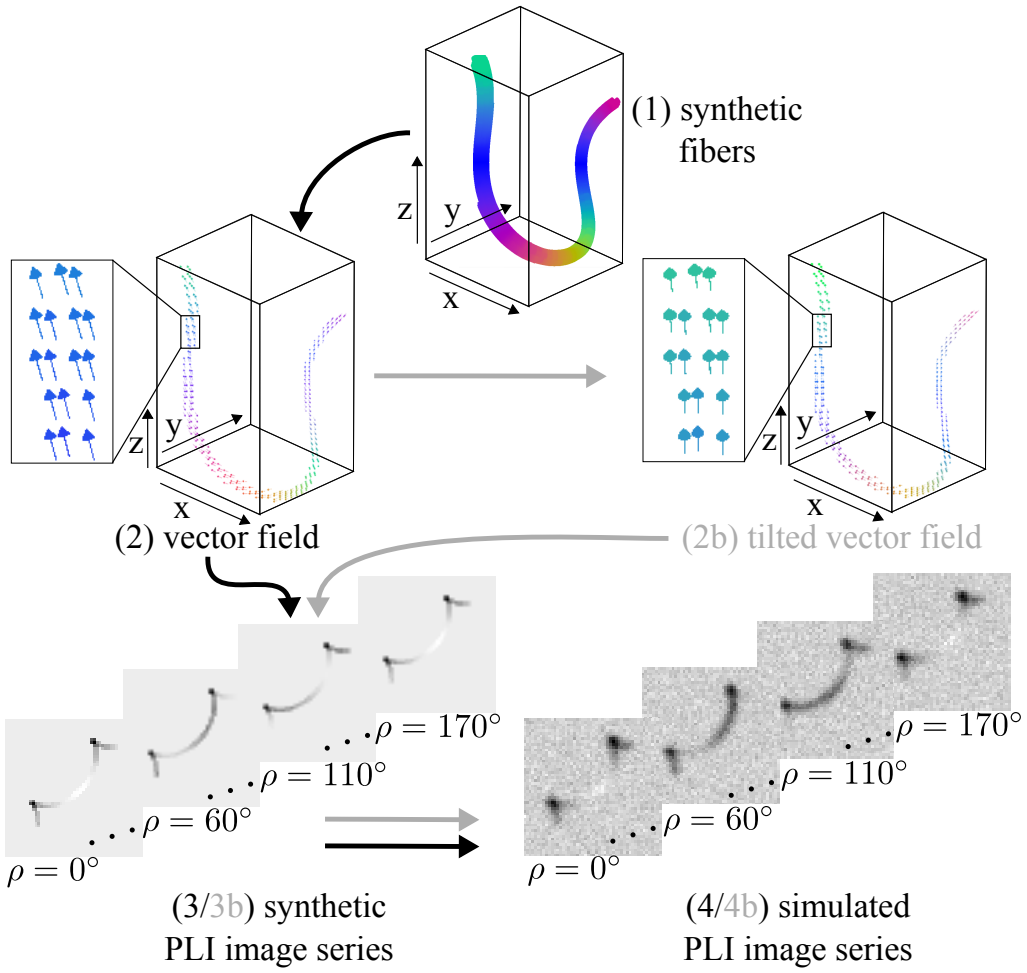

Figure 3.1: Four main steps of the PLI measurement process are reproduced by the simulation. (1) Synthetic fibers are created in a given volume. (2) A vector field is sampled with high resolution. (2-4b) Optionally, a tilted vector field is created and processed. (3) The orientations are mixed along the z-axis to obtain a synthetic PLI image series, which consists of a series of 18 gray images. (4) The measurement is simulated by resampling, blurring and addition of noise.

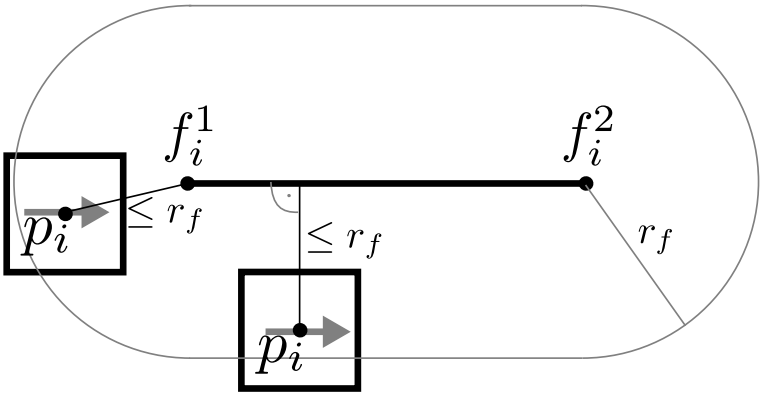

Figure 3.2: The vector field at pixel i with center p_i is derived from the synthetic fiber path coordinates f_i^1 and f_i^2 that are located the closest to p_i. Only pixels with p_i located inside the fiber radius r_f are assigned with a fiber orientation parallel to $\overline{f_i^1 f_i^2}$.

the center p_i of i and the line segment $\overline{f_i^1 f_i^2}$ or the distance to one of the fiber path coordinates is lower than the fiber radius r_f as illustrated in Fig. 3.2.

3.1.3 Simulation of the Tilting Process

The tiltable specimen stage in the PLI measurement setup, which is introduced in Chapter 2, enables the measurement of the tissue sample in four tilted positions in addition to the flat, untilted position. Therefore, the orientation of the fiber is changed by the performed tilting. This change can be calculated analytically by knowledge of the tilting axis and the tilting angle. This is further elaborated in Section 4.1.2. Tilting causes two changes to the PLI measurement, that occur simultaneously. First, the position of the tissue sample changes such that a specific point on the tissue sample is imaged in a different position in the flat and each tilted image. Second, the fiber orientation changes such that a specific point on the tissue sample produces a different PLI signal, i.e. the measured light intensity is changed. In the simulation presented here, only the latter kind of change has been reproduced. In standard PLI analysis, tilted images are untilted by back-transformation of the perspective transform. The application of a perspective transformation

is not realized in the scope of this work, but would allow the observation of errors that arise in the determination and application of the perspective transformation. Therefore, the untilting step must be omitted in the analysis of simulated PLI measurements. Tilting is simulated optionally, generating four additional simulated PLI image series.

3.1.4 Simulation of the PLI Signal from a Vector Field

The PLI signal is a sequence of light intensity values, which is generated by rotating the polarizing filters in the polarimeter. The standard PLI measurement generates a series of 18 gray images, one for each rotation angle $\rho \in \{0°, 10°, 20°, \ldots, 170°\}$. The relation between the incoming electric field vector $\boldsymbol{E_0}$, the assumed fiber orientation expressed as a pair of angles (φ, α), and the resulting electric field vector $\boldsymbol{E_1}$ can be derived from the Jones Calculus as shown in Section 2.3. To model the experimental situation, the simulation has been extended in order to create an optical path through a series of fiber orientations. When traversing the upsampled, synthetic vector field along the z-axis, multiple fiber orientations are passed. Therefore, the single retarder, that models the fiber orientation of a homogeneous tissue sample, is replaced by a series of retarders, that models the optical path through an inhomogeneous tissue sample. This can be formulated by the Jones calculus as

$$\boldsymbol{E}_1 = \boldsymbol{A} \cdot \boldsymbol{M}_{i_1} \cdot \boldsymbol{M}_{i_2} \cdot \ldots \cdot \boldsymbol{M}_{i_3} \cdot \ldots \cdot \boldsymbol{M}_{1/m_z} \cdot \boldsymbol{R}_{\frac{\lambda}{4}} \cdot \boldsymbol{P} \cdot \boldsymbol{E}_0 \,, \tag{3.1}$$

where $\boldsymbol{E}_1$ and $\boldsymbol{E}_0$ are the outgoing and incoming electric field vectors, and $\boldsymbol{M}_i$ is the retarder resembling the i^{th} fiber. The quarter-wave $\boldsymbol{R}_{\frac{\lambda}{4}}$, and the analyzer $\boldsymbol{A}$, which is a linear polarizer orthogonal to the linear polarizer $\boldsymbol{P}$, correspond to the polarimeter in Section 2.2. This simulation setup is illustrated in Fig. 3.3. Each retarder $\boldsymbol{M}_i$ is defined by the in-plane direction φ_i and out-of-plane inclination α_i of the fiber i. This leads to

$$\boldsymbol{M}_i = \boldsymbol{R}(-(\rho - \varphi_i)) \cdot \begin{pmatrix} e^{\frac{j}{2}\delta_i} & 0 \\ 0 & e^{-\frac{j}{2}\delta_i} \end{pmatrix} \cdot \boldsymbol{R}(\rho - \varphi_i) \tag{3.2}$$

with

$$\boldsymbol{R}(\rho - \varphi_i) = \begin{pmatrix} \cos(\rho - \varphi_i) & \sin(\rho - \varphi_i) \\ -\sin(\rho - \varphi_i) & \cos(\rho - \varphi_i) \end{pmatrix} \tag{3.3}$$

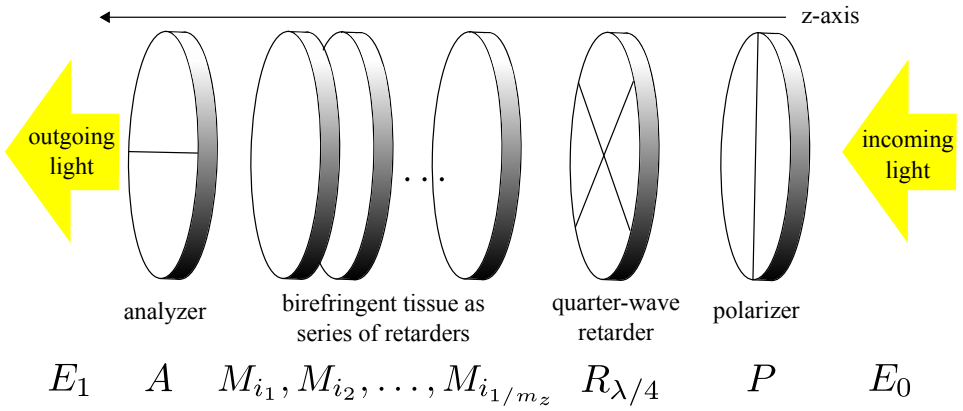

Figure 3.3: The simulation combines different fiber orientations along the z-axis of the synthetic vector field to a PLI signal by modeling each fiber orientation as an optical retarder element.

and

$$\delta_i = 2\pi \cdot \frac{d \cdot \Delta n_i}{\lambda} \cdot \cos^2 \alpha_i \tag{3.4}$$

The incoming electric field vector is defined by the incoming light intensity I_0*.

$$\boldsymbol{E}_0 = \begin{pmatrix} \sqrt{I_0} \\ 0 \end{pmatrix} \tag{3.5}$$

The outgoing light intensity I_1 is calculated from the outgoing electric field vector E_1 and the attenuation, which depends on the attenuation coefficient μ, the upsampled z-spacing m_z' and the number of voxels n in the z-axis, which contain a fiber. The size $m_z' \cdot n$ represents the thickness of the complete simulated tissue section.

$$I_1 = e^{-\frac{1}{2}\mu \cdot m_z' \cdot n} \cdot \langle \boldsymbol{E}_1, \boldsymbol{E}_1^* \rangle \tag{3.6}$$

In accordance with the standard PLI measurement, the simulation generates a series of 18 light intensities for each rotation angle $\rho \in \{0°, 10°, \ldots, 170°\}$ and each pixel $i \in (s_x' \times s_y')$ in the x-y-plane of the upsampled volume of the vector field.

*In previous publications [6], [7], the transmittance was denoted by I_0. However, I_0 is typically used to denote the incident light in the Beer-Lambert law, which is applied in (3.6). To avoid confusions, the transmittance is denoted by I_t.

3.1.5 Simulation of Noise and Artifacts

In order to obtain realistic measurement data, noise and blurring must be scaled correctly. In a preliminary study, the optical resolution was determined as approx. 128 μm opposed to a pixel size of 64 μm in a large-scale polarimeter. This reflects a blurring effect, which can be modeled by convolution with a Gaussian filter. A radius of $\sigma_r = 128\,\mu$m corresponds to the determined resolution. After blurring, resampling to the final pixel spacing m is performed. In addition to blurring, the camera sensors add white noise to the resulting image intensities. The level of noise $\sigma_c = 150$ a.u. was detected by repeated measurements of a typical specimen stage. For simulations, the standard normal distribution $\mathcal{N}(0, \sigma_c)$ was sampled and added to each pixel.

3.2 Simulation of Homogeneous Tissue with Uniformly Distributed Orientations

For the simulation of homogeneous tissue, the generation of synthetic fibers is not necessary, because each voxel is supposed to contain exactly one fiber population. Instead of creating a synthetic fiber arrangement, the fiber orientations were assigned directly to a vector field with a size of one pixel along the z-axis ($s_z = s'_z = 1$). In this way, there is no mixture of fiber orientations. This simulation allows to investigate the effect of sensor noise and imprecise estimation of the retardation reference value r_{ref} (Section 2.5). The simulated homogeneous tissue data set contains all possible fiber orientations. The fiber orientations were not sampled uniformly along the surface of a sphere, but uniformly in terms of their in-plane direction φ and out-of-plane inclination α. The direction φ was varied along the circumference of a circle, and the inclination α was varied along the square of the radius from $-90°$ to $90°$ (Fig. 3.4). This resulting vector field is smooth (Fig. 3.5). The vector field was upsampled by two in the x-y-plane but not along the z-axis. This complies with the assumption of homogeneous tissue properties and fiber orientations. The image spacing and the incident light were chosen according to a large-area polarimeter. The retardation reference value r_{ref} was set to 0.6. The incident light I_0 was set to 15700. Both values can be derived from

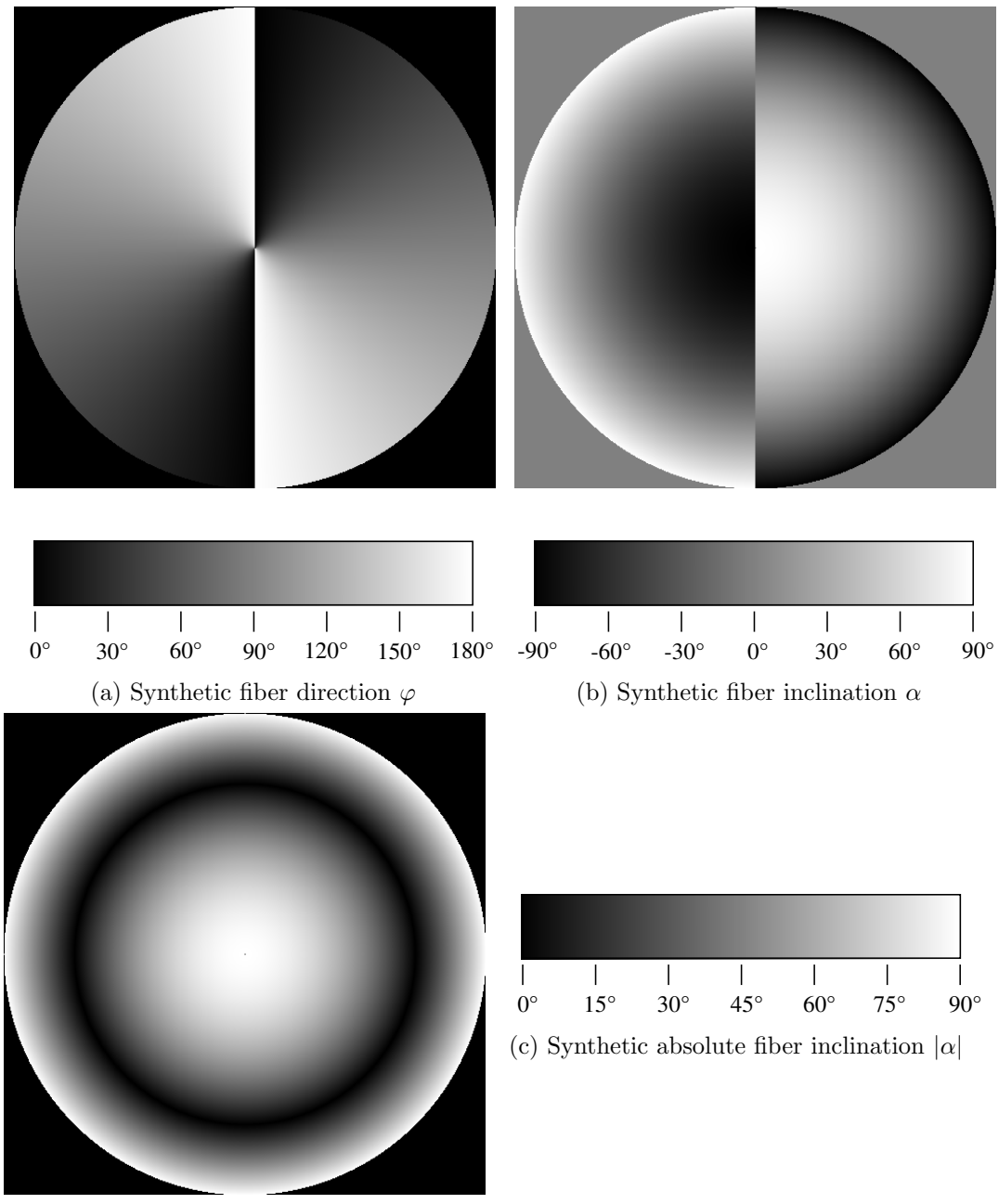

(a) Synthetic fiber direction φ

(b) Synthetic fiber inclination α

(c) Synthetic absolute fiber inclination $|\alpha|$

Figure 3.4: The distribution of fiber orientations was chosen uniformly along the circumference and uniformly along the square of the radius of a circle for in-plane direction φ and out-of-plane inclination α respectively.

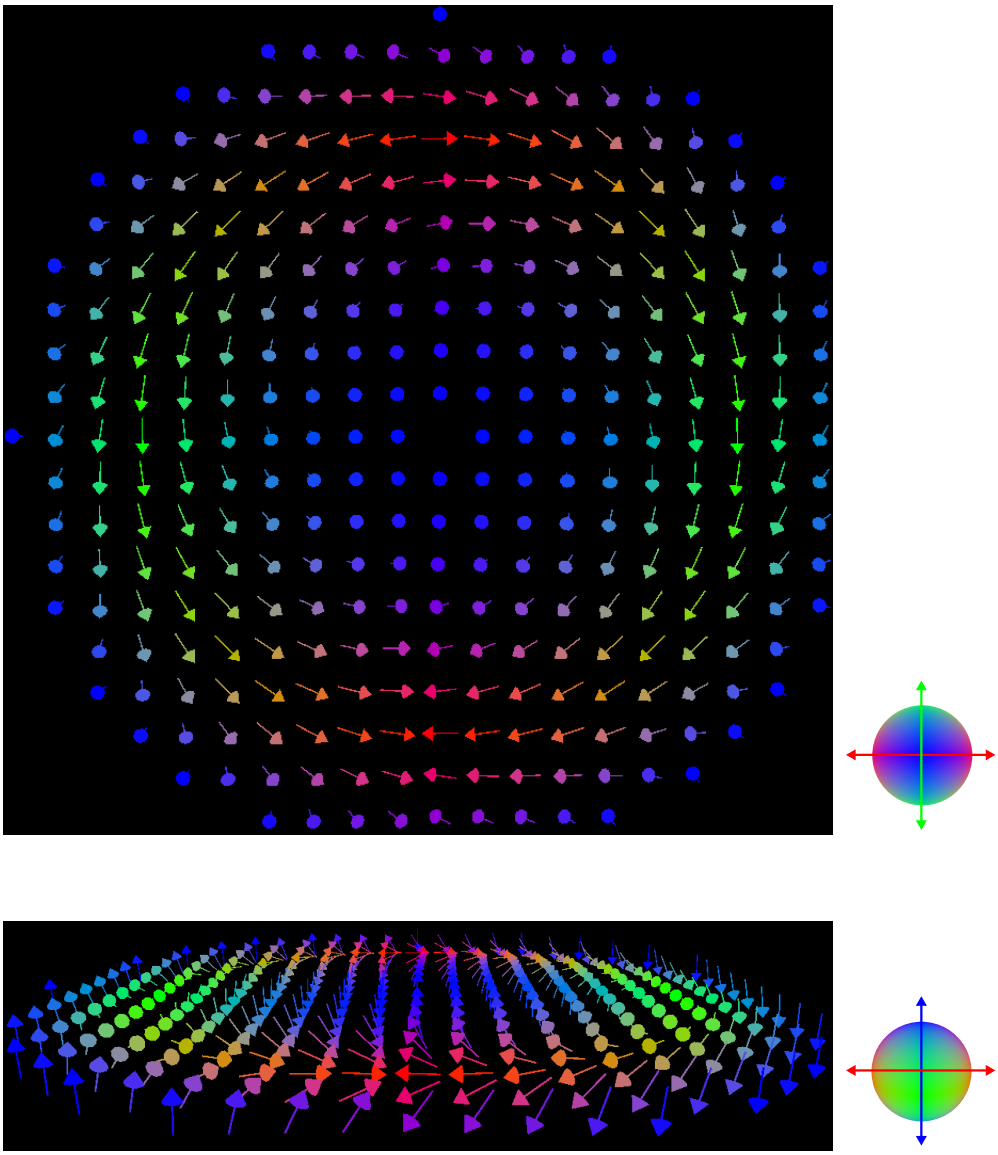

Figure 3.5: The continuous change of the fiber orientation is shown more clearly in a vector visualization with a reduced number of vectors.

Table 3.1: Simulation parameters of homogeneous tissue sample with uniformly distributed fiber orientations

parameter name	symbol	value	unit
image size x	s_x	500	px
image size y	s_y	500	px
image size z	s_z	1	px
pixel spacing x	m_x	64	μm
pixel spacing y	m_y	64	μm
pixel spacing z	m_z	100	μm
upsampled pixel spacing x	m'_x	32	μm
upsampled pixel spacing y	m'_y	32	μm
upsampled pixel spacing z	m'_z	32	μm
incident light	I_0	15 700	a.u.
reference retardation	r_{ref}	0.6	
attenuation	μ	1.5	$\frac{1}{\text{mm}}$
blurring radius	σ_r	128	μm
sensor noise	σ_c	150	a.u.

measurements of typical brain sections (Fig. 3.6). A list of all parameters used for the simulation of the homogeneous tissue sample with uniformly distributed orientations is summarized in Table 3.1. The simulation generates a PLI image series, which was processed by standard PLI analysis. The derived fiber orientations can be compared to the synthetic fiber orientations used for simulation.

3.2.1 Results

In the first step, a PLI images series was simulated from the synthetic vector field as described in Section 3.1.2 and Section 3.1.4. The change of light intensities follows the fiber in-plane orientation, as shown for a selection of rotation angles $\rho \in \{0°, 40°, 80°, 120°\}$ in Fig. 3.7. The PLI image series was analyzed as described in Chapter 2. The parameters transmittance I_t,

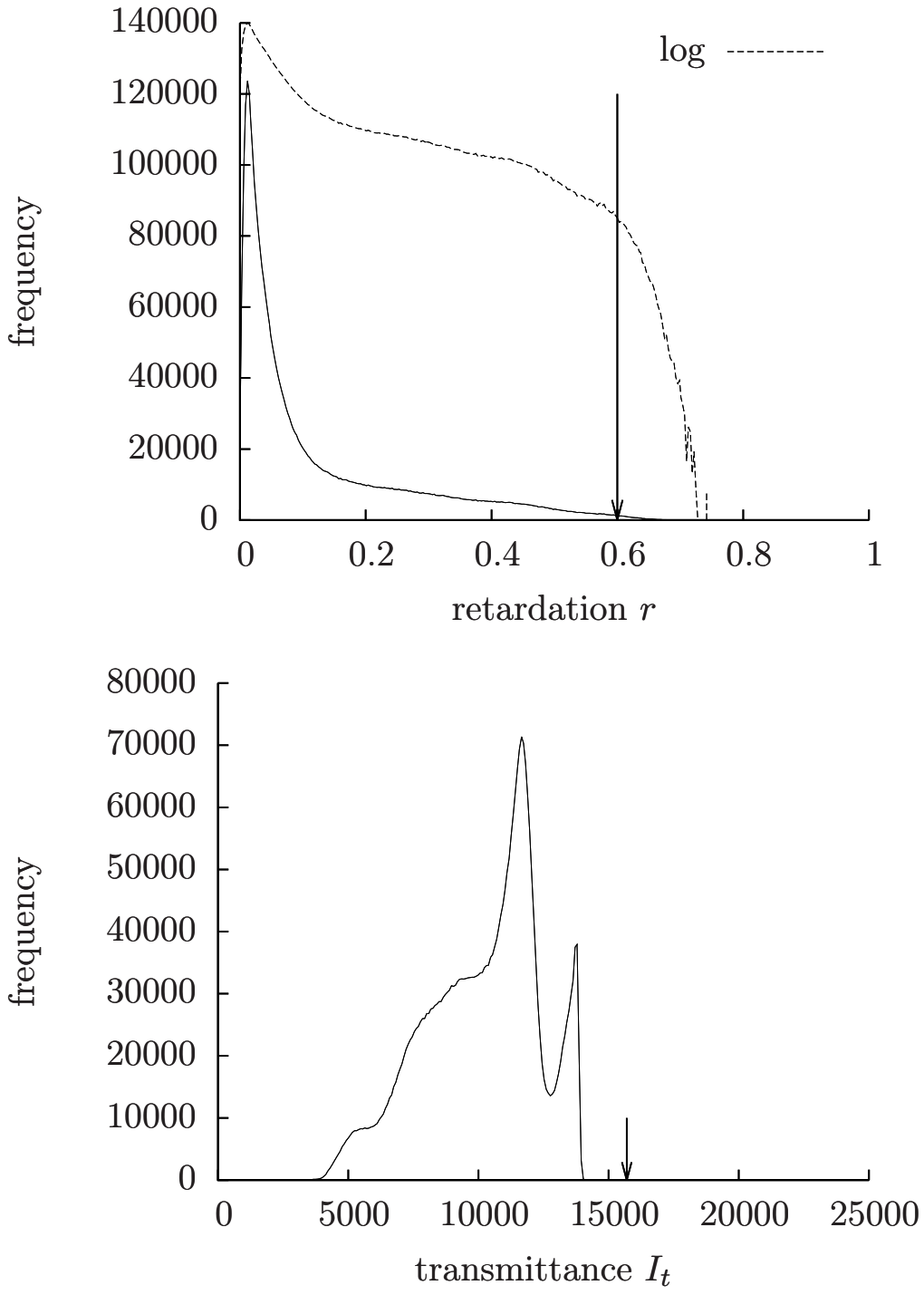

Figure 3.6: The histograms show the distribution of retardation and transmittance values in the brain sections shown in Fig. 2.3. A retardation reference value $r_{\text{ref}} = 0.6$ is typical. The incident light should be chosen higher than typical transmittance values. For simulation, $I_0 = 15700$ was chosen.

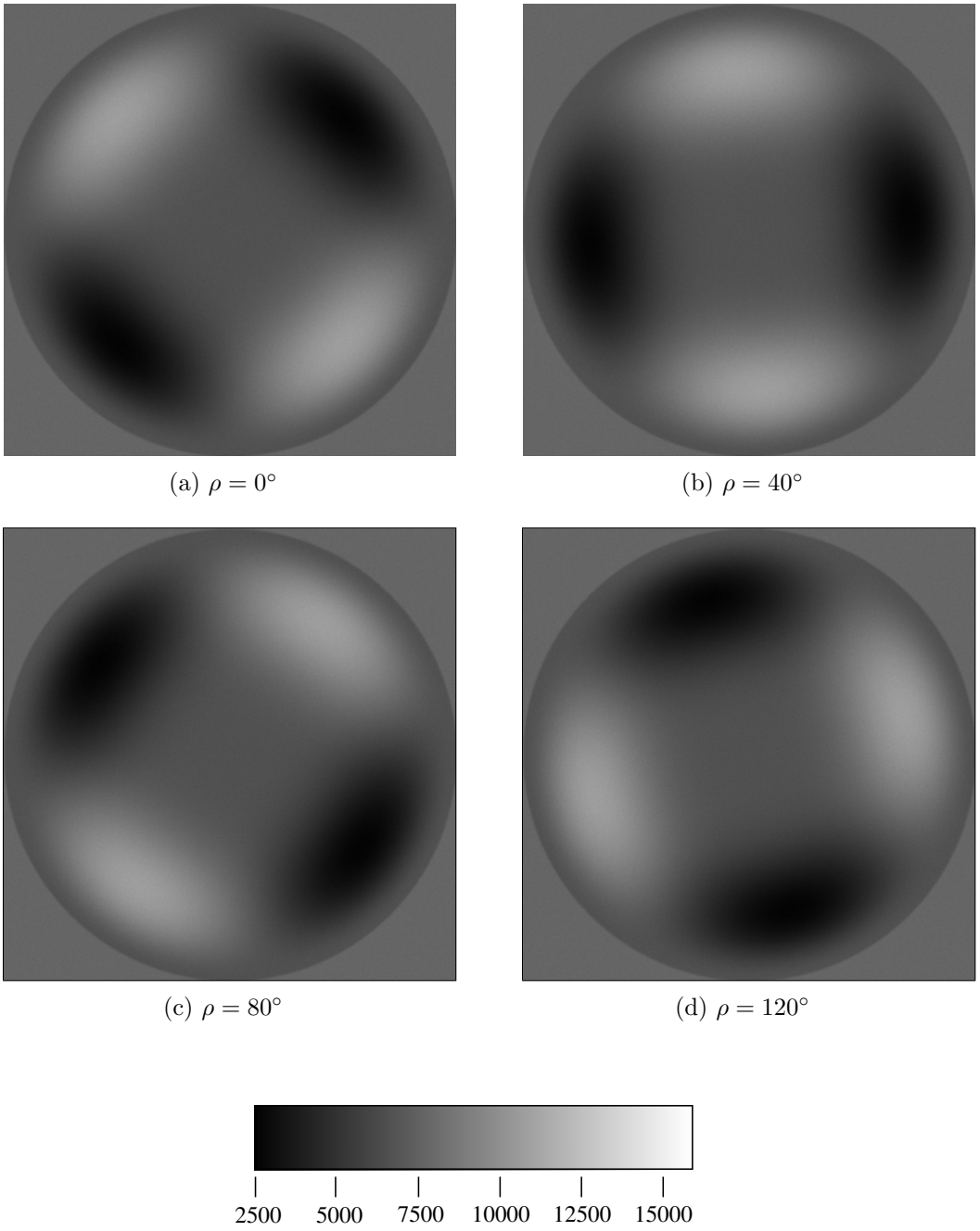

(a) $\rho = 0°$ (b) $\rho = 40°$

(c) $\rho = 80°$ (d) $\rho = 120°$

Figure 3.7: The simulation generates a PLI image series of 18 gray images for a series of rotation angles ρ of the polarizing filters. A selected set is shown here. The light intensity changes along the circular fiber direction.

retardation r, and direction φ were obtained and are shown in Fig. 3.8(a)-(c). The retardation reference value $r_{\text{ref}} = 0.602418$ is determined as described in Section 2.5. Thereby, the absolute inclination angle $|\alpha|$ can be derived (Fig. 3.8d). The comparison of true and simulated fiber orientations reveals very small differences for a large majority of fiber orientations. The images in Figs. 3.4(a), (c) and 3.8(c),(d) resemble each other strongly. A numerical comparison of the true and simulated fiber orientation angles is illustrated in Figure 3.9. This comparison reveals large discrepancies where the fiber inclination is steep. This is especially striking for the fiber direction, which shows deviations no larger than 5° in combination with inclination angles $|\alpha| < 60°$, but turns out to be assigned arbitrary values for $|\alpha| > 80°$. However, the deviation of the in-plane fiber direction φ does not depend on the value of φ itself, which is not shown here. The fiber inclination is disturbed no more than 2° for intermediate values, but up to 10° at both edges of the range of absolute inclination values. In these regions, the simulated absolute inclination values are not distributed normally around the true absolute inclination values. Low inclination values are systematically overestimated by the simulation. There is a diagonal cluster of low inclination values, that are assigned 0° in the simulation. The same applies inversely to high inclination values. They are systematically underestimated. There is no diagonal cluster, but analogously all simulated inclination angles are limited to values below 90°.

The determination of a retardation reference value r_{ref} in order to derive d_{rel} is a crucial step for the analysis of the inclination angle. As explained in Section 2.5, the automatic fit assumes a certain distribution of retardation values. Therefore, the retardation reference value must be determined manually, if a different distribution is found. This is the case, if the examined brain section is not complete, or does not contain a sufficient number of in-plane fibers. In the sample examined here, blurring and sensor noise gave rise to retardation values of up to 0.63. Before simulation, the retardation was limited to 0.6. Therefore, a maximum deviation of ± 0.03 in the choice of the reference value seems realistic. The simulated inclination angles analyzed with biased retardation reference values are compared to the true inclination angles in Fig. 3.10. With a biased retardation reference value r_{ref}, there are

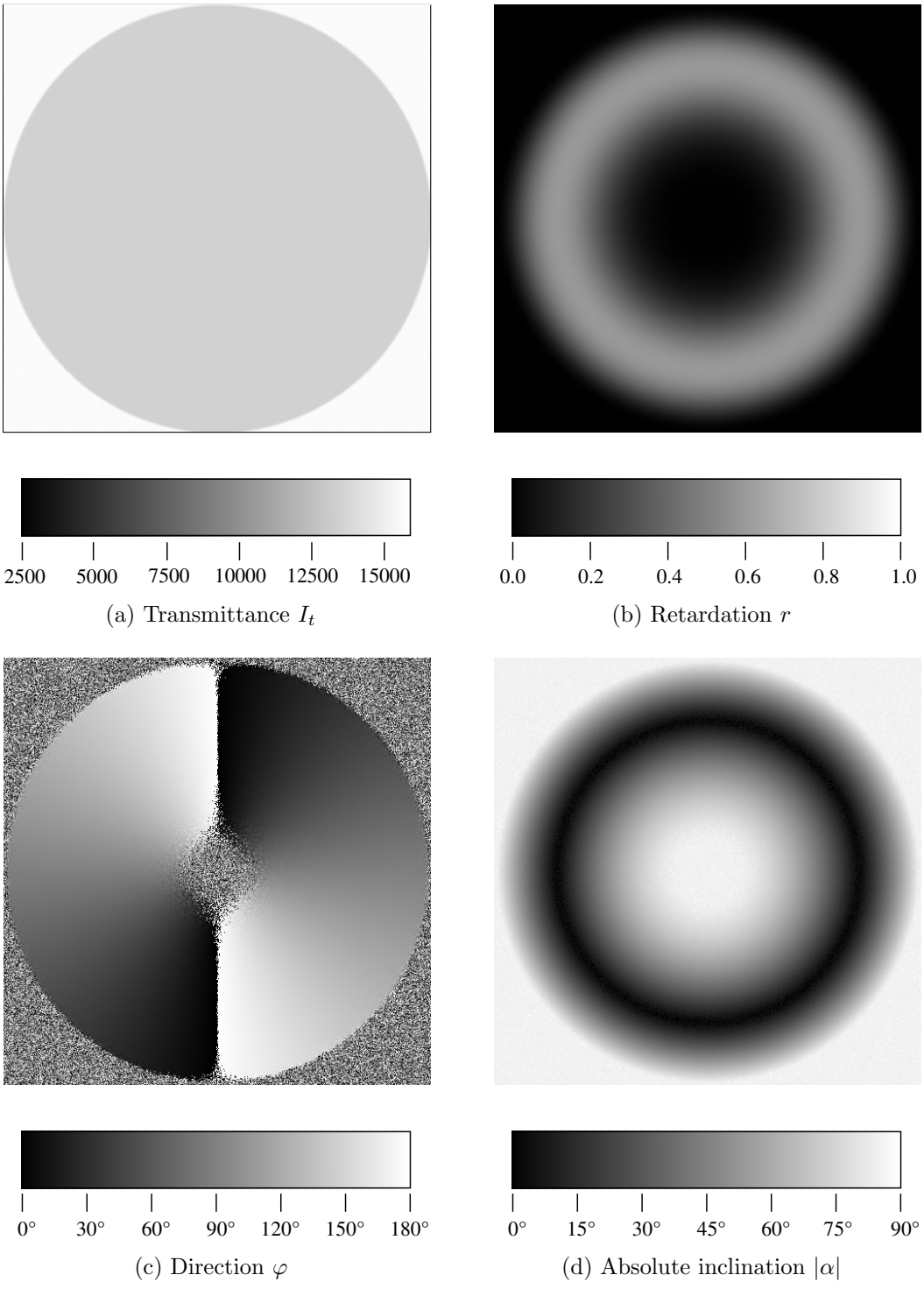

(a) Transmittance I_t (b) Retardation r

(c) Direction φ (d) Absolute inclination $|\alpha|$

Figure 3.8: The above parameters were obtained by standard PLI analysis. The reference value r_{ref} needed for the calculation of the absolute inclination $|\alpha|$ was obtained automatically from the histogram of the retardation image as described in Section 2.5.

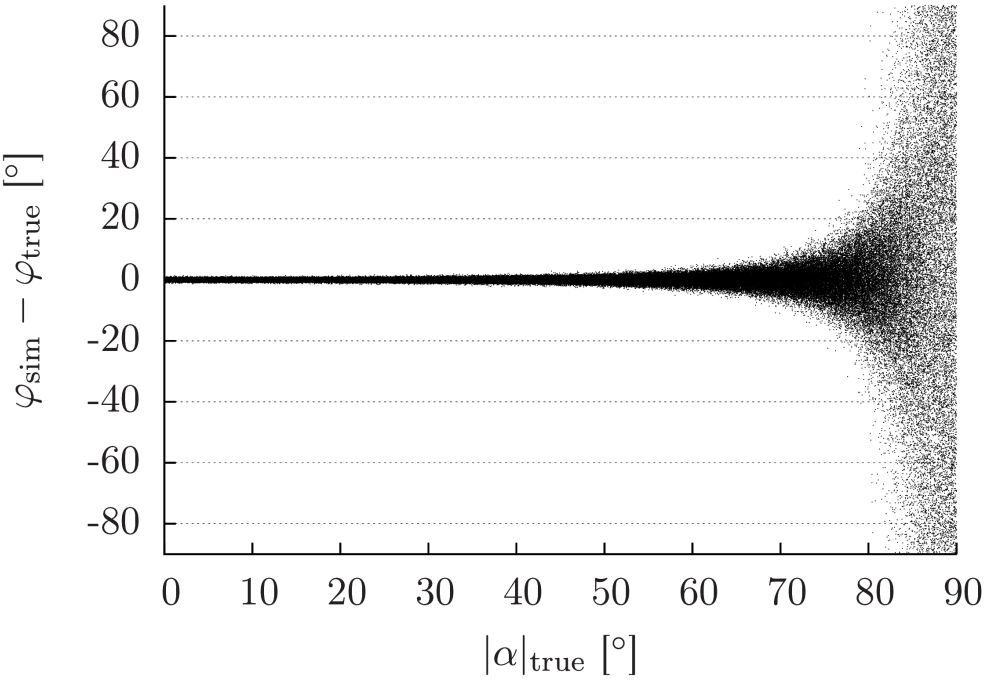

(a) Reliability of the in-plane direction φ

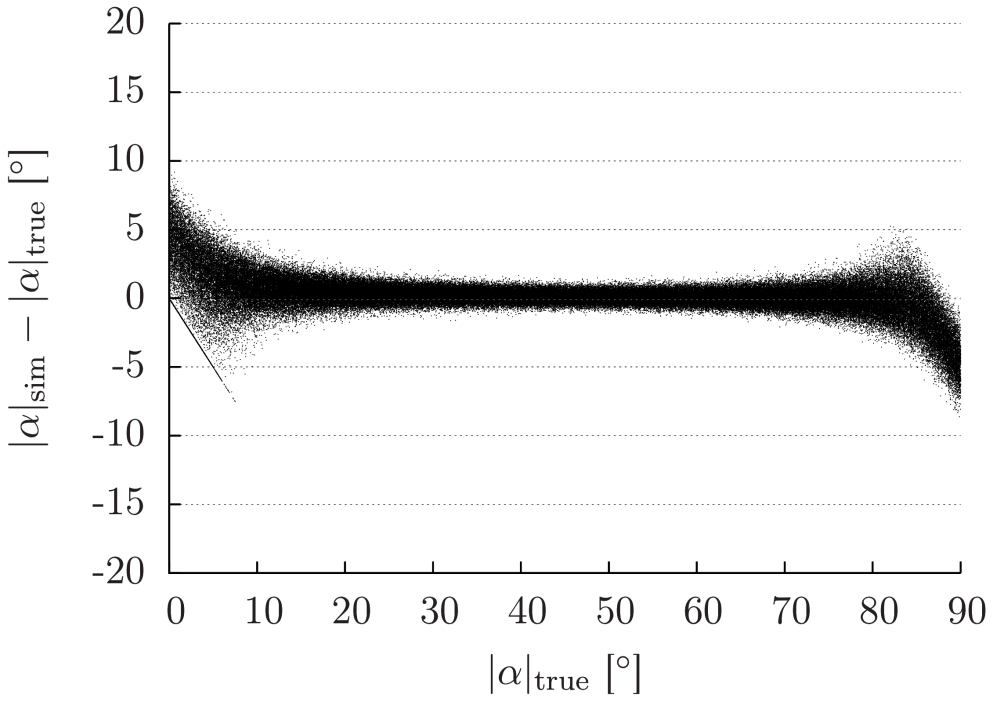

(b) Reliability of the absolute out-of-plane inclination $|\alpha|$ with automatically determined retardation reference value $r_{\mathrm{ref}} = 0.602418$

Figure 3.9: The fiber orientations that were determined from the simulated data set are compared with the true orientation angles, that the simulated data set based on. The reliability of both fiber orientation angles strongly depends on the absolute inclination angle $|\alpha|$.

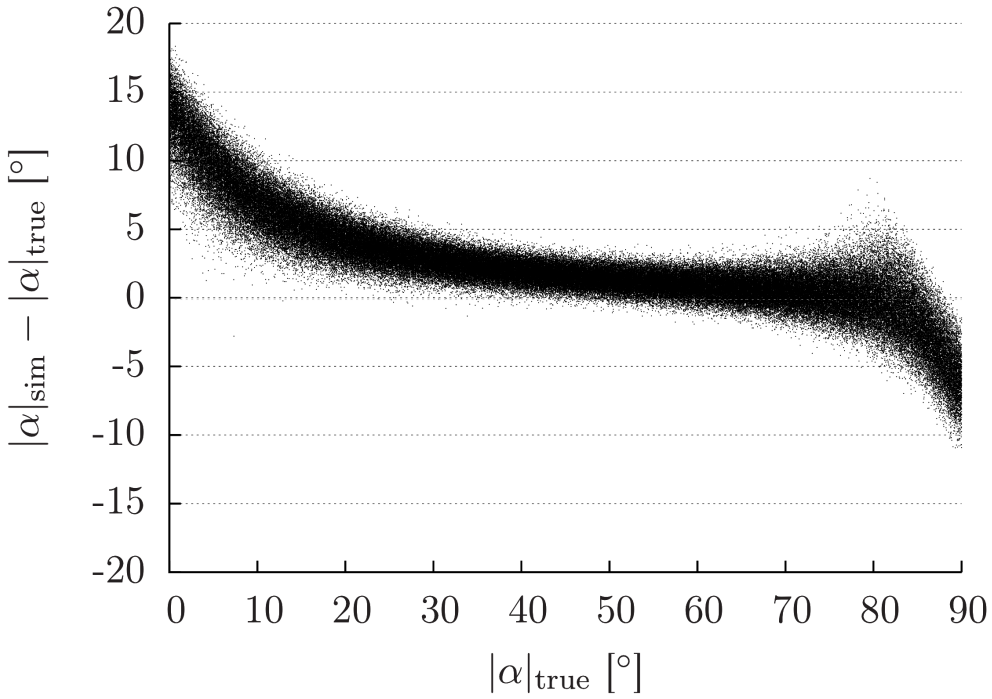

(a) Retardation reference value $r_{\text{ref}} = 0.63$

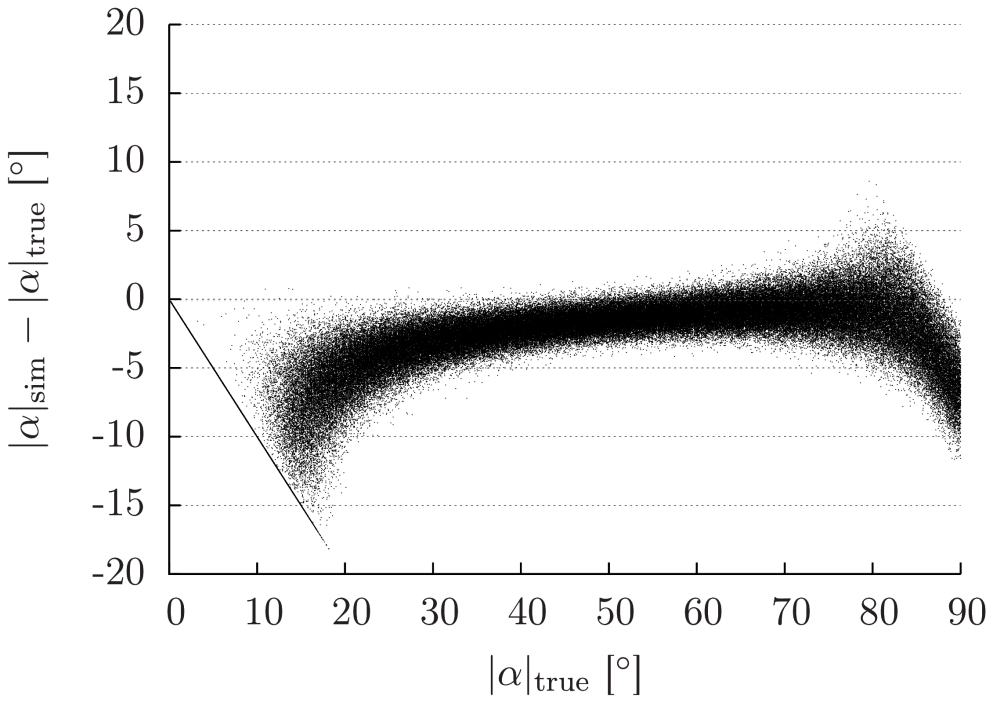

(b) Retardation reference value $r_{\text{ref}} = 0.57$

Figure 3.10: The choice of the correct retardation reference value is crucial for the correct interpretation of the inclination angle. The true reference value, which was chosen for simulation was 0.6. If the reference value is chosen too high, the absolute inclination angles below 50° are systematically overestimated. The simulation yields inclination angles of approx. 12° for actually flat fibers. The errors are also systematically biased by a reference value that is chosen too low. Then, fibers below 50° are underestimated. Practically all fibers that are inclined by less than 10° are assigned a simulated absolute inclination angle $|\alpha|_{\text{sim}} = 0°$. This is visible as a diagonal cluster.

considerable deviations between the true and the simulated inclination angle of up to almost 20°. In particular, the mean of the simulated inclination values systematically deviates from the true value, such that practically none of the true inclination angles $|\alpha| < 40°$ is conserved through the simulated measurement. The empirical standard deviation can be calculated from the simulated data set by evaluating small intercepts of the inclination angles. This empirical error is comparable to the propagated error determined in Section 2.5. A mutual plot of the propagated error and the empirical error are shown in Fig. 3.11a. In the calculation of the propagated error in Section 2.5, the uncertain choice of a reference value r_{ref} was not considered. Therefore, the calculation of the propagated error $\Delta\alpha(r, r_{\mathrm{ref}})$ is adjusted here. The absolute inclination angle $|\alpha|$ is derived from the retardation reference value r_{ref} as

$$|\alpha| = \arccos\left(\sqrt{\frac{\arcsin(r)}{\arcsin(r_{\mathrm{ref}})}}\right) . \tag{3.7}$$

The propagated error $\Delta\alpha(r, r_{\mathrm{ref}})$ is then calculated as

$$\Delta\alpha = \sqrt{\left(\frac{\partial\alpha}{\partial r}\right)^2 \cdot \Delta r + \left(\frac{\partial\alpha}{\partial r_{\mathrm{ref}}}\right)^2 \cdot \Delta r_{\mathrm{ref}}} \tag{3.8}$$

with

$$\frac{\partial\alpha}{\partial r_{\mathrm{ref}}} = \frac{1}{\sqrt{\left(1 - \frac{\arcsin(r)}{\arcsin(r_{\mathrm{ref}})}\right) \cdot (1 - r_{\mathrm{ref}}^2) \cdot 2\arcsin(r_{\mathrm{ref}})}} . \tag{3.9}$$

For comparison with the empirical errors for $r_{\mathrm{ref}} = 0.57$ and $r_{\mathrm{ref}} = 0.63$, Δr_{ref} was set to 0.015, and $\Delta r = 0.006$ was chosen as in Section 2.5. The results of both approaches of error analysis are illustrated in Fig. 3.11b. The empirical error shows a stronger increase towards flat fibers, but then falls below the propagated error for inclinations angles below approx. 15° and 10° respectively. There is a very abrupt decrease of the empirical error for a reference value $r_{\mathrm{ref}} = 0.57$, which cannot be observed for a reference value $r_{\mathrm{ref}} = 0.63$.

3.2.2 Discussion

The errors introduced by sensor noise and blurring were investigated by simulation of a homogeneous tissue sample covering the full range of possible fiber directions. The results allow the estimation of errors by comparison of the true underlying orientation and the orientation computed by simulation of the measurement process and standard PLI analysis. In conclusion, the errors strongly depend on the out-of-plane fiber inclination and therefore are very sensitive to the choice of an appropriate retardation reference value r_{ref}. The errors of the simulated inclination angles are not distributed symmetrically around the true value, if the reference value is biased. If r_{ref} is chosen correctly, at the edges of the range of inclination angles, the errors are not distributed symmetrically either. These systematic errors seem to be caused by the non-linear relation between the retardation r and the absolute inclination angle $|\alpha|$ (see (2.6)). In particular, the inclination angle is not defined for retardation values larger than the retardation reference value due to the arc cosine function. In standard PLI analysis, these retardation values are set to the retardation reference value r_{ref}, and thereby the inclination angle is artificially set to 0°. This obviously causes the empirical error to decrease for very low inclination angles. Similarly, the absolute inclination angle is limited to angles of maximally 90°, because the range of retardation values is positive by definition (see (2.14)). These boundary conditions are not and can not be included in the error propagation approach. This seems to be the reason why the error predicted by error propagation does not fully agree with the results of simulation, especially towards the edges of the range of inclination values. However, the error propagation approach provides a description of the error in a closed-form expression. This could be convenient for the development of stochastic tractography algorithms (see Chapter 5).

3.3 Simulation of a Crossing Fiber Arrangement

In this section, a crossing fiber arrangement is simulated in order to observe the mixture of two defined fiber orientations (Fig. 3.12a). This fiber arrangement

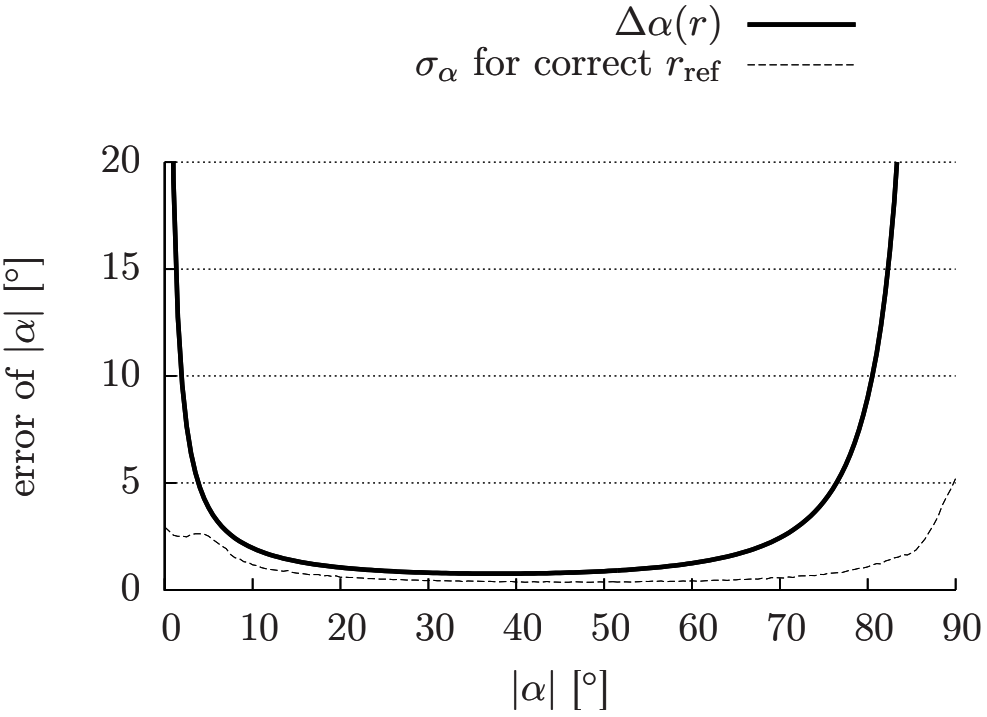

(a) The retardation reference value is set to the correct value $r_{\mathrm{ref}} = 0.6$.

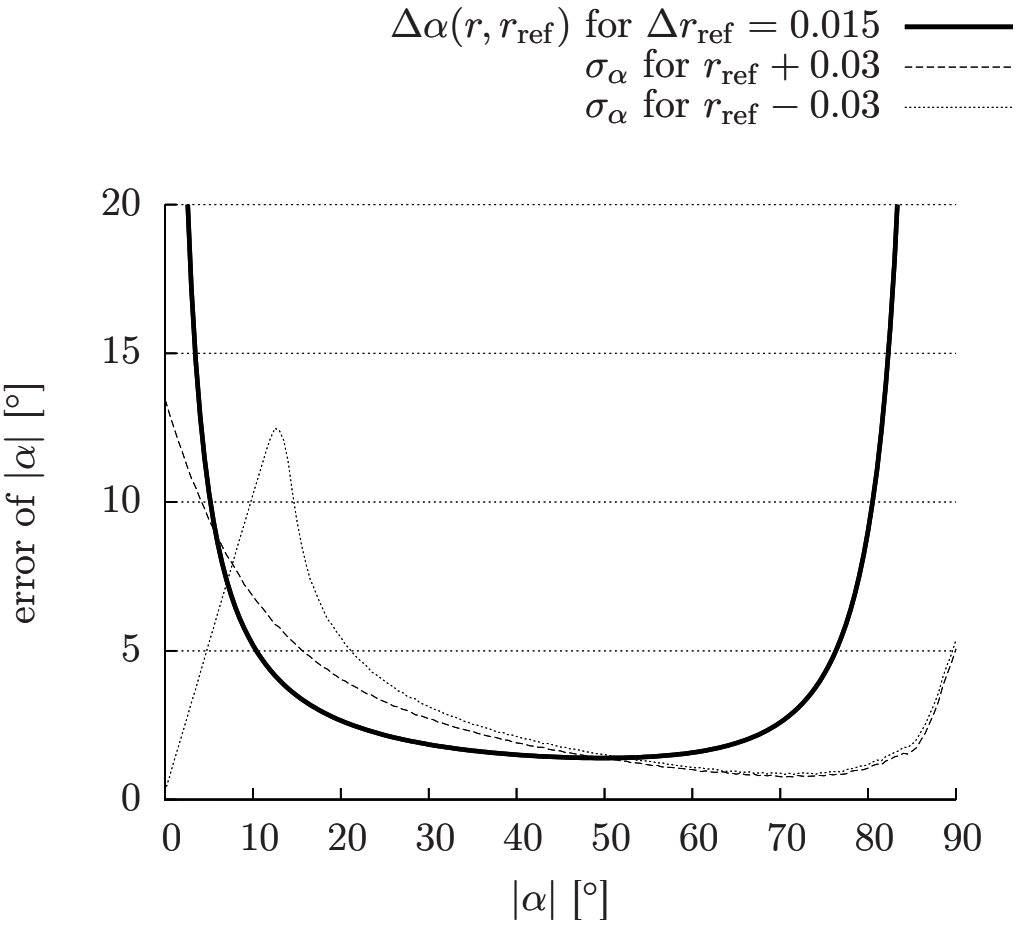

(b) The retardation reference value is chosen with a bias $r_{\text{ref}} \pm 0.03$ and with uncertainty $\sigma_{r_{\text{ref}}} = 0.015$ respectively.

Figure 3.11: The standard deviation of the absolute inclination angle can be predicted by error propagation analysis ($\Delta\alpha$), and can be determined empirically from simulations (σ_α). For intermediate inclinations, the error is estimated on an equal level by both methods. At the edges, the theoretically propagated error is considerably larger.

occurs in many regions of the human brain. A very prominent example is the optic chiasm, the crossing of the optic nerves, which is found in many animal species. In this simulation, the crossing fiber arrangement was designed to compare with a real tissue sample, the optic chiasm of a hooded seal *(Cystophora cristata)* (Fig. 3.15d). The fiber orientations of the synthetic fiber crossing were chosen to run orthogonally to each other. The in-plane orientation was sampled from a normal distribution in order to add a realistic variance. The investigation of the optic chiasm of the hooded seal is particularly interesting, because it is not known whether all fibers actually cross to the other side, or if fibers exist, that continue ipsilaterally. In the optic chiasm, the majority of fibers cross from one optic nerve to the contralateral optic tract, but the portion of fibers, that does not cross is very diverse in different species [67], [102]. In mammals, a correlation between the degree of the binocular field of view and the degree of non-crossing fibers has been proposed [49], [107]. However, the binocular view field has not been investigated for the hooded seal. For a close relative of the hooded seal, the harbor seal [55], the binocular view field suggests a fraction of crossing fibers of approx. 50 %. In addition to the crossing fiber arrangement, a so-called kissing fiber arrangement was created (Fig. 3.12b), which demonstrates the possible course of ipsilateral running fibers. A combined fiber arrangement was also created (Fig. 3.12c). A conclusion about the structure of the optic chiasm must be supported by comparison of all data sets.

The synthetic crossing fibers were generated by randomly placing starting seeds in the center of the simulation volume. Alternately, the fiber direction was sampled normally around 45° and 135° respectively. The chosen fiber direction was continued in both directions up to the border of the simulation volume to constitute a synthetic fiber path.

The crossing fiber arrangement was selected for simulation, because the mixture of different fiber orientations in one pixel clearly violates the assumption of homogeneous tissue in standard PLI analysis. In order to ensure correct interpretation, the effect of fiber orientation mixture must be investigated. The evaluation of mixed fiber orientations was performed on fibers with two groups of direction angles ($\varphi \approx 45°$ and $\varphi \approx 135°$), while the out-of-plane inclination angle α of the synthetic fibers was set to 0°. This allows the

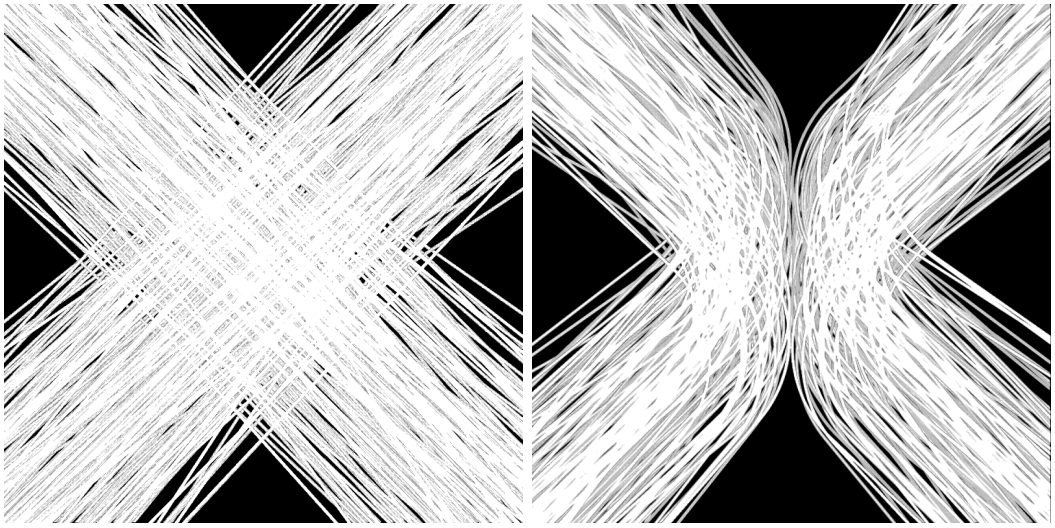

(a) Crossing fibers

(b) Kissing fibers

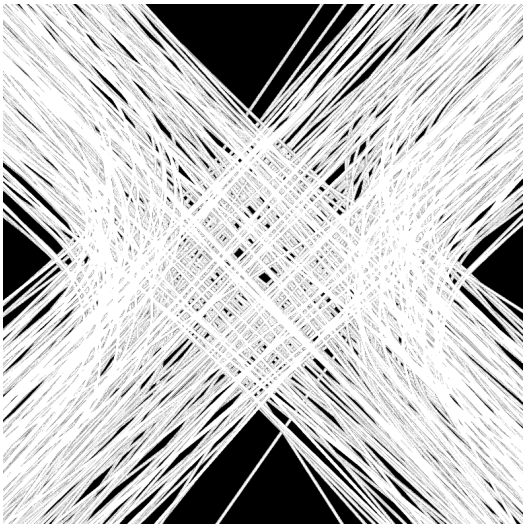

(c) Crossing and laterally non-crossing fibers

Figure 3.12: These synthetic fiber arrangements were designed to investigate the mixture of crossing fibers and to reproduce typical fiber arrangements in the optic chiasm. This is rendered visualization with a view onto the x-y-plane.

description of fiber mixture by relating the number of fibers of one orientation to the number of total fibers inside one pixel. For example, a relative mixture of 40 % describes the situation of ten mixed fibers, consisting of four fibers in the first group and six fibers in the second group.

The evaluation of the simulated crossing fiber arrangement was performed in two steps. First, in-plane resampling, blurring and sensor noise were omitted. This allows to examine the mixing fiber orientations without any additional sources of errors. Second, the crossing fiber arrangement was compared to the real data set. In this case, in-plane resampling, blurring and sensor noise were added such that a realistic data set was generated. In particular, the final size and spacing of the simulated data set was chosen in accordance with the optic chiasm of the hooded seal. The retardation reference value r_{ref} was set to 0.6 as before, but the attenuation $\mu = 4.4\,\text{mm}^{-1}$ was adapted to the light intensity, that was observed in the real data set. Also, the blurring radius was enlarged to improve the visual similarity to the real data set. A summary of all parameters is found in Tab. 3.2.

3.3.1 Results

The effects of fiber orientation mixture were examined for the in-plane direction φ and the out-of-plane inclination α separately. The direction angles derived from the simulated PLI signal were evaluated in sets of equal relative mixtures. Figure 3.13 shows the mean values and standard deviations of each relative mixture class. The simulated mixture of directions yields arbitrary direction angles, where perpendicular fiber directions are mixed in equal parts. However, if one of the relative mixture lies above 60 % or below 40 %, then the simulated mixed direction matches the underlying majority at average. This behavior of mixing fiber orientations considerably differs from the intuitive idea of a mixed fiber orientation, that lies in between underlying fiber orientations. Instead, the orientation of the majority of the underlying fibers is conserved.

The fiber inclination is also influenced strongly by fiber mixture (Fig. 3.14). The true fiber inclination in the crossed fiber arrangement is 0°, but the simulation and subsequent analysis results in quite steep inclination angles in the crossing region. The measured inclination angle obviously correlates

Table 3.2: Simulation parameters of crossing fiber arrangement

parameter name	symbol	value	unit
image size x	s_x	100	px
image size y	s_y	100	px
image size z	s_z	1	px
pixel spacing x	m_x	64	μm
pixel spacing y	m_y	64	μm
pixel spacing z	m_z	70	μm
upsampled pixel spacing x	m'_x	5	μm
upsampled pixel spacing y	m'_y	5	μm
upsampled pixel spacing z	m'_z	5	μm
# of fibers	n	450	
fiber radius	r_f	20	μm
incident light	I_0	15 700	a.u.
reference retardation	r_{ref}	0.6	
attenuation	μ	4.4	$\frac{1}{\text{mm}}$
blurring radius	σ_r	256	μm
sensor noise	σ_c	150	a.u.

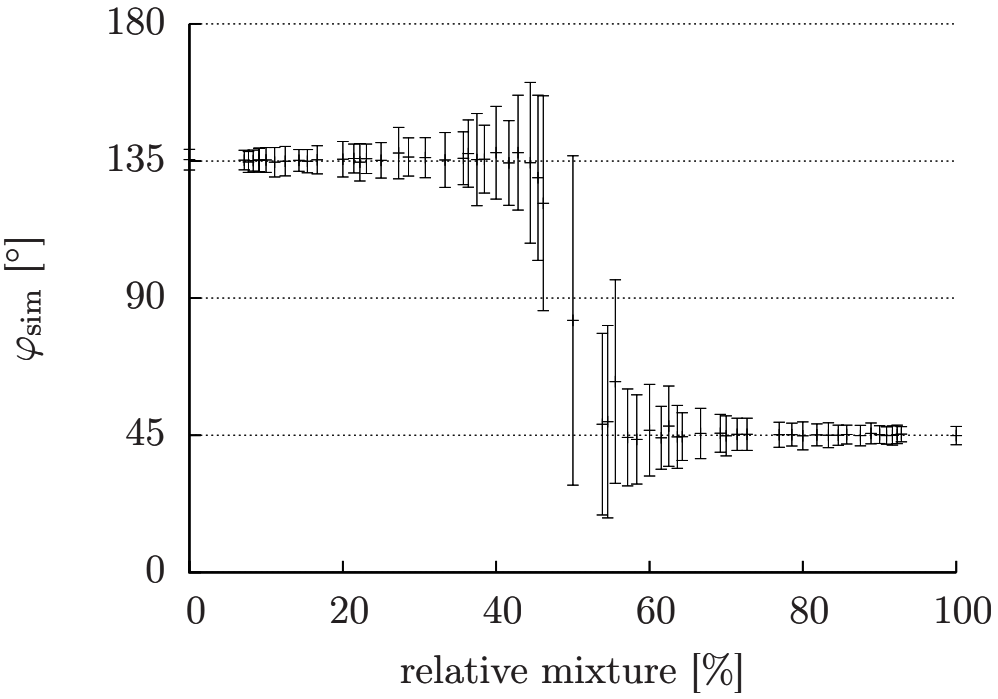

Figure 3.13: The simulation of PLI measurements yields a fiber direction φ_{sim}, that reflects the mixture of different fiber orientations in one pixel. This simulated resulting fiber direction does not correspond to an intuitive arithmetic mean. The simulated fiber direction corresponds to the direction of the majority of the underlying fiber directions with growing uncertainty when underlying fiber orientations are more balanced.

with the relative mixture, such that mixtures of equal parts create the highest inclination angles. The inclination angles further increase with a lower tissue density, i.e. with a lower number of total fibers.

For comparison with the measured fiber orientations in the optic chiasm (Fig. 3.15d), three fiber arrangements were simulated and the orientation were extracted by standard PLI analysis (Fig. 3.15(a)-(b)). The orientations in the crossing fiber arrangement generally resemble the orientations in the optic chiasm. The kissing fiber arrangement contains many vertical fiber orientations, that are not found in the real tissue sample. However, the lateral edges of the measured optic chiasm are also similar to the edges in the crossing fiber arrangement. There is a slight impression of fiber transitions between the left and right optic nerve in real data.

3.3.2 Discussion

The fiber orientations in the optic chiasm of a hooded seal must be interpreted with care. The transitions between both optic nerves are anatomically impossible. The analysis of fiber mixtures in a fiber crossing shows, that even in mixed fiber arrangements, the measured fiber directions originate from a majority of fibers with the measured direction. Therefore, the measured directions, that show a transition between both optic tracts, that is not assumed to exist, can hardly be explained by errors of fiber mixtures. Possibly, other birefringent tissue components fulfill the observed smooth bend of orientations.

The lateral regions of the real optic chiasm are similar to the corresponding regions in all synthetic fiber arrangements. The analysis of mixed direction angles demonstrated, that a majority of fiber orientations that is mixed with a minority of different orientations along the z-axis, is hardly biased. This suggests, that if there are ipsilateral fibers in the optic chiasm of the hooded seal, then intermediate fiber orientations, that occur in bending fibers, should be visible although they are mixed with other directions. Clearly, the kissing fiber arrangement contains these intermediate fiber directions, but the optic chiasm does not. This argues for a complete crossing of the optic nerves to the contralateral tracts. Non-crossing fibers in the lateral regions are still possible

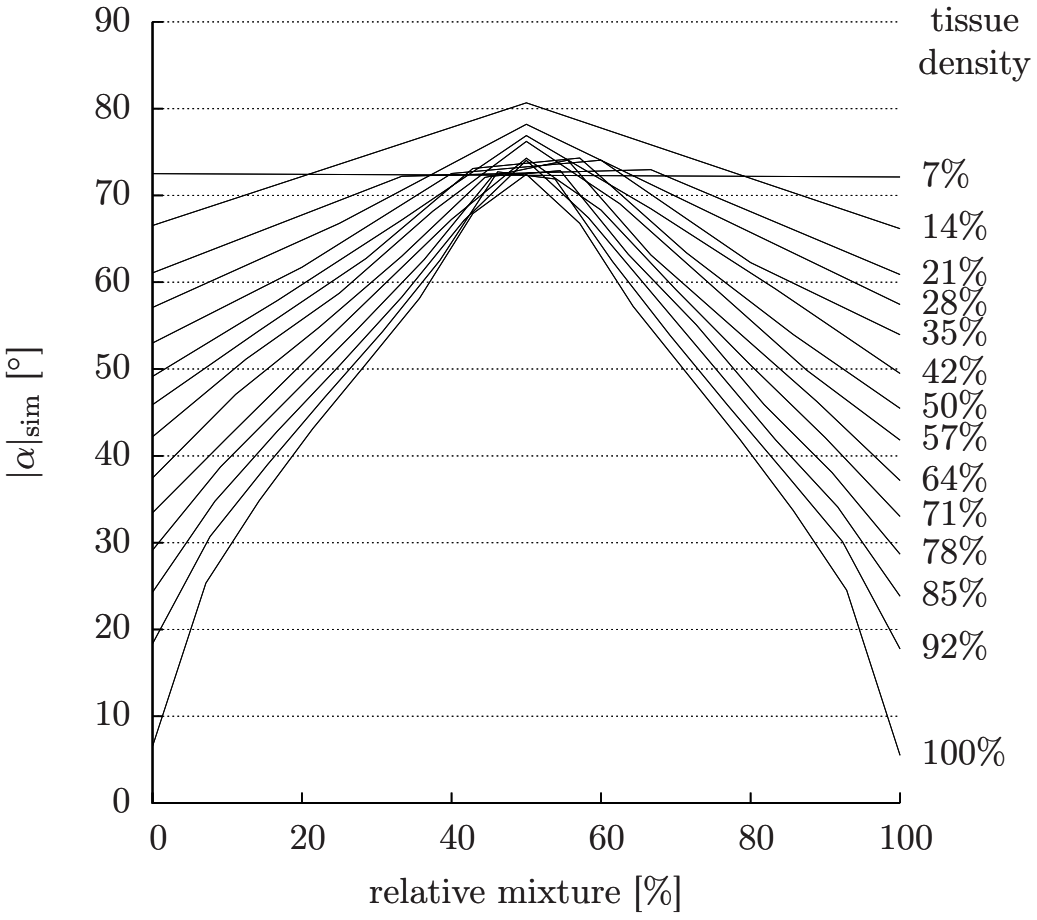

Figure 3.14: The true inclination in this fiber arrangement is 0°. However, the mixture of fibers attenuates the measured signal, such that the simulated inclination angle is much higher than the true inclination angle. The effect is the strongest for balanced mixtures. The tissue density describes the fraction of tissue in the examined volume. The simulated data set has a thickness of 70 μm and the synthetic fibers were sampled with a resolution of 5 μm. The tissue density is 100 %, if the complete thickness is filled with synthetic fibers and 0 %, if this part of the data set does not contain any synthetic fibers. A low tissue density also strongly overestimates the inclination angle.

though as shown by the combined fiber arrangement, which is also quite similar to the real data set. It is known, that non-crossing fibers typically pass the optic chiasm in the lateral region [67].

The analysis of the fiber course could be supported by results of tractography. However, the problems, that arise from the mixture of fiber orientations have also become obvious. The fiber inclination, that is derived by standard PLI analysis, is heavily biased by signal extinction of perpendicular orientations. The actually flat fibers are determined with inclination angles that strongly correlate with the relative mixture of fiber orientations. Therefore, tracking out-of-plane fiber orientations in this vector field will result in artifacts rather than realistic fiber tracts. This signal attenuation also affects the fiber direction. The fiber direction in equally balanced fiber mixtures is determined with arbitrary errors. This is in line with the observation of direction angles at high inclination angles (Fig. 3.9a). The determination of the in-plane fiber direction is strongly affected by high inclination angles. This is the case both for truly high inclination angles, or for overestimated inclination angles due to fiber mixture or low tissue density. It is likely that, if the amplitude of the PLI signal falls below a specific limit, then the phase, i.e. the direction angle, cannot be determined anymore by Fourier analysis (see Section 2.4). This must be examined in future studies. Possibly, the accuracy of the direction angle can be improved in these cases, by a more robust derivation of the direction angle from the PLI image series.

The varying number of fibers, that also influences the inclination angle, again reflects the problem to find the correct retardation reference value r_{ref}. The birefringence of a single fiber differs, of course, from that of two fibers, if all fibers have equal properties. Probably, the fiber density does not vary as strong as it does in this synthetic fiber arrangement, but the consequences of different fiber densities in real tissue must be kept in mind for interpretation.

In this chapter, the simulations of two fiber arrangements have been analyzed with respect to many details. Three main sources of errors, i.e. fiber mixture, imprecise knowledge about tissue properties, and sensor noise, were observed and quantified. The presented fiber arrangements are examples of the broad set of possibilities that are now available to simulate PLI measurements. The simulation framework can be easily extended by any other

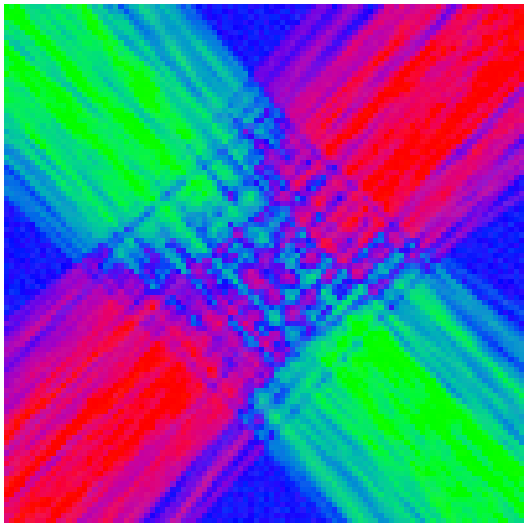

(a) Simulation of crossing fibers

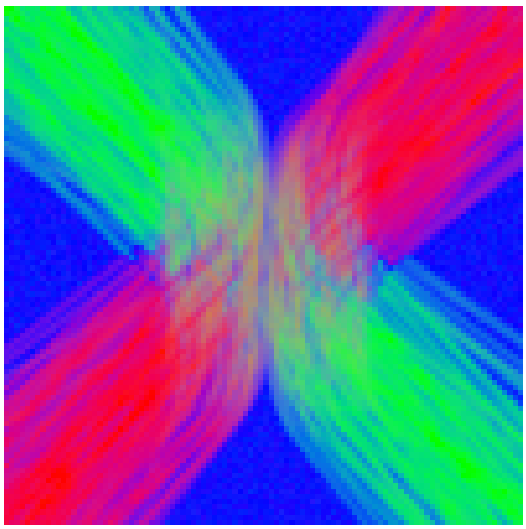

(b) Simulation of kissing fibers

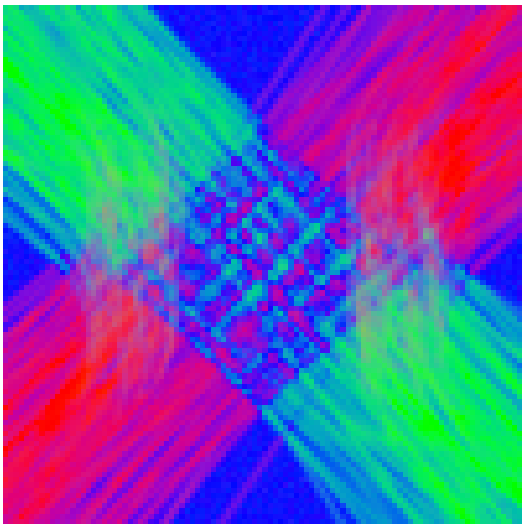

(c) Simulation of crossing and laterally non-crossing fibers

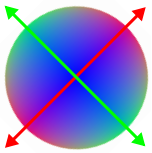

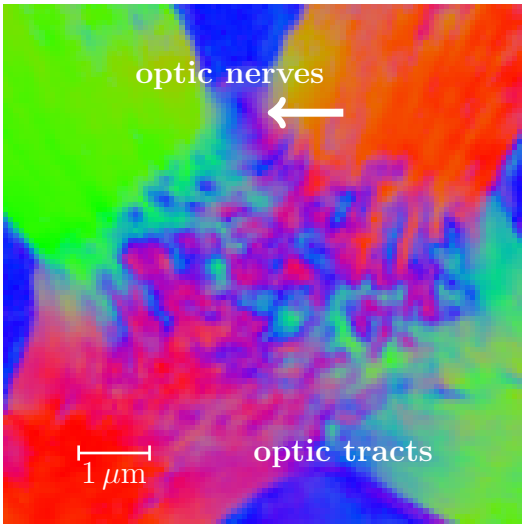

(d) Optic chiasm of a hooded seal

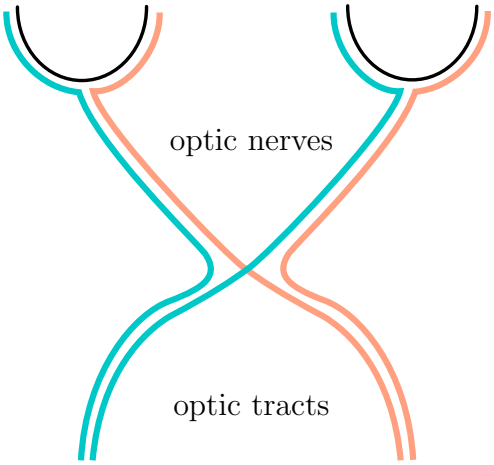

(e) Scheme of the optic chiasm

Figure 3.15: The comparison of the synthetic fiber arrangements (a)-(c) to the optic chiasm of the hooded seal (d), suggests that most fibers of the optic nerves cross to the contralateral optic tract. It is not known exactly how many fibers pass the optic chiasm on the ipsilateral side. The measured fiber orientations must be interpreted with care. There seems to be a transition of fibers between both optical nerves (arrow), which contradicts to anatomical knowledge (e).

fiber arrangement. Further developments could allow a different fiber radius for each synthetic fiber. The application of a perspective transform is under development and could reproduce another source of potential measurement errors. The simulation of fiber arrangements is an important contribution to the interpretation of measured fiber orientations. The simulation has also demonstrated, which limitations and problems arise for the reconstruction of nerve fibers from fiber orientations measured by PLI.

Chapter 4

PLI Inclination Sign Ambiguity

The measurement setup presented in Section 2.2 allows the derivation of the absolute inclination angle $|\alpha|$ but not the derivation of the inclination sign $l \in \{+1, -1\}$. This leads to an ambiguity, that must be treated in order to reconstruct a fiber orientation correctly. The unambiguous fiber orientation is of specific interest, when fiber tractography across neighboring sections is envisaged. Larsen et al. [81] presented an optimization approach to overcome the inclination sign ambiguity in PLI by minimizing the difference between neighboring fiber orientations with simulated annealing. Unfortunately, this approach relies on a set of pixels, where the inclination sign must be known. In regions, where neighboring fiber tracts only differ by their inclination sign, one of these fiber tracts tends to be assigned with the wrong inclination sign to minimize their difference. Therefore, it is necessary to measure additional information about the inclination sign at each pixel. For a polarizing microscope, Pajdzik [97] presented a tilting stage to differentiate positive and negative inclination signs of crystal orientations. Similarly, a tilting setup was developed for PLI. The tiltable setup, which allows to derive the inclination sign, is presented in Section 4.1 in detail. In Section 4.1.3, the reliability of the derived inclination sign is investigated, and it is shown, that the derived inclination sign is very sensitive to noise. This motivates the further enhancement of the reliability of the inclination sign in Section 4.2. For this purpose, a Markov Random Field optimization approach is presented (see also [74]).

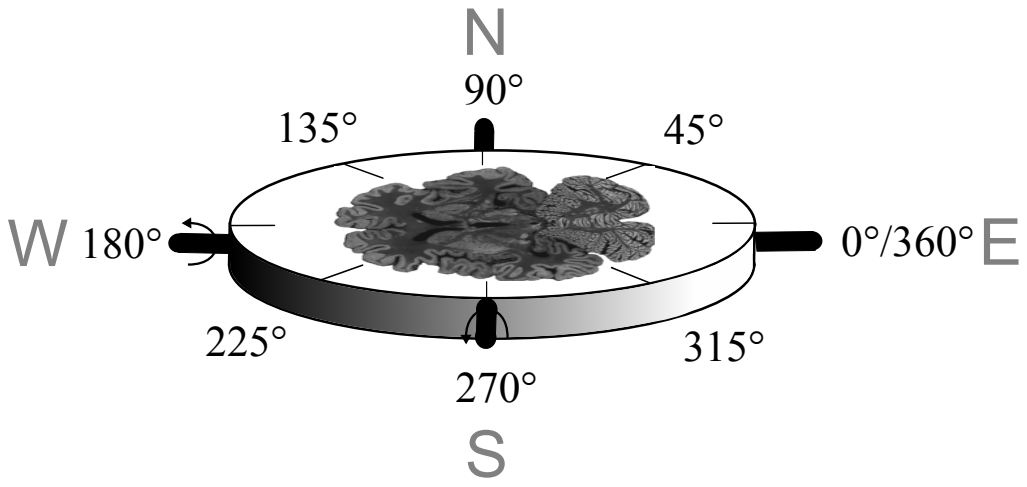

Figure 4.1: The tiltable specimen stage is tiltable in two axes, i.e. in four directions. The tilting direction ψ is given as a geographic direction or in degrees alternatively. The nomenclature in degrees is a common reference for the filter rotation angle ρ, the fiber in-plane direction φ and the tilting direction ψ.

4.1 Tilting Setup

In order to derive unambiguous information about the inclination sign at each image pixel, the polarimeter (see Section 2.2) contains a tiltable specimen stage.

There are two tilting axes, which are aligned with the orthogonal image axes of the camera. The specimen stage can be tilted clockwise and counter-clockwise by an angle $\tau \approx 4.0°$ around both axes, which leads to four tilting positions in addition to the flat, untilted position. The tilting position is denoted by ψ expressed as an angle. The four directions, that are currently available for tilting, are also named by geographic directions (N = 90°, W = 180°, S = 270°, E = 0°) as an intuitive nomenclature, meaning that the edge of the specimen in the specified direction ψ is tilted down towards the light source. The tilting direction angle ψ refers to the same coordinate system as the in-plane fiber direction φ and the filter rotation angle ρ (Fig. 4.1).

4.1.1 Comparison of Tilted Images

The tilted positions of the two-dimensional specimen plane represent small rotations in three-dimensional space, which result in perspective transformations of the two-dimensional images. In order to compare the same point of tissue in different tilting positions, the perspective transformation, a homography, must be determined. This can be done by automatic detection of characteristic features, for example by Scale Invariant Feature Transforms (SIFT) [88], and their correct mapping in different images. The estimation of the homography matrix becomes robust by applying RANdom SAmple Consensus (RANSAC) [41] on all feature mappings.

The modalities retardation r and direction φ are not suitable for feature detection, because their intensities change noticeably by tilting. This violates the basic assumptions of standard image feature matching techniques. The transmittance I_t changes only slightly for different tilting positions due to the elongated optical path, but these changes are below the sensitivity of the camera. Therefore, I_t is used to detect corresponding landmarks in the images of all tilting positions in order to determine and invert the perspective transformation.

4.1.2 Derivation of the Inclination Sign by Tilted Measurements

The parameters that were measured in tilting position ψ are specified by a superscript, e.g. α^ψ and r^ψ in contrast to α and r on a flat specimen stage. For each tilting direction ψ, the opposite direction is $\psi \pm 180°$. To achieve a reasonable effect, the tilting direction must be aligned to the fiber direction as well as possible. In other words, the difference $|\varphi - \psi|$ should be as small as possible. In the current setup with four directions, in the worst case, the difference between fiber direction and tilting direction is 45°. If the fiber in-plane direction and the tilting direction are aligned well, fibers with positive inclination can be distinguished from those with negative inclination by their decrease in absolute inclination after tilting (Fig. 4.2). The closer the fiber in-plane direction is aligned to the tilting direction, the larger is the effect of tilting on the fiber inclination. If the fiber direction is perpendicular to

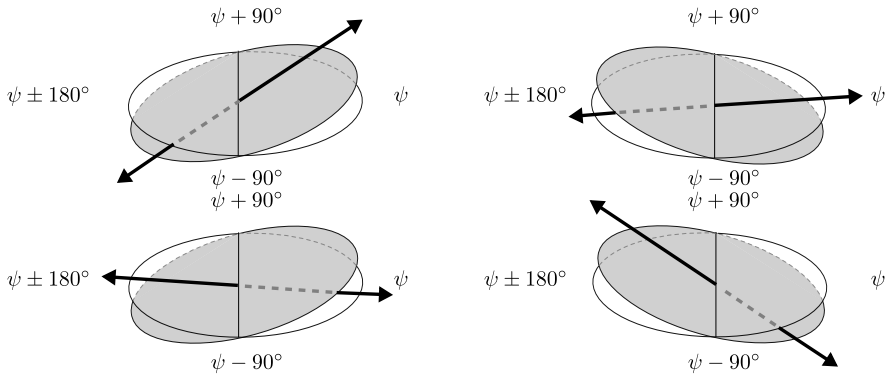

Figure 4.2: The tilting process is shown for fibers with $\varphi = \psi$. The absolute inclination, i.e. steepness, of fibers with a positive inclination sign (top row) decreases when tilting to ψ. If the inclination sign is negative (bottom row), the steepness increases.

the tilting direction, the fiber inclination is not changed at all. If the fiber direction deviates from the tilting direction by more than 90°, the change is inverted. The signum function formalizes this relation to

$$\operatorname{sgn}(\alpha) = \operatorname{sgn}(|\alpha^{\psi \pm 180°}| - |\alpha^{\psi}|) \cdot \operatorname{sgn}(\cos(\varphi - \psi)) \; . \tag{4.1}$$

In order to derive the inclination sign from retardation values, the strictly decreasing relation between inclination and retardation (for $0 < d_{\mathrm{rel}} < 1$ as shown in (2.6)) may be applied as

$$\operatorname{sgn}(\alpha) = \operatorname{sgn}(r^{\psi} - r^{\psi \pm 180°}) \cdot \operatorname{sgn}(\cos(\varphi - \psi)) \; . \tag{4.2}$$

Note, that the change of retardation already takes place, when comparing a tilted measurement with the flat measurement. The change is more effective though, if the retardation of opposite tilting positions are compared. Therefore, the inclination sign is derived from opposite tilting positions as a standard. However the statement (4.2) would be correct as well, if either r^{ψ} or $r^{\psi \pm 180°}$ were replaced by r. The same applies for (4.1) and α^{ψ}, $\alpha^{\psi \pm 180°}$, and α.

Description of Tilting as Rotation The exact change of α and φ can be calculated by multiplying the corresponding rotation matrices with the

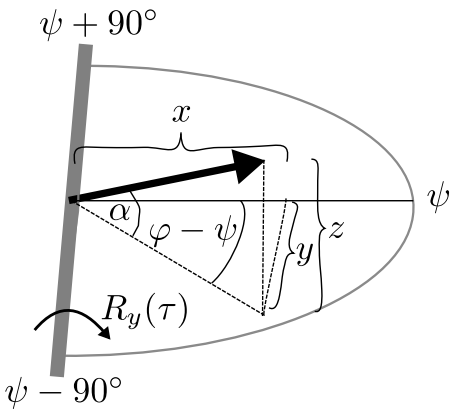

$$\boldsymbol{v} = \begin{pmatrix} \cos(\alpha)\cos(\varphi-\psi) \\ \cos(\alpha)\sin(\varphi-\psi) \\ \sin(\alpha) \end{pmatrix}$$

Figure 4.3: The tilting transformation in direction ψ, which is applied to vector $\boldsymbol{v} = (x, y, z)^T$, is a clock-wise rotation around the y-axis.

derived vector (4.3). If ψ is related to φ, the rotation can be expressed by clock-wise rotation around the y-axis (Fig. 4.3).

$$\begin{aligned} \boldsymbol{R}_y \cdot \boldsymbol{v} &= \begin{pmatrix} \cos(\tau) & 0 & -\sin(\tau) \\ 0 & 1 & 0 \\ \sin(\tau) & 0 & \cos(\tau) \end{pmatrix} \cdot \begin{pmatrix} \cos(\alpha)\cos(\varphi-\psi) \\ \cos(\alpha)\sin(\varphi-\psi) \\ \sin(\alpha) \end{pmatrix} \\ &= \begin{pmatrix} \cos(\alpha)\cos(\varphi-\psi)\cos(\tau) - \sin(\alpha)\sin(\tau) \\ \cos(\alpha)\sin(\varphi-\psi) \\ \cos(\alpha)\cos(\varphi-\psi)\sin(\tau) + \sin(\alpha)\cos(\tau) \end{pmatrix} \end{aligned} \tag{4.3}$$

4.1.3 Reliability of the Derived Inclination Sign

The standard PLI measurement acquires PLI images series in four tilted positions in addition to the flat position. As mentioned above, only two oppositely tilted measurements or one tilted and the flat measurement are necessary to derive an inclination sign according to (4.2). This produces redundant information about the inclination sign. In the following experiments, the inclination signs derived from various combinations of tilted measurements are compared. It is expected, that the derived inclination signs are consistent. A high consistency of independently derived inclination signs would argue for a high reliability of the derived inclination sign and a high reproducibility of the tilted measurements.

Experiments The white matter of four human brain sections was manually segmented and examined (Fig. 4.4).

First, the inclination sign was derived from one tilted and the flat measurement. This was compared to the inclination sign derived from the oppositely tilted and the flat measurement (see N-flat-S and W-flat-E in Fig. 4.4). Only pixels with a fiber in-plane direction $\varphi = \psi \pm 10°$ were considered to assure a good alignment between φ and ψ and thereby a large effect.

Second, the inclination sign was derived according to (4.2) with $\psi = \mathrm{N}$ and then compared to the derived inclination sign with $\psi = \mathrm{W}$ (see NS-WE in Fig. 4.4). Thereby, both signs are derived independently. To ensure a similar alignment between fiber direction and tilting direction for both tilting axes, only fibers that run near the bisecting line in between both axes were considered ($\varphi = 45° \pm 10°$, $\varphi = 135° \pm 10°$).

Results and Discussion The derived sign from combined flat and single tilted measurement is inconsistent in 42.05 % to 75.52 % of all considered pixels. The tilting amplitude $\tau \approx 4°$ seems to be too small to observe changes between flat and tilted measurements reliably. The largest sample even shows the most significant inconsistency between both derived signs. This suggests, that there are additional influences, which disturb the derivation of the inclination sign by observing the retardation change between a flat and tilted measurements. These influences could include differing scatter and reflection properties. As a consequence, the inclination sign must be derived from opposite tilting positions with a tilting amplitude $\tau \geq 4°$. Otherwise, the derivation of the inclination sign is random.

The inclination sign derived from tilting in N and S compared to tilting in W and E are consistent for 56.78 % to 64.23 % of all considered pixels. For the majority of these pixels, the inclination sign is derived equally from both tilting axes, however a large part of the examined pixels received inconsistent inclination signs. Probably, the true error rate of the derived inclination sign is lower than the rate of inconsistent pixels, because the alignment between the fiber direction and the tilting direction is not equal for both derived signs. The better aligned tilting axes should be used to solve these inconsistencies. However, the true inclination sign is not known and the

relatively high inconsistencies for fiber orientations, that are not well aligned to the tilting axes, suggest that the derivation of the inclination sign in these pixels is not very reliable. The correction of the derived sign in such pixels with image restoration methods is reasonable. Further sources of errors, such as interpolation errors from the inverted perspective transformation or the influence of very high and very low inclination angles, which are not resolved well by the non-linear relation between retardation and inclination (see (2.6)), have not been investigated quantitatively, but support the need for post-processing.

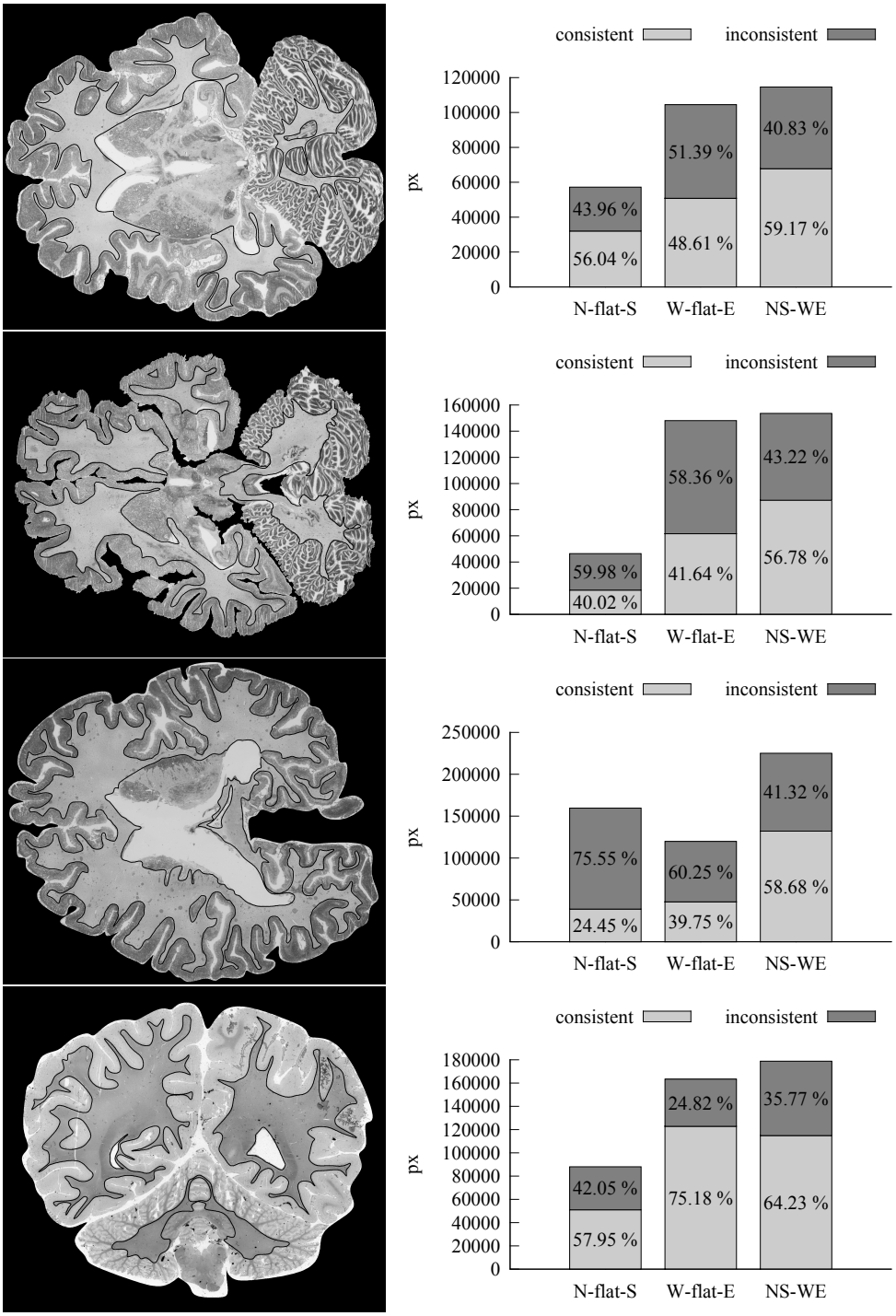
consistent
inconsistent
px
120000
100000
80000
60000
40000
20000
0
43.96 %
56.04 %
51.39 %
48.61 %
40.83 %
59.17 %
N-flat-S
W-flat-E
NS-WE
consistent
inconsistent
px
160000
140000
120000
100000
80000
60000
40000
20000
0
59.98 %
40.02 %
58.36 %
41.64 %
43.22 %
56.78 %
N-flat-S
W-flat-E
NS-WE
consistent
inconsistent
px
250000
200000
150000
100000
50000
0
75.55 %
24.45 %
60.25 %
39.75 %
41.32 %
58.68 %
N-flat-S
W-flat-E
NS-WE
consistent
inconsistent
px
180000
160000
140000
120000
100000
80000
60000
40000
20000
0
42.05 %
57.95 %
24.82 %
75.18 %
35.77 %
64.23 %
N-flat-S
W-flat-E
NS-WE

Figure 4.4: The white matter of four human brain sections was segmented manually as shown by the black contours in the transmittance images on the left side. The consistency of the inclination signs derived from different subsets of the tilted measurements was evaluated. The derived inclination sign from tilting to N to flat is expected to agree with the derived sign from flat to S (N-flat-S) for fibers that are aligned with the N-S axes ($\varphi - \psi = \pm 10°$). Analogously, the consistency was evaluated for tilting positions E and W compared to the flat position (W-flat-E). Finally, the inclination sign was derived from changes between N to S and from changes between W to E (NS-WE) for fibers that are oriented between both axes ($\varphi \in \{45° \pm 10°, 135° \pm 10°\}$).

4.2 Inclination Sign Enhancement

The inclination sign ambiguity can be regarded as a labeling problem. The tilted measurements provide information about the inclination sign to make a binary decision between positive (+) and negative (−) inclination sign. This is very similar to other typical image labeling problems in the domain of image processing, e.g. segmentation or denoising. Markov random fields (MRFs) were first introduced in computer vision by Geman and Geman [44] and allow the formulation of a labeling problem in terms of an energy optimization problem. The development of efficient energy optimization algorithms on MRFs [22], has made MRFs a powerful tool [27]. Similar ambiguity problems, e.g. with interferometric fields, have been solved successfully with MRFs [136, 18].

4.2.1 Markov Random Fields for Image Enhancement

A random field is defined as an undirected graph $\mathcal{G} = (\Omega, \mathcal{N})$ with a set of random variables Ω and a set of dependencies $\mathcal{N}$ between them. The stochastic event $x = l$ is the assignment of a label $l \in \mathcal{L}$ to a random variable $x \in \Omega$ with a probability $p(x = l)$. The joint labeling of all random variables in Ω is a configuration $L = \{x_0 = l_0, x_1 = l_1, \ldots, x_n = l_n\}$. In general, the random variables $x_i \in \Omega$ are not conditionally independent from each other. However, when the set of random variables to be labeled represents the set of pixels in an image, it is commonly assumed, that a stochastic event $x_i = l_i$ does not depend on the labeling of the entire image, but that there is a limited set of neighbored pixels, whose labels may influence $x_i = l_i$. For a set of random variables Ω, a configuration L, and a neighborhood relation $\mathcal{N}$, the Markov property states

$$p(x_i = l_i \mid L \setminus \{x_i = l_i\}) = p(x_i = l_i \mid \{x_j = l_j \mid (x_i, x_j) \in \mathcal{N}\}). \tag{4.4}$$

The Markov property simplifies the calculation of the joint probability of a configuration. According to Hammersley and Clifford [54], the joint probability can be expressed as

$$p(L) = \frac{1}{Z} \cdot e^{\sum_c E_c(L_c)}, \tag{4.5}$$

where a clique c is a maximal set of random variables, that is completely connected by the neighborhood relation $\mathcal{N}$, and $E_c : \Omega \to \mathbb{R}^+$ is a positive energy function. The partial configuration L_c is the subset of L defining the labeling of the random variables in c only. In order to find a configuration L^*, that maximizes the joint probability $p(L)$, (4.5) is logarithmized.

$$L^* = \underset{L}{\operatorname{argmax}}\, p(L) = \underset{L}{\operatorname{argmin}} \sum_c E_c(L_c) \tag{4.6}$$

In this way, the joint probability is transferred to a sum of independent energy functions for each clique. There are two types of relevant cliques, unary cliques, consisting of one random variable, and binary cliques, consisting of two random variables. The energy of a unary clique penalizes the label of the respective random variable. Typically, the unary energy functions are chosen according to some kind of observation or measurement for index i, and such a function is then denoted as *data energy* E_i. The energy of binary cliques defines the interaction between neighbored random variables. The smoothness of labels in neighbored random variables can be imposed by binary energy functions. In this case, the energy of binary cliques is denoted as *smoothness energy* $E_{i,j}$. The reference to indices i, j points out, that smoothness can be defined locally. In summary, the total energy is defined as a trade-off between data energies and smoothness energies, that can be controlled by a weighting factor λ.

$$E(L) = \sum_i E_i(x_i = l_i) + \lambda \cdot \sum_{(i,j)\in\mathcal{N}} E_{i,j}(x_i = l_i, x_j = l_j)\ . \tag{4.7}$$

For PLI, the set of labels $\mathcal{L} = \{-, +\}$ is binary and the set of random variables represents the pixels of the inclination image. Then, a configuration L assigns one of two signs to each image pixel and thereby gives a solution to the inclination sign ambiguity.

4.2.2 Design of Data and Smoothness Energy Functions

The definition of the data and the smoothness energy functions determines the quality of the resulting labeling. Therefore, the desired properties of the

solution must be defined in these functions. Generally, the set of possible energy functions is only limited to the class of positive functions. In this section, the data energy will be designed to express the relation between the tilted measurements and the inclination sign. For the smoothness energy, two alternatives will be presented. Both of them aim for a smoothing of the three-dimensional fiber orientation and therefore depend on the local in-plane fiber direction.

Data Energy The data energy is thought to include observations about the label at a certain image index. Here, these observations are PLI measurements in different tilting positions. Equation (4.1) shows how the inclination sign $\mathrm{sgn}(\alpha)$ can be derived from oppositely tilted, unsigned inclination angles $|\alpha^{\psi}|$, $|\alpha^{\psi\pm180°}|$, the fiber direction φ, and the tilting direction ψ. A large absolute difference between oppositely tilted inclination angles $|\alpha^{\psi\pm180°} - \alpha^{\psi}|$ argues for a large tilting effect and a high reliability of the derived sign. We therefore require the data energy to be proportional to the sum of these differences for all tilting directions $\psi \in \{\mathrm{N}, \mathrm{W}, \mathrm{S}, \mathrm{E}\}$.

$$E_i \propto \sum_{\psi} |\alpha_i^{\psi\pm180°} - \alpha_i^{\psi}| \,. \tag{4.8}$$

The data energy is minimal, when the label l_i corresponds to the true inclination sign $\mathrm{sgn}(\alpha)$. It is maximal, when the label l_i and the true inclination sign are inconsistent.

$$E_i(x_i = l_i) \propto -l_i \cdot \sum_{\psi} |\alpha_i^{\psi\pm180°} - \alpha_i^{\psi}| \cdot \mathrm{sgn}(\alpha_i) \tag{4.9}$$

As discussed in Section 2.5, and examined in simulations in Section 3.2, the inclination angle α is obtained with limited accuracy. This is due to the strong dependency of α on a possibly biased choice of d_{rel}, as well as the high sensitivity of α to noise for very steep and very flat fibers. However, there is an approximation of $|\alpha^{\psi\pm180°} - \alpha^{\psi}|$ that does not require d_{rel}, for small $|\tau|$, which is satisfied by $\tau = 4°$. The details are presented in the appendix.

Together with (4.2), this leads to the data potential

$$E_i(x_i = l_i) \propto -l_i \sum_{\psi} \Big(|-2\sin(\tau)| \cdot \operatorname{sgn}(r_i^{\psi} - r_i^{\psi \pm 180^\circ}) \cdot \cos(\varphi_i - \psi) \operatorname{sgn}(\cos(\varphi_i - \psi)) \Big) \tag{4.10}$$

By inserting $\psi \in \{\mathrm{N} = 90^\circ, \mathrm{E} = 0^\circ\}$, and omitting constant factors, the data energy is further simplified.

$$E_i(x_i = l_i) \propto -l_i \cdot \Big(\cos(\varphi_i - 90^\circ) \cdot \operatorname{sgn}(r_i^N - r_i^S) + \cos(\varphi_i - 0^\circ) \cdot \operatorname{sgn}(r_i^E - r_i^W) \Big) \tag{4.11}$$

For symmetry reasons, the insertion of $\psi \in \{\mathrm{W} = 180^\circ, \mathrm{S} = 270^\circ\}$ is not necessary. Finally, the data energy is normalized to values between 0 and 1.

$$E_i(x_i = l_i) = \frac{1}{2} - l_i \cdot \frac{\sin(\varphi_i) \cdot \operatorname{sgn}(r_i^N - r_i^S) + \cos(\varphi_i) \cdot \operatorname{sgn}(r_i^E - r_i^W)}{2\sqrt{2}} \tag{4.12}$$

The intuitive idea of the data energy is to derive the inclination sign from both tilting axes ($\operatorname{sgn}(r^N - r^S)$, $\operatorname{sgn}(r^E - r^W)$), and to weight the resulting signs according to the alignment of the fiber direction φ with the tilting axis ($\cos(\varphi - \psi)$). If both derived inclination signs agree and this sign corresponds to the assigned label, then the data energy becomes minimal. If both signs agree, but do not correspond to the assigned label, then the data energy becomes maximal. If both signs contradict, the sign derived from the better aligned axis is weighted stronger. If both signs contradict and both axes are aligned equally to the fiber orientation ($\varphi - \psi \in \{-135^\circ, -45^\circ, 45^\circ, 135^\circ\}$), then the tilted measurements do not contain any information about the inclination sign. Consequently, in this case, the data energy has the same value (0.5) for both possible labels, i.e. the data energy does not contribute to the optimal labeling (see Fig. 4.5).

Smoothness Energy It is assumed that neighboring pixels tend to belong to the same anatomical structure. It follows, that neighboring pixels tend to contain a similar fiber orientation, because the anatomical structure is

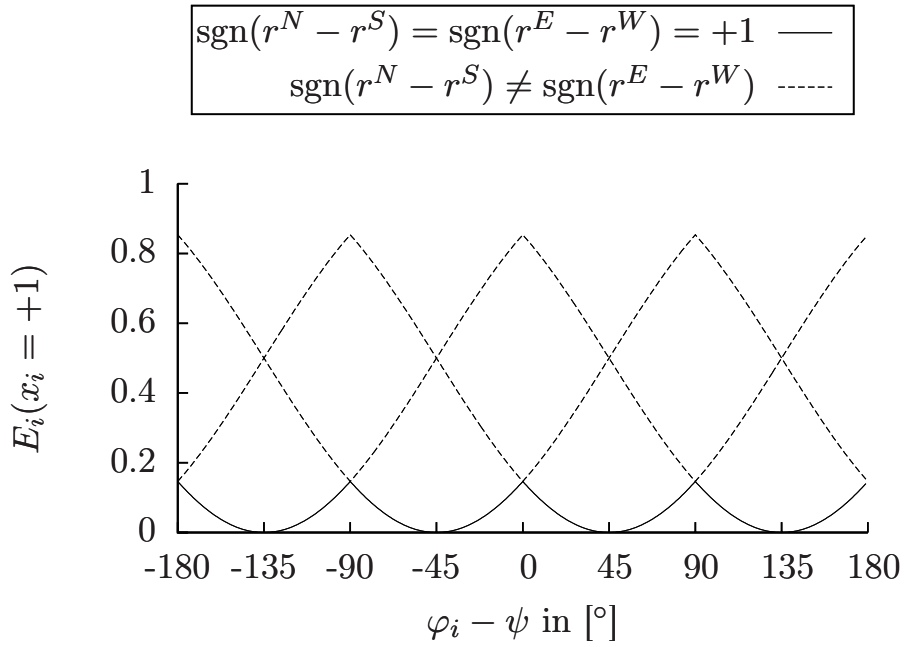

(a) Data energy for $x_i = +1$

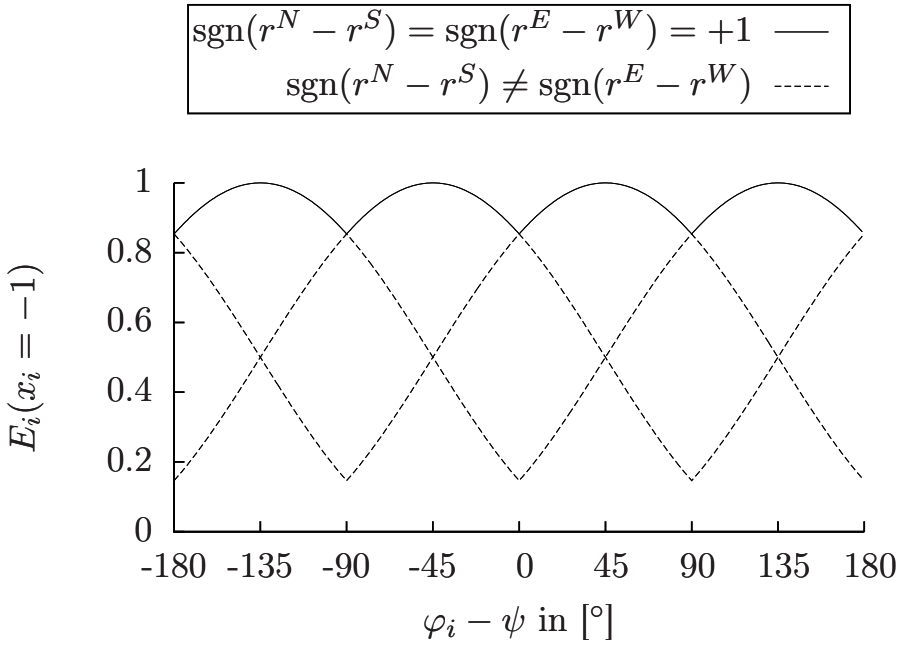

(b) Data energy for $x_i = -1$

Figure 4.5: The data energy depends on the relation of φ to ψ. The inclination sign can be derived from the tilted measurements of two tilting axes independently ($\mathrm{sgn}(r^N - r^S)$ and $\mathrm{sgn}(r^E - r^W)$). These plots show the data energy for the case, that both derived signs are positive, and for the case that both derived signs contradict. The corresponding signs push the data energy towards the minimum and maximum, respectively, while contradicting inclination signs yield intermediate energy values.

continued. Therefore, it is reasonable to impose smooth fiber orientations, especially to compensate for uncertain information. The smoothness energy has great influence on the computational complexity of the optimization. In general, the optimization of the joint probability in a Markov random field is NP-hard. According to Kolmogorov et al. [79], there is a class of energy functions, that can be solved in polynomial time. These functions are called graph-representable [79, Theorem 4.1]:

Theorem 4.2.1 (Submodularity Constraint) *Let E be a function of n binary variables, i.e.*

$$E(x_1 = l_1, x_2 = l_2, \ldots, x_n = l_n) = \sum_i E_i(x_i = l_i) + \sum_{i<j} E_{i,j}(x_i = l_i, x_j = l_j).$$

Then, E is graph-representable if and only if each term $E_{i,j}$ satisfies the inequality

$$\begin{aligned} E_{i,j}(x_i = 0, x_j = 0) \quad + \quad & E_{i,j}(x_i = 1, x_j = 1) \leq \\ & E_{i,j}(x_i = 0, x_j = 1) + E_{i,j}(x_i = 1, x_j = 0) \end{aligned}$$

This means, that the exact optimization of a smoothness energy function is not computable in practice, if the submodularity constraint is not fulfilled. Therefore, two alternative definitions of the smoothness energy will be presented and discussed. The first approach will impose smoothness in the complete three-dimensional fiber orientation, but is not submodular. The second approach is submodular, but only considers the in-plane fiber direction for the smoothness constraint.

To impose smoothness on the complete fiber orientation, the deviation δ of neighboring fiber orientations must be measured, e.g. by calculating the smallest enclosed angle.

$$\delta(\boldsymbol{v}_i, \boldsymbol{v}_j) = \min(\arccos(\boldsymbol{v}_i \cdot \boldsymbol{v}_j), 180^\circ - \arccos(\boldsymbol{v}_i, \boldsymbol{v}_j)) \tag{4.13}$$

The first smoothness term automatically follows this difference measure for two neighboring fiber orientations $\boldsymbol{v}_i$, $\boldsymbol{v}_j$ at indices i and j.

$$\begin{aligned} E_{i,j}(x_i = l_i, x_j = l_j) &\propto \delta(l_i \cdot \boldsymbol{v}_i^T, l_j \cdot \boldsymbol{v}_j) \\ &= \frac{1}{90^\circ} \cdot \delta(l_i \cdot \boldsymbol{v}_i^T, l_j \cdot \boldsymbol{v}_j)\,, \end{aligned} \tag{4.14}$$

In this definition, $E_{i,j}$ is normalized to values between 0 and 1. A plot of the smoothness energy function (Fig. 4.6a) illustrates that it is not submodular for $\Delta\varphi \geq 90^\circ$. Therefore, the minimization of (4.14) cannot be computed efficiently. Additionally, the energy function in (4.14) requires the inclination to be known. The reliability of the inclination was discussed in Sections 2.5 and 3.2.2. Considering the possible error in the inclination angle, an alternative graph-representable energy function, that refrains from including the inclination angle can be defined.

$$E_{i,j}(x_i = l_i, x_j = l_j) = \left(1 - \frac{|\varphi_i - \varphi_j|}{180^\circ}\right) \cdot \begin{cases} 1 & \text{, if } l_i \neq l_j \\ 0 & \text{, else} \end{cases} \tag{4.15}$$

This function corresponds to a *contrast-sensitive Potts model* [23, Eq. 3], where the contrast is defined as the absolute difference of neighboring in-plane fiber directions. The illustration in Fig. 4.6b confirms that this smoothness energy function is graph-representable according to Theorem 4.2.1.

Energy Optimization Various algorithms have been developed for the optimization of submodular and non-submodular energy functions in Markov random fields. Szeliski et al. have presented and compared some of them [124]. For the following experiments, the quadratic pseudo-boolean optimization (QPBO) described by Kolmogorov [78] based on ideas in [53] and [20] was used. It supports the optimization of submodular and non-submodular energy functions using the same interface. The implementation includes the min-cut/max-flow algorithm by Boykov [21]. The QPBO algorithm returns the optimal configuration for submodular energy functions, and a partial optimal configuration with possibly unlabeled pixels in case of non-submodular energy functions.

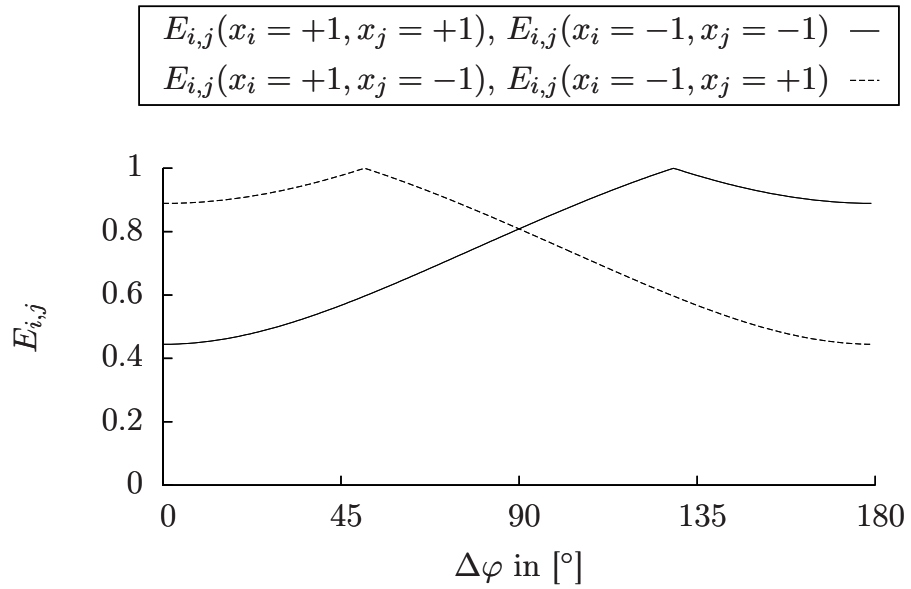

(a) The smoothness energy based on the full fiber orientation vectors (see 4.14) is illustrated for $\alpha_i = 60°$ and $\alpha_j = 20°$. This function is not submodular for $\Delta\varphi \geq 90°$.

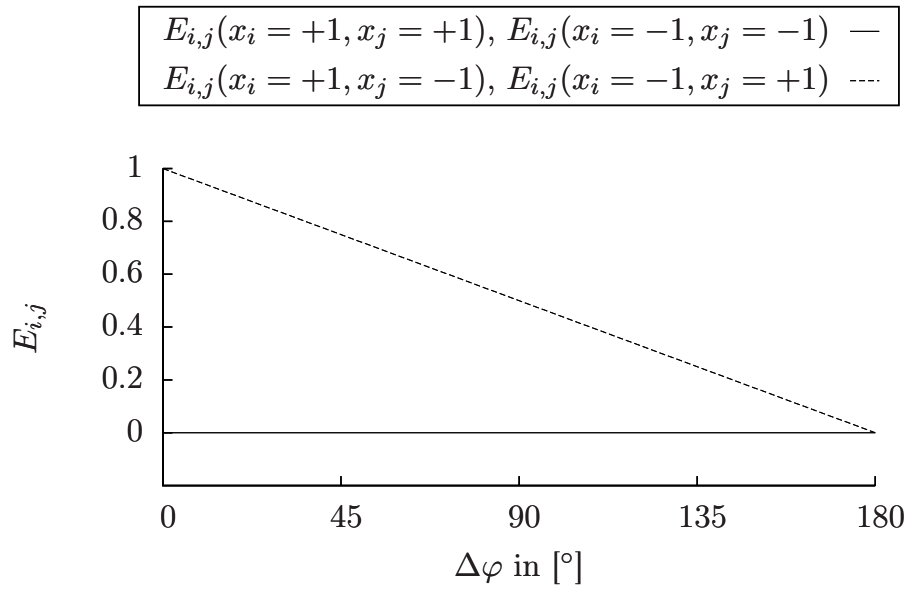

(b) This is the submodular smoothness energy based on a Potts model with a contrast function based on the in-plane fiber orientation (see 4.15).

Figure 4.6: Two alternative smoothness energy functions for the optimization of the joint probability in a Markov random field. For submodularity, see Theorem 4.2.1.

4.2.3 Experiments

The inclination sign and the resulting vector fields are evaluated on synthetic data and real data. The evaluation of synthetic data allows the comparison of the reconstructed inclination sign to the true inclination sign. For comparison, the derived inclination sign maps were also smoothed by application of a median filter. On binary images, the median filter replaces each pixel by the most frequently occurring binary value in its neighborhood. For a simple and clear reference to the applied methods, the following notation is used:

AllPos (+):	The inclination sign is assumed to be positive at all pixels.
DataOnly (DO):	The inclination sign is directly derived from tilted measurements, as presented in (4.2), with $\psi = N$ for $45° < \varphi < 135°$ and $\psi = E$ for $\varphi \leq 45°$ or $\varphi \geq 135°$.
DataMedian (DM):	The inclination sign is derived from tilted measurements and smoothed by a median filter.
GlobalOptPotts (GOP):	The MRF is equipped with a Pottsmodel sensitive to the contrast of the in-plane fiber direction according to (4.15) to enhance smoothness.
GlobalOptFull (GOF):	The MRF is equipped with a smoothness model, which computes the angular deviation between three-dimensional fiber orientations of neighboring pixels according to (4.14). This results in a non-submodular model.

Synthetic Data As a synthetic data set, the homogeneous tissue arrangement presented in Section 3.2 was used again. Additionally, the vector field was tilted, such that four additional simulated PLI image series were created. From each PLI image series, the retardation images r, $r^{0°}$, $r^{90°}$, $r^{180°}$ and $r^{270°}$ were computed. The reference value r_{ref} was determined with the standard fit procedure as described in Section 2.5, and the absolute inclination $|\alpha_{\text{sim}}|$ was

calculated from r. According to DataOnly, DataMedian, AllPos, GlobalOptPotts and GlobalOptFull, the inclination signs s_{DO}, $s_{DM}(R)$, s_+, $s_{GOP}(\lambda)$ and $s_{GOF}(\lambda)$, in general s_{sim}, were determined with weighting factor λ or radius R as indicated. For evaluation, the true orientation vector $\boldsymbol{v}$ was composed from the synthetic orientation angles φ and α (Fig. 3.4). Accordingly, the simulated orientation vectors $\boldsymbol{v}_{GOP}(\lambda)$, $\boldsymbol{v}_{GOF}(\lambda)$, $\boldsymbol{v}_{DM}(R)$, $\boldsymbol{v}_+$ and $\boldsymbol{v}_{DO}$, in general $\boldsymbol{v}_{\text{sim}}$, were composed from the simulated orientation angles φ_{sim} and $\alpha_{\text{sim}} = |\alpha_{\text{sim}}| \cdot s_{\text{sim}}$. The difference between the true and the simulated vectors was measured by the root mean squared deviation (RMSD) of the enclosed angles (see (4.13)):

$$\text{RMSD} = \sqrt{\frac{1}{N}\sum_{i=1}^{N}(\delta(\boldsymbol{v}, \boldsymbol{v}_{\text{sim}}))^2} \tag{4.16}$$

Background pixels displayed in black in Fig. 3.4 are not considered.

Additionally, the sensitivity was determined as the fraction of pixels that were assigned the wrong sign in DataOnly, but corrected by GlobalOptPotts or GlobalOptFull respectively.

Human Brain Data The different approaches were applied to sections of human post-mortem brains without pathological findings. Three regions of interest, that represent the diversity of the results, were selected (Fig. 4.10-4.12). The inclination signs were determined by AllPos, DataOnly, DataMedian, GlobalOptPotts and GlobalOptFull for $R = 1$ and three values of λ. In human brain data, there is no alternative method to reliably determine the inclination sign. Therefore, the human brain data presented here cannot be objectively compared to ground truth. In order to evaluate the computed inclination signs, an appropriate visualization of the vector field is necessary. Inconsistencies in the resulting fiber orientation must become visible. The resulting 3D orientations were visualized in a special HSV color space. The hue and saturation represent the fiber in-plane direction and the absolute inclination respectively. The brightness component was used to emphasize local differences, which were obtained in terms of the mean

absolute deviation $\bar{\delta}$ in the 8-neighborhood of each pixel i.

$$\text{Hue}(\varphi) = 2\varphi \tag{4.17}$$

$$\text{Saturation}(\alpha) = 1 - |\alpha|/90° \tag{4.18}$$

$$\text{Value}(\bar{\delta}) = 1 - \bar{\delta} \tag{4.19}$$

The color coding highlights abrupt changes in the vector field by dark pixels or edges. Accordingly, unexpected changes in the vector fields, which could be caused by wrong inclination signs, are made visible.

Apart from the comparison of different methods, it is also crucial to determine a reasonable value for the weighting factor λ. This is a common problem in image restoration and regularization [32]. A natural approach is to plot data and smoothness energy after optimization with different values for λ, and to look for a good trade-off between both constraints. This plot is also known as the L-curve [57]. According to the *L-curve criterion* [56], the point on the corner of the L-curve is a good choice for the regularization parameter. The L-curve was calculated for the complete human brain section shown in Fig. 4.11.

4.2.4 Results

Synthetic Data The resulting vector fields were also colored with the HSV color coding defined in (4.17)-(4.19) (Fig. 4.7). In $\boldsymbol{v}_+$ and $\boldsymbol{v}_{\text{DM}}$, undesired vertical edges arise, where the fiber direction changes from 0° to 180° and the inclination sign changes simultaneously (compare to Fig. 3.4(a)-(b)). In $\boldsymbol{v}_{\text{DO}}$, $\boldsymbol{v}_{\text{GOP}}$ and $\boldsymbol{v}_{\text{GOF}}$, the vector field closely resembles ground truth. Only very modest noise can be found in the center. There is no visible difference between $\boldsymbol{v}_{\text{DO}}$, $\boldsymbol{v}_{\text{GOP}}$ and $\boldsymbol{v}_{\text{GOF}}$. The RMSD values, that measure the difference between the reconstructed and true vector field are plotted in Fig. 4.8. GlobalOptFull achieves the lowest value of all methods (1.490°) at $\lambda = 5.3$. GlobalOptPotts reduces the RMSD to 1.497° at $\lambda = 0.26$. DataOnly achieves an error of 1.613°, which is the same as GlobalOptPotts and GlobalOptFull for $\lambda = 0$. DataMedian does

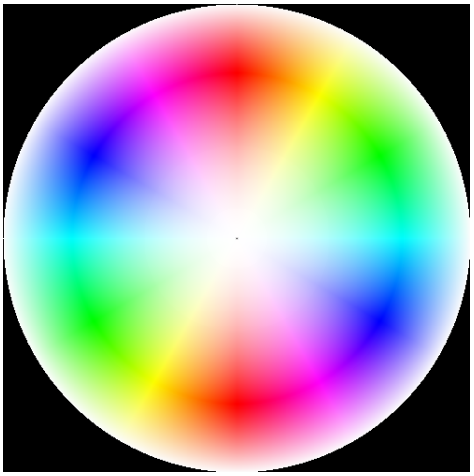

(a) Ground truth

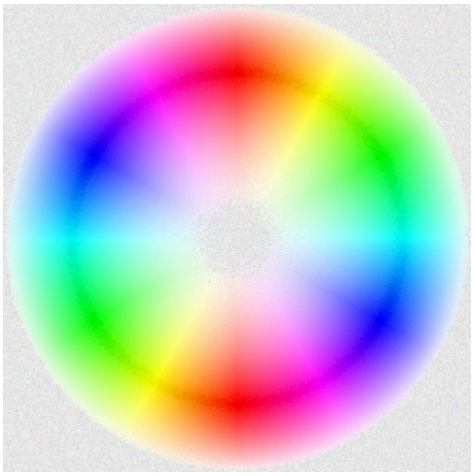

(b) Fiber orientation $\boldsymbol{v}_{\mathrm{DO}}$

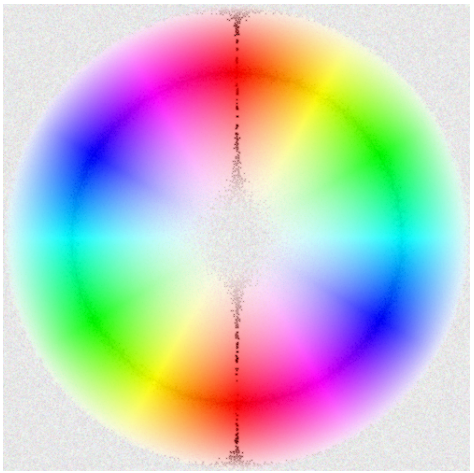

(c) Fiber orientation $\boldsymbol{v}_{\mathrm{DM}}(R = 1)$

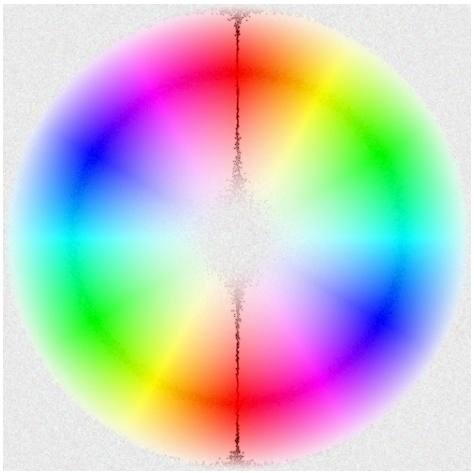

(d) Fiber orientation $\boldsymbol{v}_{+}$

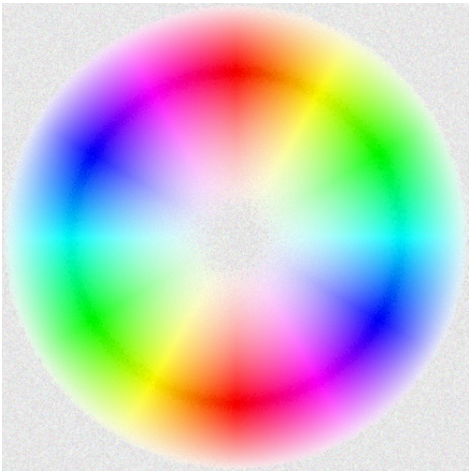

(e) Fiber orientation $\boldsymbol{v}_{\mathrm{GOP}}(\lambda = 0.2)$

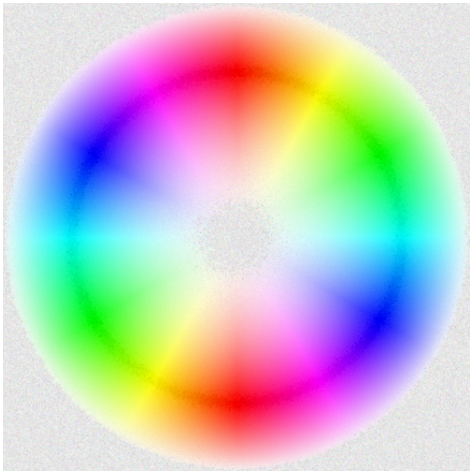

(f) Fiber orientation $\boldsymbol{v}_{\mathrm{GOF}}(\lambda = 0.4)$

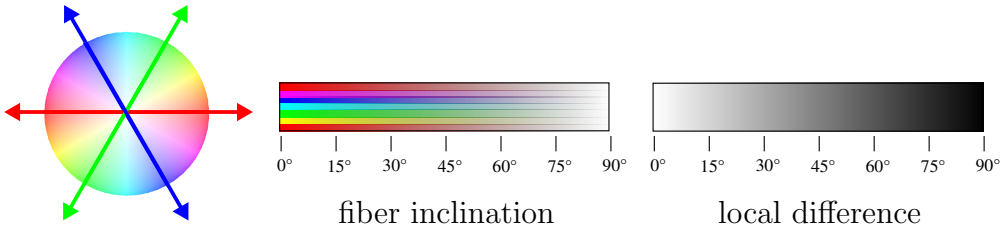

Figure 4.7: The fiber orientation is colored in the HSV color coding defined in (4.17)-(4.19). The fiber orientations $\boldsymbol{v}_{+}$ and $\boldsymbol{v}_{\mathrm{DM}}$ show an undesired vertical edge. This corresponds to the transition of the direction angle from 0° to 180° and the simultaneous change of the inclination sign in the true vector field (compare to Fig. 3.4). The fiber orientations $\boldsymbol{v}_{\mathrm{DO}}$, $\boldsymbol{v}_{\mathrm{GOP}}$ and $\boldsymbol{v}_{\mathrm{GOF}}$ do not show visible differences. There is a very modest noise in the center region compared to ground truth.

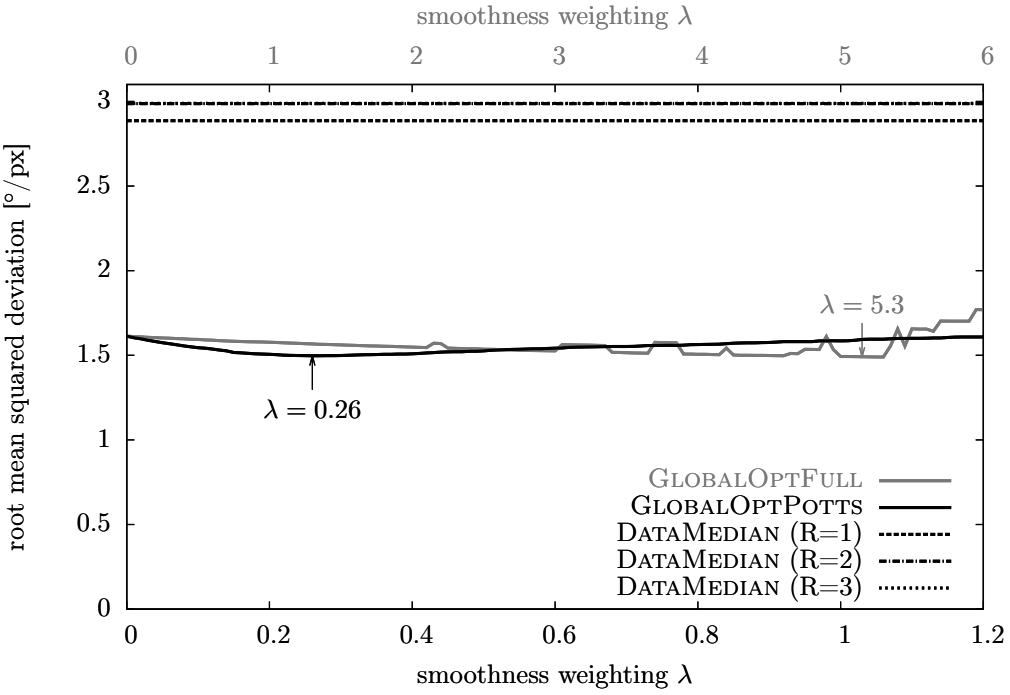

Figure 4.8: The root mean squared deviation (RMSD) measures the difference between the true synthetic vector field and the vector field reconstructed from simulated measurements. The minimal values are achieved by GlobalOptPotts at $\lambda = 0.26$ and GlobalOptFull at $\lambda = 5.3$.

not show any improvements compared to DataOnly with increasing errors for increasing radius R.

The sensitivity of both GlobalOpts to determine the correct inclination sign at pixels, that are not classified correctly by DataOnly, is examined in Fig. 4.9. GlobalOptPotts achieves a sensitivity of 50% at $\lambda = 0.35$ and almost 60% at $\lambda = 1.0$ (Fig. 4.9a), whereas GlobalOptFull hardly reaches only 25% at $\lambda = 3.9$ and stays under 50% even at $\lambda = 10$ (Fig. 4.9b).

The optimization of GlobalOptFull left less than 0.01% unlabeled in the synthetic data set (for $\lambda \leq 6$).

Human Brain Data DataMedian introduces undesired artifacts into the vector field at $0° - 180°$ transitions of the fiber direction, that also occur in AllPos (Fig. 4.10). Both GlobalOptPotts, GlobalOptFull, and

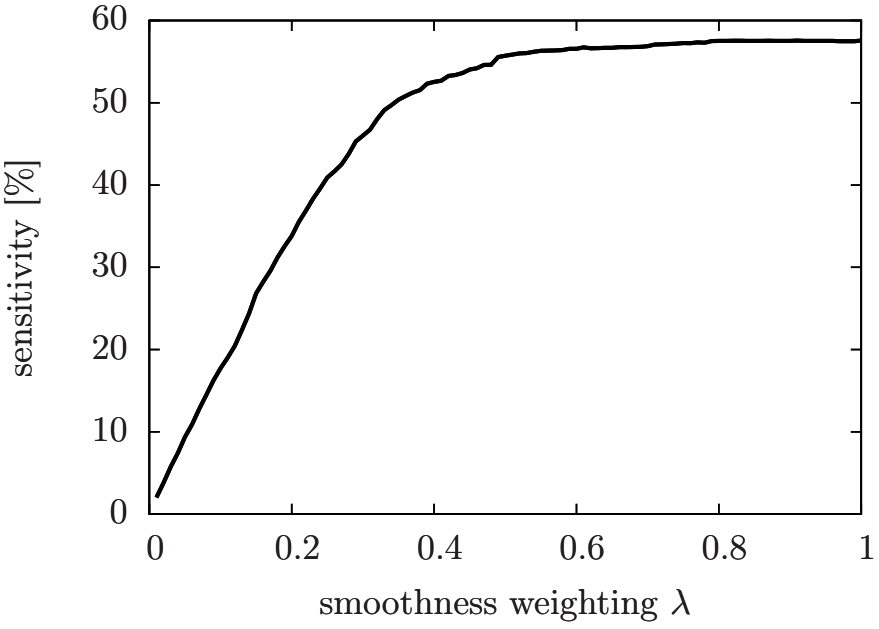

(a) Sensitivity of GlobalOptPotts

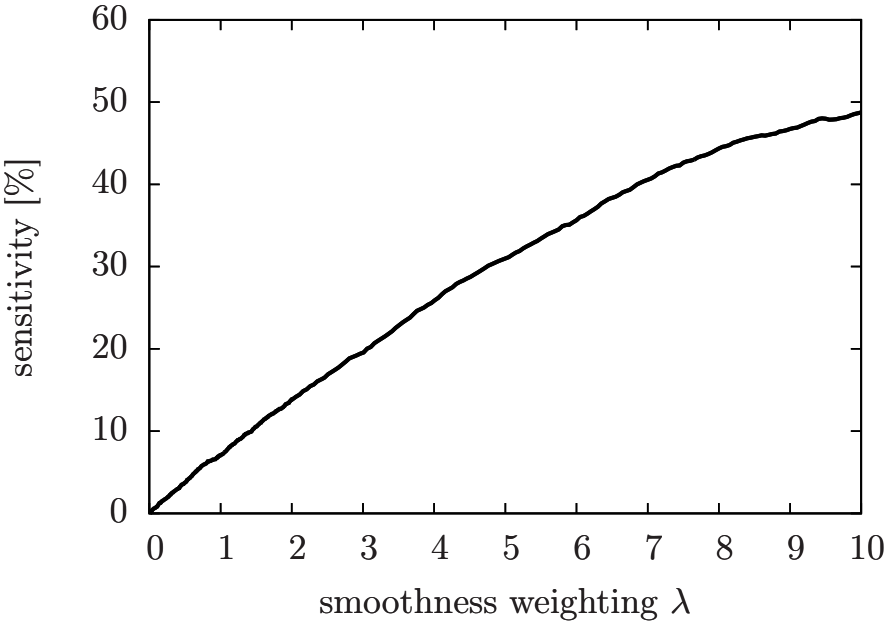

(b) Sensitivity of GlobalOptFull

Figure 4.9: The sensitivity of GlobalOptPotts to detect pixels with wrong inclination signs in the resulting sign map of DataOnly is clearly higher than for GlobalOptFull, which hardly reaches 60%, even for values of λ of up to 10.0. However, the sensitivity does not differentiate pixels according to the size of the error they produce in the vector field.

DataMedian are able to smooth regions that appear very inhomogeneous in DataOnly (Figs. 4.11, 4.12). The weighting factors $0.1 - 0.3$ and $0.2 - 0.6$ were selected manually. GlobalOptPotts with $\lambda = 0.2$ and analogously GlobalOptFull eliminate noise on an equal and reasonable level. Higher smoothness weighting factors, such as $\lambda = 0.3$ and $\lambda = 0.6$ respectively, remove important details of the vector field by smoothing. Lower smoothing weighting factors, such as $\lambda = 0.1$ and $\lambda = 0.2$ respectively, leave more noise in the vector field.

The L-curve, which plots the smoothness energy against the data energy, is shown in Fig. 4.13. It does not show a clear corner, but there are ranges of λ, where the curvature seems higher than in the rest of the curve. The estimated regions are marked at $0.15 \leq \lambda \leq 0.25$ for GlobalOptPotts and at $0.3 \leq \lambda \leq 0.5$ for GlobalOptFull.

The optimization of GlobalOptFull left an increasing number of pixels unlabeled for increasing values of λ as shown in Fig. 4.14.

4.3 Discussion

The results show that the inclination sign derived from the tilted measurements can be further improved by optimizing energy functions defined on a Markov random field. The data energy, that controls the agreement with the tilted measurements is balanced against the smoothness energy, that removes noise in regions where tilting yields only small changes. However, this balance must be done carefully. In real human brain data, the optimal result is not obvious, because the true inclination sign cannot be determined. However, the subjective evaluation of human real data, and the observation of the L-curve, come to similar conclusions for the weighting factor λ. The L-curve on real data suggests a value of $0.15 - 0.25$ and $0.3 - 0.5$ respectively, the manual inspection of the selected regions of interest suggest a value around 0.2. The results on synthetic data suggest a weighting factor of $\lambda = 0.26$ for GlobalOptPotts. The best weighting factor of GlobalOptFull is $\lambda = 5.3$, but the curve of the RMSD values shows, that the error becomes volatile for $\lambda > 2$. This underlines, that the weighting factor must be chosen with care and controlled by manual inspection. In doubt, a lower weighting factor

should be preferred. A smoothness weighting value of $\lambda = 0.2$ and $\lambda = 0.3$ respectively ensures high influence of the measured data opposed to the degree of necessary smoothing. The regularization parameter is known to vary with the level of noise in the data [32]. Therefore, if the measurement environment changes, the level of noise and the choice of the regularization parameter λ will have to be reviewed. For the current experimental situation, a smoothness weighting factor of $\lambda = 0.2$ is recommended with GlobalOptPotts.

The differences between both proposed smoothness energy functions used in GlobalOptPotts and GlobalOptFull do not seem relevant in real data. In order to achieve similar results, the weighting factor is chosen twice as high in GlobalOptFull as in GlobalOptPotts. The relation of both weighting factors, which were chosen manually, also seem to fit for the course of the L-curve. The disadvantage of GlobalOptFull to leave pixels unlabeled is negligible for $\lambda \leq 1.0$, i.e. in the reasonable range for human brain data. Although GlobalOptFull is more sophisticated and includes more knowledge about the kind of desired smoothness, it hardly achieves better results on synthetic data. Additionally, the results achieved with GlobalOptFull are less stable for increasing weighting factors and the sensitivity of GlobalOptFull to detect wrong pixels is not satisfactory in comparison to the sensitivity of GlobalOptPotts. However, the sensitivity does not differentiate pixels according to the size of their error. Therefore, the sensitivity is less meaningful than the RMSD.

In Sections 2.5 and 3.2.2, the accuracy of the absolute inclination angle is discussed. The overestimated or underestimated inclination angle should be kept in mind, when interpreting three-dimensional fiber orientations. The HSV visualization of the corpus callosum shows a strong edge of local differences for smoothed results, also for the results of GlobalOptFull. In the corpus callosum, the exact angle of the incoming fiber tracts from both hemispheres to each other is not known, but the shape of the corpus callosum suggests that the connecting fibers are not inclined in the median plane. However, the overestimated inclination angle explains the high inhomogeneity in this region. Until the biased absolute inclination values are not corrected effectively, GlobalOptPotts should clearly be preferred to GlobalOptFull. However, there are approaches to compensate for this bias (Chapter 6),

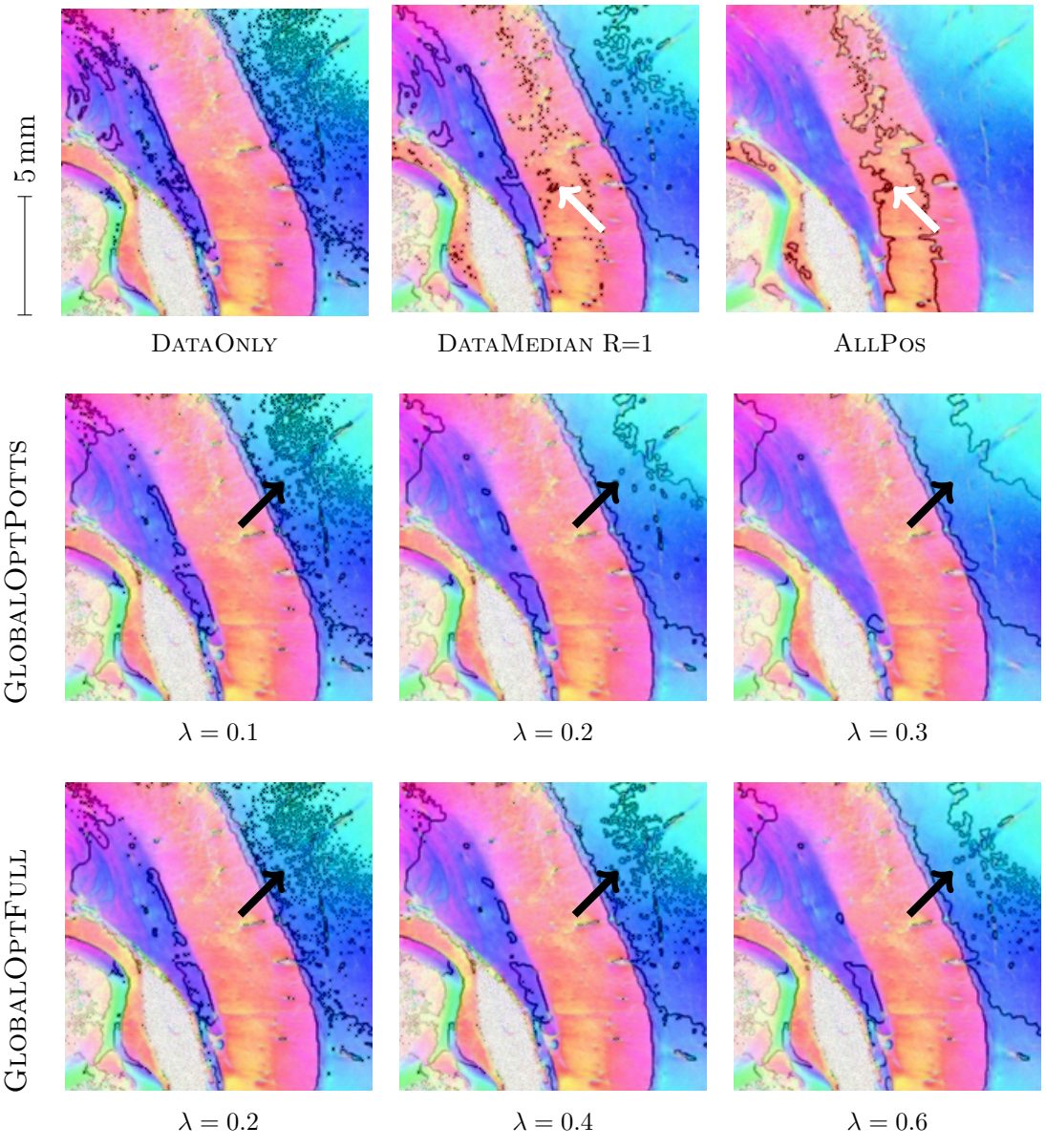
5 mm
DataOnly
DataMedian R=1
AllPos
GlobalOptPotts
λ = 0.1
λ = 0.2
λ = 0.3
GlobalOptFull
λ = 0.2
λ = 0.4
λ = 0.6

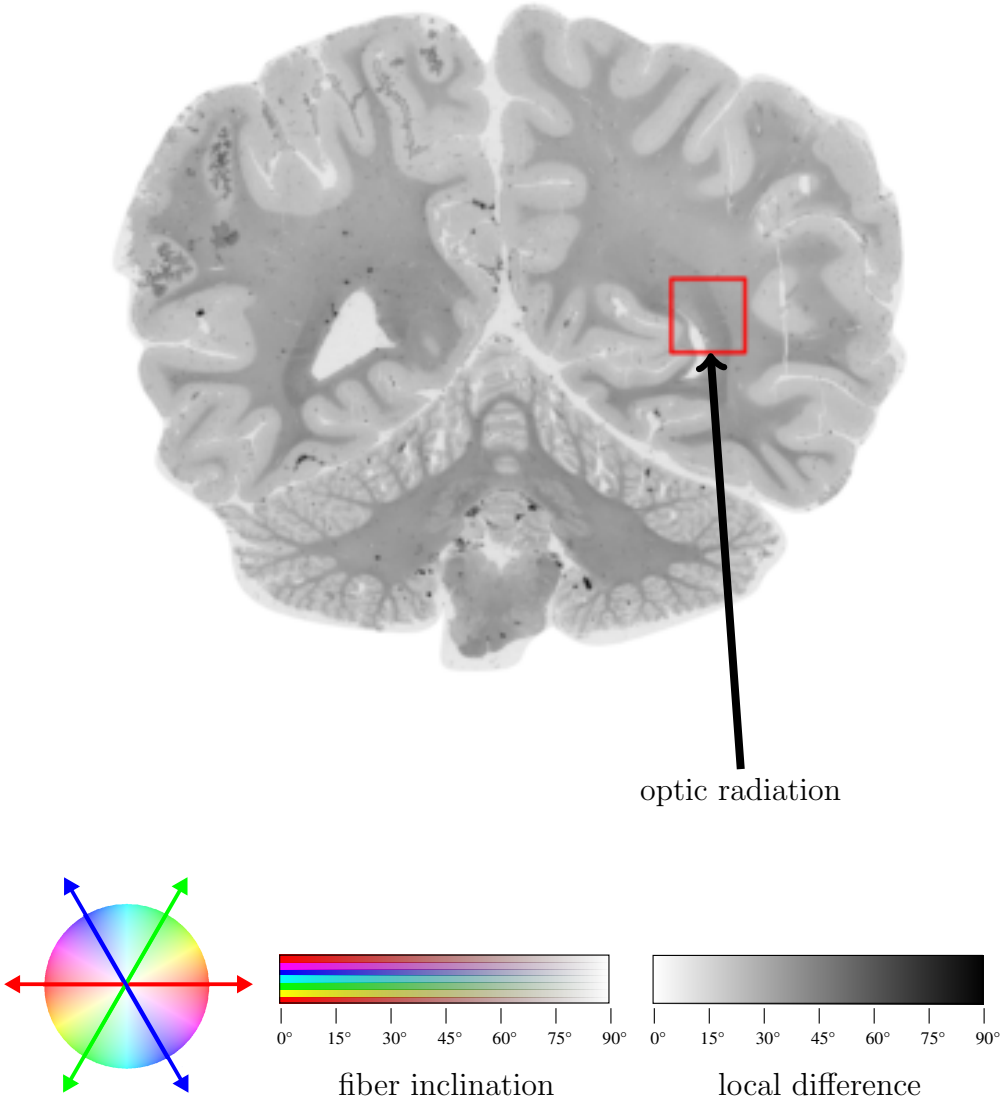

Figure 4.10: The optic radiation shows that DataMedian and AllPos show strong inhomogeneities in the vector field at $0° - 180°$ transitions (white arrow). The results of the energy minimization approaches are smooth in these regions. A stronger weighting of the smoothness energy smoothes the background (black arrow).

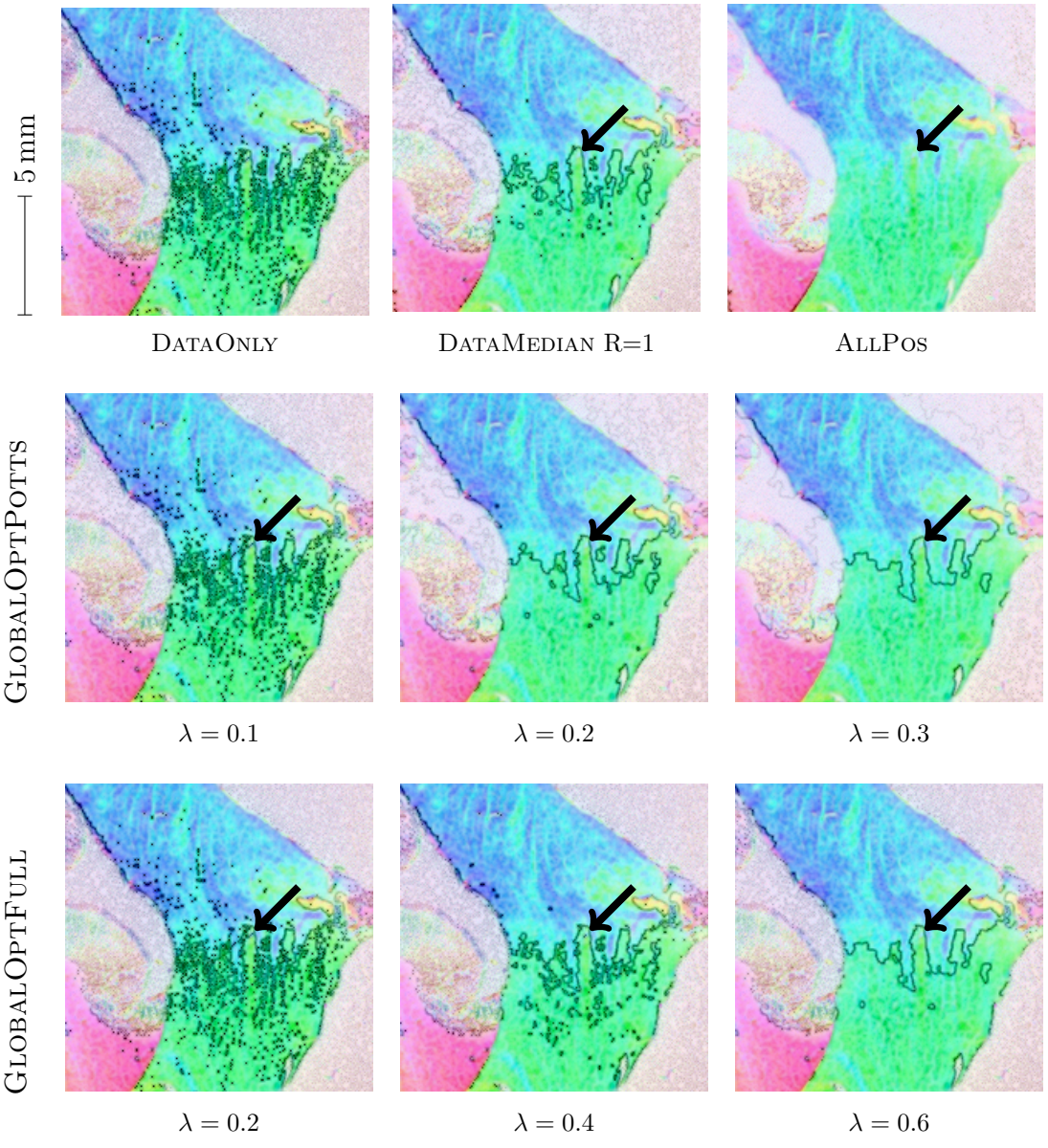
5 mm
DataOnly
DataMedian R=1
AllPos
GlobalOptPotts
λ = 0.1
λ = 0.2
λ = 0.3
GlobalOptFull
λ = 0.2
λ = 0.4
λ = 0.6

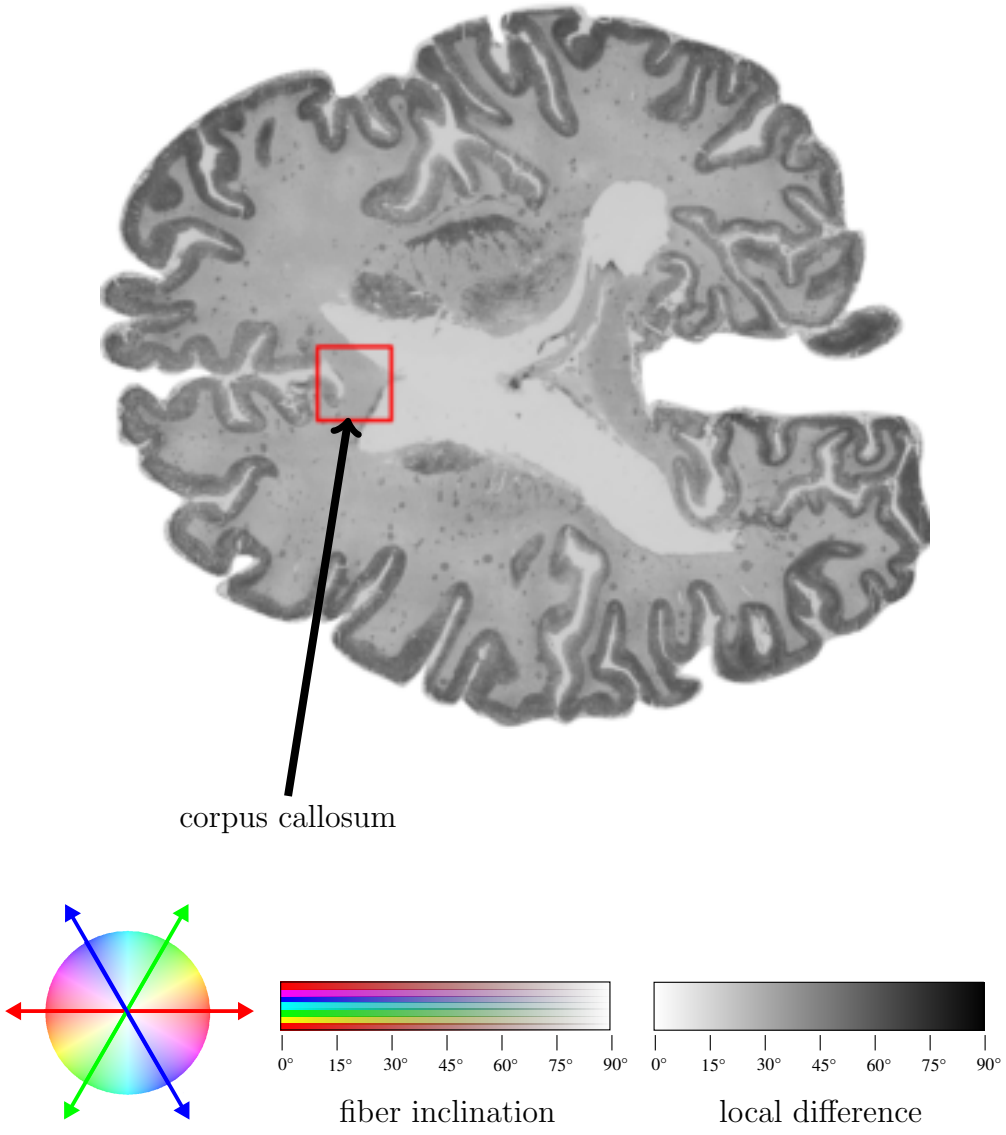

Figure 4.11: The resulting vector fields in the corpus callosum demonstrate the benefit of global optimization. Reasonable values for λ seem to be $\lambda = 0.2$ for GlobalOptPotts and $\lambda = 0.4$ for GlobalOptFull. Smoothing becomes too dominant for $\lambda = 0.3$ and $\lambda = 0.6$ respectively. Although AllPos shows the most homogeneous vector field, the correctness of the underlying, strictly positive inclination signs must be in doubt.

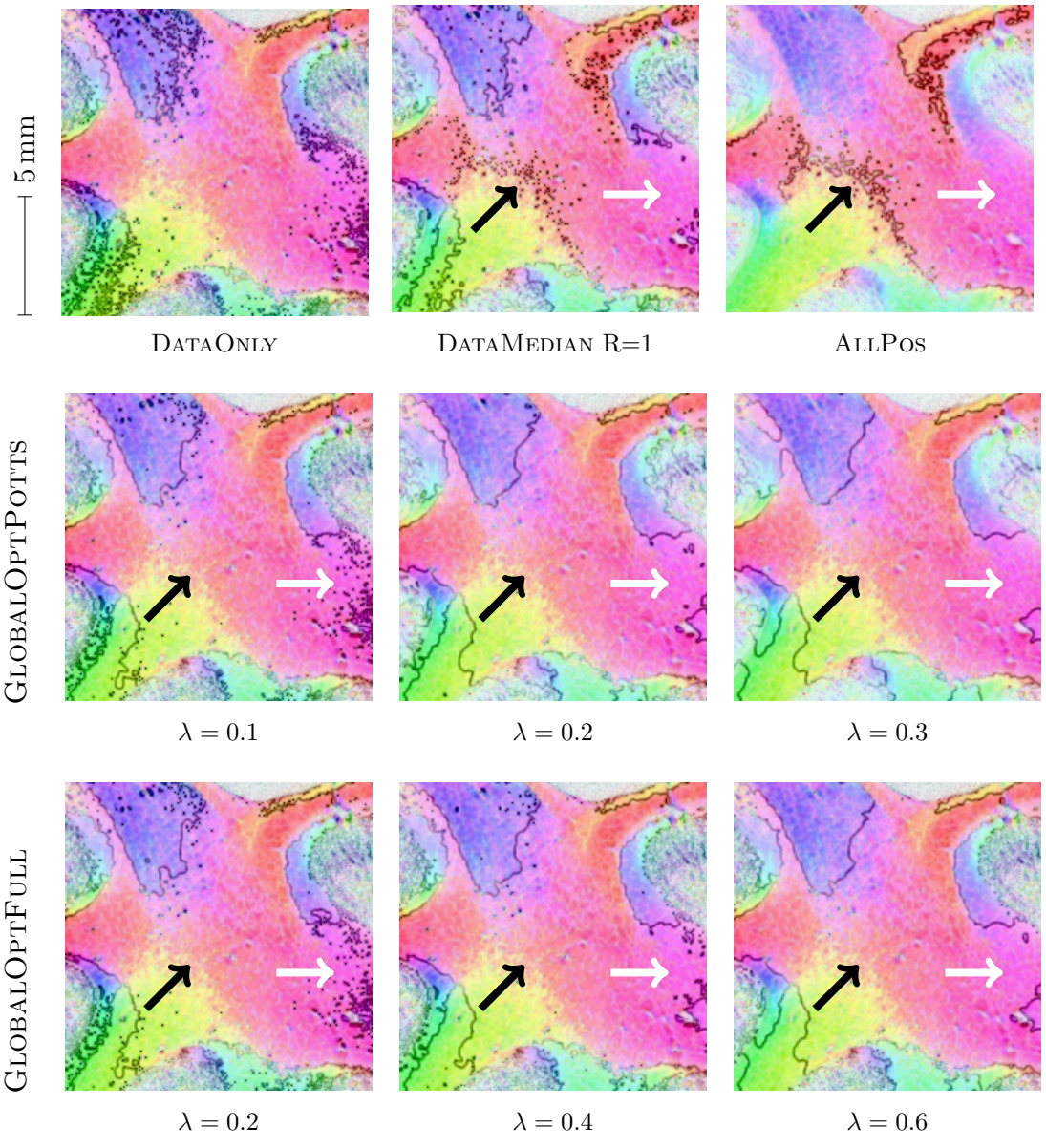
5 mm
DataOnly
DataMedian R=1
AllPos
GlobalOptPotts
λ = 0.1
λ = 0.2
λ = 0.3
GlobalOptFull
λ = 0.2
λ = 0.4
λ = 0.6

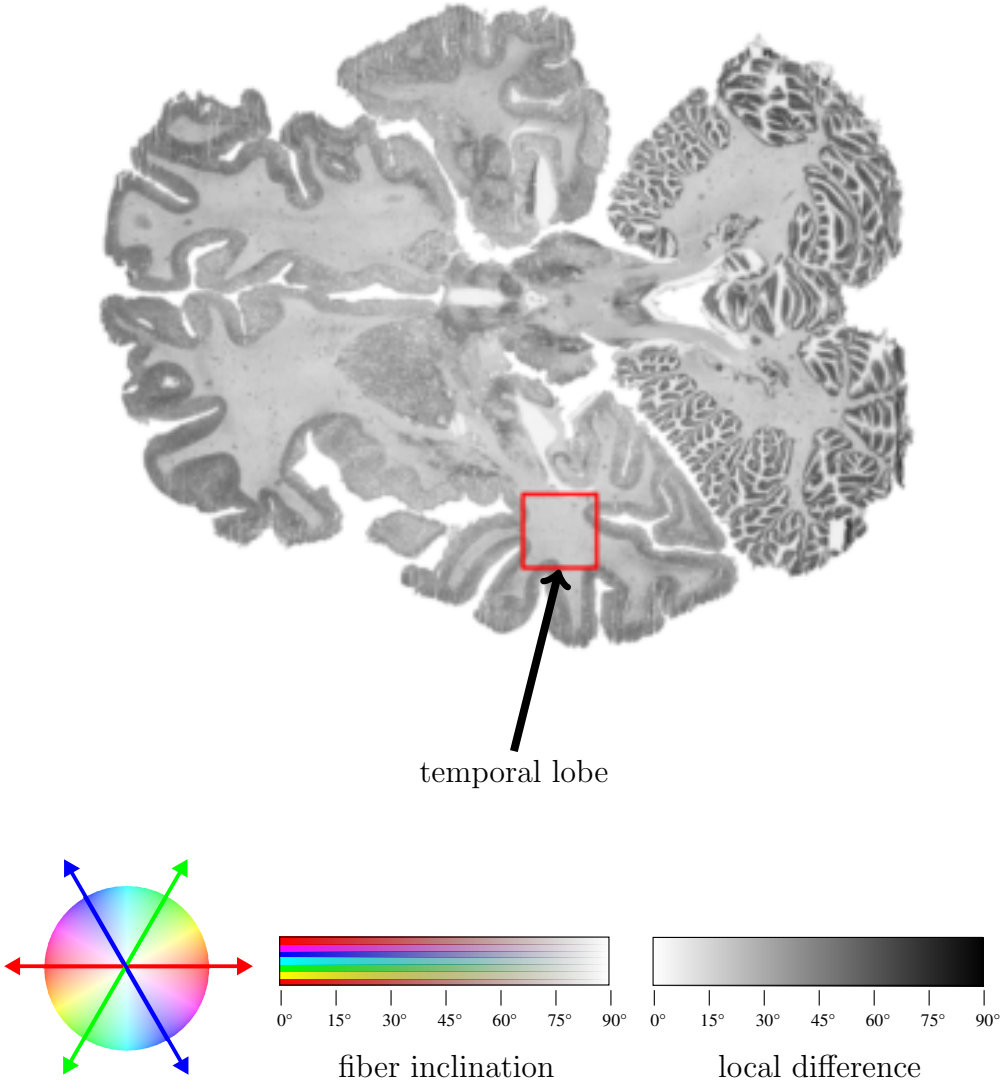

Figure 4.12: In this region in the temporal lobe, there are obvious differences between the different methods. There are artifacts in AllPos and Data-Median in $0° - 180°$ transitions as in the optic radiation in Fig. 4.10 (black arrows). And there is a smoothing of strong discontinuities in the vector fields such as in the corpus callosum (Fig. 4.11) (white arrows).

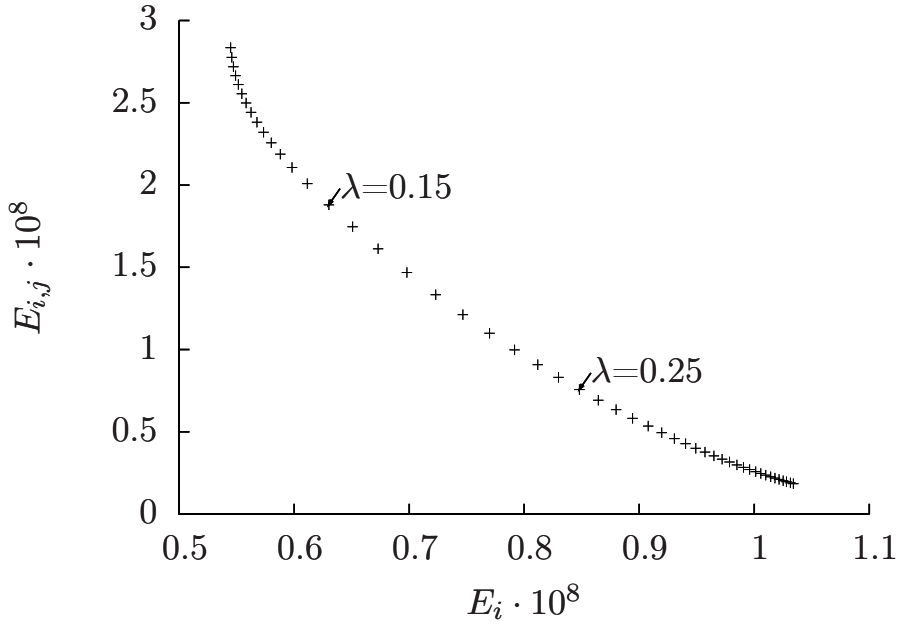

(a) GlobalOptPotts real data

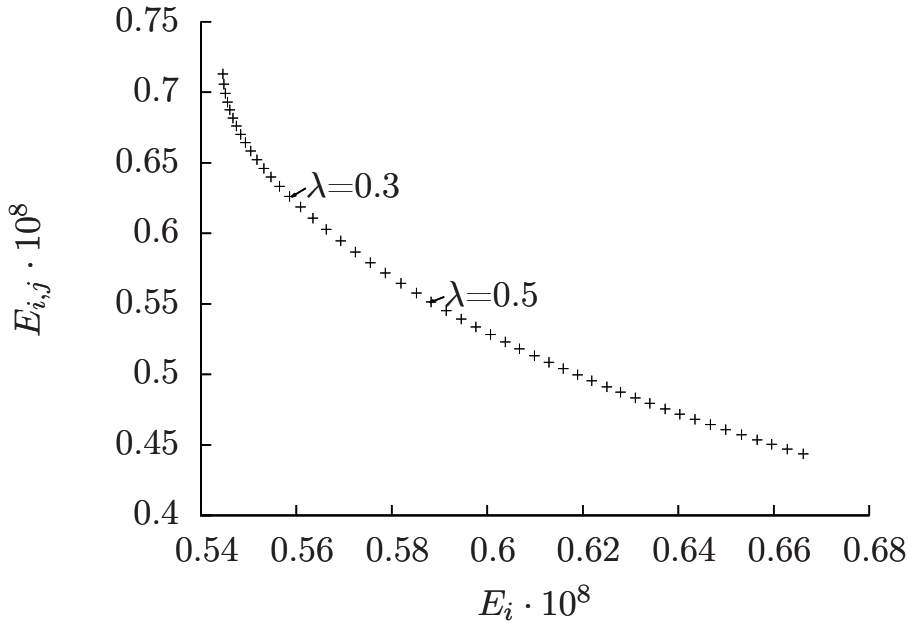

(b) GlobalOptFull real data

Figure 4.13: The L-curve visualizes the trade-off between the data energy and smoothness energy function for different values of the regularization parameter λ. A good choice for λ is where there is a high curvature.

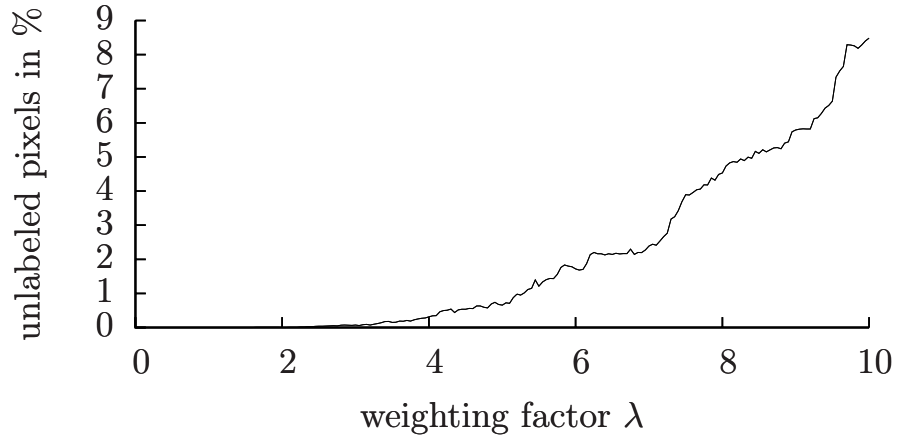

Figure 4.14: The efficient optimization of a non-submodular function does not guarantee to provide a complete result. In the examined human brain section, an increasing number of pixels is left unlabeled by the quadratic pseudo-boolean optimization (QPBO) algorithm.

and then GlobalOptFull should be reconsidered.

In human brain data, the most obvious errors of DataMedian appear, where the fiber direction φ flips from 180° to 0° or vice versa inside a continuous fiber structure. DataMedian does not consider the fiber direction. This is obviously the source of the artifacts, that are observed in the optic radiation and the selected region in the temporal lobe. Artifacts also appear for AllPos in these 180°-0°-transition regions. GlobalOptPotts uses the fiber direction to control smoothing and thereby is able to guarantee a good solution in 180°-0°-transition regions.

The terms *smoothing* and *regularization* have been used synonymously. The term *regularization* is frequently used in the context of optimization problems, while the term *smoothing* is often associated with blurring and information loss. Here, smoothing is applied in a very constrained and distinct way, that improves the resulting inclination sign by considering knowledge about the data and suppressing noise.

The improvement of GlobalOptPotts compared to DataOnly is very small on synthetic data. This poses the question, whether the intricate

optimization step is really necessary. On real data, the improvement is more obvious. A number of influences on the data during tilting, such as modified reflection angles and interpolation errors during the perspective back-transformation, have not been modelled in the simulation, yet. In a previous study [74], a different synthetic data set was evaluated, showing larger improvements in terms of the RMSD. The application of noise was performed to the retardation and direction images directly, which possibly yields more noise, than the more realistic application of noise to the PLI image series, which was implemented here. All of these influences must be examined in future to reevaluate the quality of the derived and optimized inclination sign.

Chapter 5

PLI Tractography

The term *tractography*, also referred to as *fiber tracking*, denotes a group of algorithms that reconstruct nerve fibers from orientational measurements. Since the measurement of the diffusion orientation has become possible with diffusion-weighted magnetic resonance imaging (DW-MRI), a considerable number of tractography algorithms has been developed. The existing algorithms are reviewed in Section 5.1. Tractography algorithms based on Bayesian inference are a convenient approach to consider measurement uncertainties during tractography. Therefore, this approach is also promising for 3D-PLI and is described with more detail, including an introduction into the methodology. In Section 5.2, a tractography algorithm based on Bayesian inference is developed for PLI. This includes the formalization of a fiber propagation model and a measurement model. Bayesian inference is performed by particle filtering, a Monte Carlo type method. In Section 5.3, the developed tractography algorithm is evaluated on a synthetic data set in comparison to a standard streamline algorithm.

5.1 Tractography Algorithms for DW-MRI

A large and heterogeneous set of tractography algorithms for DW-MRI has been published until today. When DW-MRI was in its infancy, only a few gradient measurements were composed to a diffusion tensor. The simplicity of the measurement has made diffusion tensor imaging (DTI) to the most

widely applied method for the reconstruction of DW-MRI measurements. However, a diffusion tensor only resolves one principal direction [11]. During the past years, new measurement protocols, such as high angular resolution diffusion imaging (HARDI) [127] and diffusion spectrum imaging (DSI) [133] have pushed the use of more complex diffusion models, such as the partial volume model [13], the composite hindered and restricted diffusion model [3], multiple tensor models [50], or the orientation distribution functions (ODFs) [52], which are typically expressed with spherical harmonics as basis functions. There are numerous methods that reconstruct ODFs from diffusion measurements [4], and various basis functions have been used [108], which are not discussed here.

The quantitative evaluation of tractography algorithms based on DW-MRI is difficult, because there is no alternative method to assess the nerve fiber orientation in vivo. Therefore, evaluation is commonly done by visual inspection, which may be subjective or misleading, or on synthetic data, which may not be realistic. In many cases, it is not decidable, which algorithms produce the most correct fiber reconstructions. The most useful comparison of tractography algorithms, has been performed on a phantom in the context of a competition, the Fiber Cup 2009 [39].

5.1.1 Classification of Tractography Algorithms

Traditionally, tractography algorithms have been classified either as deterministic (Table 5.1) or probabilistic (Table 5.2). The first tractography algorithms were deterministic [93], [29]. These algorithms are also called line propagation or streamline algorithms, because a line is constructed beginning at a seed point by following the local fiber orientation. In DTI [11], the fiber orientation is determined as the principal direction of the diffusion tensor. There are algorithms that step through the vector field continuously and those that step from voxel to voxel, limiting the number of possible orientations by the number of neighbors [35]. Tensor deflection [84] and tensor advection [134] take the shape of the diffusion tensor and the previously tracked fiber direction into account, when determining the next local fiber orientation. Recently, deterministic tractography algorithms were extended by the use

of more complex diffusion models such as two tensor models [50], [106] and multiple mixture models [119], higher order tensors [63], or by the use of orientation distribution functions [133], [33]. Especially, the method to extract single fiber orientations from fiber mixtures has been varied [115], [119].

The first probabilistic tractography algorithms were presented by Parker [100] and Behrens [13]. Kang [73] propagated a diffusion front. Perrin [101], Descoteaux [33] and Koch [77], beginning at a seed point, tracked multiple orientations simultaneously according to the fiber orientation probability. These tracts are often called particle trajectories. By counting the number of arriving particle trajectories, probabilistic tractography algorithms are able to construct connectivity matrices, defining a probability of connectivity between the seed point and all other voxels. However, there are also probabilistic tractography algorithms, that construct a single fiber path instead of connectivity matrices. The term probabilistic or stochastic is then used, because each path is assigned with a measure of uncertainty, but not necessarily all possible fiber paths are explored. Uncertainty can be estimated by bootstrapping of repeated diffusion measurements [83], [69], [58], [17], [68], [132]. Complex fiber models have also been used in probabilistic tractography algorithms [14], [17], [68].

Further probabilistic tractography algorithms estimate the fiber orientation as a dynamic state, with a prior probability distribution and an observation likelihood, which describes the agreement of the estimated state with the measured fiber orientations. The estimation is inferred from these probability distributions with Bayes' Theorem. The approach is also called state-space-modeling and will be explained in more detail in Section 5.1.2. Although Behrens also used Bayesian inference [13], [14], his tractography approach is not classified there, because a non-informative prior is used, i.e. the prior distribution does not influence the estimated state.

Besides deterministic and probabilistic algorithms, further classes of algorithms have emerged (Table 5.3). Optimization algorithms find the optimal path between two given points, e. g. [117], [37]. These approaches are very closely related to global tractography algorithms, that optimize an arrangement of fiber tracts in the complete orientation field at once [28], [80], [128], [40], [1], [109], [137]. The global optimization algorithms clearly have the

Table 5.1: Local deterministic tractography approaches
(HO-tensor = higher order tensor, m-tensor = multiple tensor)

author [Ref]	**diffusion model**	**comment**
Mori 1999 [93]	tensor	streamline
Conturo 1999 [29]	tensor	streamline
Weinstein 1999 [134]	tensor	tensor advection
Basser 2000 [11]	tensor	streamline
Zhukov 2002 [140]	tensor	previous regularization
Lazar 2003 [84]	tensor	tensor deflection
Hlawitschka 2005 [63]	HO-tensor	HO-tensor lines
Guo 2006 [50]	2-tensor	multiple tensor deflection with branching
Duru 2007 [35]	tensor	stack algorithm
Wedeen 2008 [133]	ODF	based on DSI
Qazi 2009 [106]	2-tensor	streamline
Singh 2010 [119]	m-tensor	separate fibers with ICA

highest potential to achieve the best tractography results, because they can consider the entire orientation information at once. In the Fiber Cup 2009 [39], the global tractography method outperformed all other algorithms. This advantage is gained by enormous computational challenges. For DW-MRI data, these have been overcome, such that computation time is reduced to hours on a standard PC [109].

The classification of 48 approaches to tractography (Tables 5.1-5.4) gives a broad overview of the variety of algorithms that have been developed. It is an attempt to find best practices. In some cases, algorithms could be assigned to another class as well, because aspects of multiple classes are found. There are other possibilities to classify tractography algorithms, but classifications similar to the one here have been proved useful in previous reviews [94], [8], [96], [65], [126].

Table 5.2: Local probabilistic tractography approaches
(2-comp = two compartment model, m-tensor = multiple tensor)

author [Ref]	**diffusion model**	**comment**
Parker 2001 [100]	tensor	front propagation
Koch 2002 [77]	tensor	particle trajectories
Behrens 2003 [13]	2-comp	Bayesian inference
Kang 2005 [73]	tensor	front propagation
Jones 2005 [69]	tensor	bootstrap
Lazar 2005 [83]	tensor	BOOT-TRAC
Perrin 2005 [101]	ODF	particle trajectories
Behrens 2007 [14]	m-tensor	Bayesian inference
Haroon 2007 [58]	ODF	wild bootstrap
Berman 2008 [17]	ODF	residual bootstrap
Descoteaux 2009 [33]	ODF	particle trajectories
Jeurissen 2011 [68]	ODF	residual bootstrap
Vorburger 2013 [132]	tensor	BootGraph

Table 5.3: Global tractography approaches (m-tensor = multiple tensor, CHARMED = composite hindered and restricted model of diffusion)

author [Ref]	**diffusion model**	**comment**
Sherbondy 2008 [117]	tensor	ConTrack
Feng 2011 [37]	tensor	ant colony optimization
Tuch 2001 [128]	ODF	connectivity matrix, based on DSI
Cointepas 2002 [28]	2-tensor	spin-glass model
Kreher 2008 [80]	m-tensor	Gibbs tracking
Fillard 2009 [40]	ODF	spin-glass model
Wu 2009 [137]	tensor	GeneTrack
Sherbondy 2010 [118]	CHARMED	MicroTrack
Aganj 2011 [1]	ODF	Hough transform
Reisert 2011 [109]	m-tensor	line segments

5.1.2 Tractography Based on Bayesian Inference

An increasing number of tractography algorithms use stochastic models to estimate the fiber orientation from measurements and prior knowledge. The combination of both measurement and prior knowledge can be expressed as a special form of Bayes' Theorem ([34, p. 6], [2]).

Theorem 5.1.1 (Bayes' Theorem) *Given the previous state $\boldsymbol{x}_{k-1}$ and a new measurement $\boldsymbol{y}_k$, the probability of the next state $\boldsymbol{x}_k$ can be inferred as*

$$p(\boldsymbol{x}_k \mid \boldsymbol{y}_k, \boldsymbol{x}_{k-1}) = \frac{p(\boldsymbol{y}_k \mid \boldsymbol{x}_k) \cdot p(\boldsymbol{x}_k \mid \boldsymbol{x}_{k-1})}{\int p(\boldsymbol{y}_k \mid \boldsymbol{x}_k) \cdot p(\boldsymbol{x}_k \mid \boldsymbol{x}_{k-1}) \, \mathrm{d}\boldsymbol{x}_k}$$

The probability $p(\boldsymbol{x}_k \mid \boldsymbol{x}_{k-1})$ is called *prior distribution*, $p(\boldsymbol{y}_k \mid \boldsymbol{x}_k)$ is called *observation likelihood*, and the resulting probability $p(\boldsymbol{x}_k \mid \boldsymbol{y}_k, \boldsymbol{x}_{k-1})$ is denoted as the *posterior distribution*. The random variables are indexed with a time index k, that allows to repeatedly calculate the posterior probability for new incoming measurements $\boldsymbol{y}_k$ at time point k. The *maximum a posteriori* (MAP) denotes an optimal estimation for state $\boldsymbol{x}_k$ by maximizing the posterior distribution.

Generally, $p(\boldsymbol{x}_k \mid \boldsymbol{y}_k, \boldsymbol{x}_{k-1})$ cannot be computed exactly because of the integral in the marginal distribution $\int p(\boldsymbol{y}_k \mid \boldsymbol{x}_k) \cdot p(\boldsymbol{x}_k \mid \boldsymbol{x}_{k-1}) \, \mathrm{d}\boldsymbol{x}_k$. This can be overcome either by approximation or by limitation to specific types of distributions.

The repeated estimation of dynamic states $\boldsymbol{x}_k$ by Bayesian inference is also known as state-space-modeling. The prior distribution is generally derived from a process model with noise $\boldsymbol{v}_k$.

$$\boldsymbol{x}_k = f(\boldsymbol{x}_{k-1}, \boldsymbol{v}_k) \tag{5.1}$$

The observation likelihood is derived from a measurement model with noise $\boldsymbol{w}_k$.

$$\boldsymbol{y}_k = h(\boldsymbol{x}_k, \boldsymbol{w}_k) \tag{5.2}$$

The most common state-space model is the Kalman filter, which requires f and h to be linear, and $\boldsymbol{v}_k$ and $\boldsymbol{w}_k$ to be normally distributed. A simple recursive algorithm directly provides the exact MAP solution for each time point k [135]. The Kalman filter has been extended for non-linear functions

Table 5.4: Probabilistic tractography algorithms based on Bayesian inference (Watson = Watson distribution function, m-tensor = multiple tensor, 2-comp = two compartment model)

author [Ref]	**diffusion model**	**comment**
Friman 2006 [42]	tensor	Bayesian inference
Gössl 2002 [46]	tensor	Kalman filter
Imperati 2009 [64]	tensor	Extended Kalman filter
Malcolm 2009 [91]	2-tensor	Unscented Kalman filter
Malcolm 2010 [89]	Watson	Unscented Kalman filter
Lienhard 2011 [86]	m-tensor	Unscented Kalman filter
Björnemo 2002 [19]	tensor	particle filter
Jbabdi 2007 [66]	2-comp	particle filter, fMRI as prior
Zhang 2009 [139]	tensor	particle filter
Savadjiev 2010 [111]	ODF	particle filter, helicoid model
Yap 2011 [138]	Watson	particle filter
Pontabry 2011 [104]	ODF	particle filter

f and h by local linearization (extended Kalman filter) [2], or by non-linear transformation of sample points (unscented Kalman filter) [71]. In case of non-linear transformations and non-Gaussian distributions, the marginal distribution can be discretized by Monte Carlo methods. A set of particles is used to represent the probability distributions. Therefore, this discretization approach is also called particle filtering [34]. A particle filter does not only provide an MAP estimation in each step, but it also provides an estimate of the complete posterior distribution. Therefore, tractography with particle filters can provide probabilities for each generated particle trajectory.

Various tractography algorithms based on Bayesian inference have been published. In 2002, Gössl [46] introduced the Kalman filter to white matter tractography. The extended Kalman filter by Imperati [64] includes a non-linear measurement model. Malcolm et al. published numerous tractography approaches with an unscented Kalman filter [89, 90, 91, 92], that

use increasingly complex probability distributions. The use of a particle filter for tractography was first presented by Björnemo [19]. Savadjiev [111] implemented a particle filter with a geometrical fiber model based on helicoids [110]. Zhang et al. [139] presented a particle filter, which classifies the diffusion tensor and uses Mises von Fisher distributions. Friman [42] performed Bayesian inference by discretely sampling the complete state space.

5.2 Tractography Based on 3D-PLI

There are some important differences between 3D-PLI and DW-MRI that must be considered when a tractography algorithm is transferred from DW-MRI to 3D-PLI.

First, the orientational data, that is collected, is in a different format, has a slightly different meaning, and hence must be interpreted differently. DW-MRI signals provide the distance of diffusion in the given directions. 3D-PLI provides a single, unscaled direction per voxel. There is work in progress to combine the directional information of several 3D-PLI voxels into one larger voxel in order to create an ODF. This could simplify the transfer of tractography algorithms. However, many DW-MRI based tractography algorithms reduce the acquired orientational information to the normalized principal eigenvector of the diffusion tensor. In this case, the data format can be transferred more easily.

Second, the measurement uncertainty is very different. In DW-MRI measurements, there is also diffusion orthogonal to the fiber axis, which generates a kind of background noise. In complex fiber constellations, diffusion takes place along multiple directions, which are measured as a mixed diffusion profile. In 3D-PLI, there is more measurement uncertainty in the out-of-plane angle, than in the in-plane angle.

Third, 3D-PLI operates on a scale of micrometers instead of millimeters. This considerably increases the size of data, that must be processed. Therefore, algorithms with a high complexity, such as global tractography algorithms, that run in acceptable time on DW-MRI data, exceed run time and memory limits on PLI data. The reduced voxel size in 3D-PLI leads to a reduced amount of voxels that contain multiple fiber populations. This

applies especially for the in-plane resolution of up to 1.6 μm provided by a polarizing microscope. Currently, the thickness of gross histological human brain sections is limited by tissue preparation for cryosectioning to approx. 60 μm. Smaller tissue samples, such as mouse or rat brains, can be sectioned even with a thickness of 30 μm providing acceptable quality. Consequently, mixed fiber orientations also appear in 3D-PLI, but fiber orientations are primarily mixed along the z-axis.

In the present work, a tractography algorithm based on a particle filter is developed for 3D-PLI. As all Bayesian approaches, the particle filter is able to combine measurements (observation likelihood) with regularity constraints (prior knowledge about fiber tracts) in order to track plausible fibers. Because of the differences between DW-MRI and 3D-PLI measurements, the observation likelihood must be adapted. In this way, prior knowledge can be used effectively to compensate for uncertainties in the measured 3D-PLI data.

The simulated measurement of synthetic fiber structures in Chapter 3 has shown, that the derived inclination angle is biased considerably by fiber orientation mixture and inhomogeneous myelination. Until now, neither the degree of fiber mixture nor the degree of myelination can be assessed reliably in real tissue. Without additional knowledge about fiber mixture and myelination, the errors of the inclination angle cannot be controlled. Therefore, the tractography algorithm presented here is restricted to two dimensions. Possibilities to assess the missing information are discussed in Chapter 6. The particle filter can be extended easily to three dimensions as soon as further information about fiber mixture and fiber myelination becomes available.

As discussed in Chapter 3, the uncertainty of the direction angle depends on the measured inclination angle α, which is accessible during tractography. The aim of the developed tractography approach is to account for this uncertainty and to find plausible fiber tracts.

The central part of a state-space model is the definition of the state space. For tractography, the essential information to be estimated is the fiber orientation. In this work, the estimated state consists of the in-plane fiber direction φ.

5.2.1 Prior Knowledge About Fiber Tracts

With very few exceptions, the prior density for tractography algorithms has been chosen to continue the previous fiber orientation [42, 64, 104, 139]. Tractography approaches with Kalman filters assume normal distributions as priors [46, 91, 89, 86]. However, this is a heuristic choice, which cannot be inferred from observations of real fiber tracts. It is commonly argued, that the prior density is used to enforce smoothness, which is observed in real fiber tracts. In this work, the prior density $p(\varphi_k \mid \varphi_{k-1})$ is also chosen as a normal distribution with zero mean and standard deviation σ_φ:

$$p(\varphi_k \mid \varphi_{k-1}) = \mathcal{N}(0, \sigma_\varphi) \tag{5.3}$$

However, as will be discussed in Section 5.3.2, such a prior density is at most a rough approximation of the true fiber course. The standard deviation σ_φ must be chosen according to the step length, because larger step lengths must allow larger deviations and smaller step lengths must restrict deviations further. The step length must not be chosen too large, because then small variations of the fiber orientation could be missed. If the step length is chosen too small, this may create artificial fiber tracts inside a single voxel. For this reason, the step length was chosen as 0.3 times the pixel size, which is $0.3 \cdot 64\,\mu\text{m} \approx 20\,\mu\text{m}$ for a large-scale polarimeter. The standard deviation σ_φ was varied in the experiments between 2° and 0.2°.

5.2.2 Observation Likelihood in PLI Data

The measurement model describes the relation between the measurement $\boldsymbol{y}_k = (\varphi_k^m,\, \alpha_k^m)$ and the state $\boldsymbol{x}_k = (\varphi_k,\, \alpha_k)$ to be estimated, expressed as an observation likelihood function $p(\varphi_k^m, \alpha_k^m \mid \varphi_k, \alpha_k)$. In Chapter 3, the experimental setup was simulated and the relation between the true fiber orientation and the measured fiber orientation was examined. The observation likelihood can be directly derived from the results of the simulation. The fiber in-plane direction angle φ and the out-of-plane inclination angle α are derived differently and with different accuracy. Therefore, the observation probability must be considered separately for both components.

In this work, the observation likelihood is restricted to the estimated fiber direction angle. The density $p(\varphi^m, \alpha^m \mid \varphi)$ is approximated piecewise by normal distributions $\mathcal{N}(0, \sigma)$ with zero mean and standard deviation σ and a uniform distribution $\mathcal{U}[a, b]$ in the interval $[a, b]$:

$$p(\varphi_k^m, \alpha_k^m \mid \varphi_k) = \begin{cases} \mathcal{N}(0, 0.3^\circ + \frac{1.0}{60} \cdot |\alpha_k^m|) & , 0^\circ \leq |\alpha_k^m| \leq 60^\circ \\ \mathcal{N}(0, 1.3^\circ + \frac{1.4}{70} \cdot |\alpha_k^m|) & , 60^\circ < |\alpha_k^m| \leq 70^\circ \\ \mathcal{N}(0, 2.7^\circ + \frac{1.5}{75} \cdot |\alpha_k^m|) & , 70^\circ < |\alpha_k^m| \leq 75^\circ \\ \mathcal{N}(0, 4.2^\circ + \frac{5.4}{80} \cdot |\alpha_k^m|) & , 75^\circ < |\alpha_k^m| \leq 80^\circ \\ \mathcal{N}(0, 9.6^\circ + \frac{24}{85} \cdot |\alpha_k^m|) & , 80^\circ < |\alpha_k^m| \leq 85^\circ \\ \mathcal{U}[-90^\circ, 90^\circ] & , 85^\circ < |\alpha_k^m| \leq 90^\circ \end{cases} . \tag{5.4}$$

The standard deviation is increased piecewise linearly from 0.3° to 33.6°. This corresponds to the empirical standard deviations determined from the simulations (Fig. 3.9a). The approximated observation likelihood function is illustrated together with the simulated measurements in Fig. 5.1.

5.2.3 Particle Filtering

The particle filter denotes a class of methods that are also known as sequential Monte Carlo methods. The general idea is that a set of particles represents a probability distribution. The process model transforms the particle set, while the observation likelihood is used for weighting the particles. The filter starts with a set of N particles, that are sampled from an initial distribution at a given seed point. Each particle is initialized with a weight $1/N$. Here, the initial distribution was chosen to be derived from the measured fiber orientation at that starting point. Then, in each time step k, all particles are propagated by the linear process model. In the next step, the particles are reweighted according to their observation likelihood. After a few iterations, the particle weights may degenerate, such that a single particle has the maximum weight and all other particles have a minimum weight. Degeneracy cannot be avoided, because reweighting automatically increases the variance of the weights. Therefore, resampling must be performed regularly. The resampling scheme shown in Algorithm 2, which is applied here, was taken

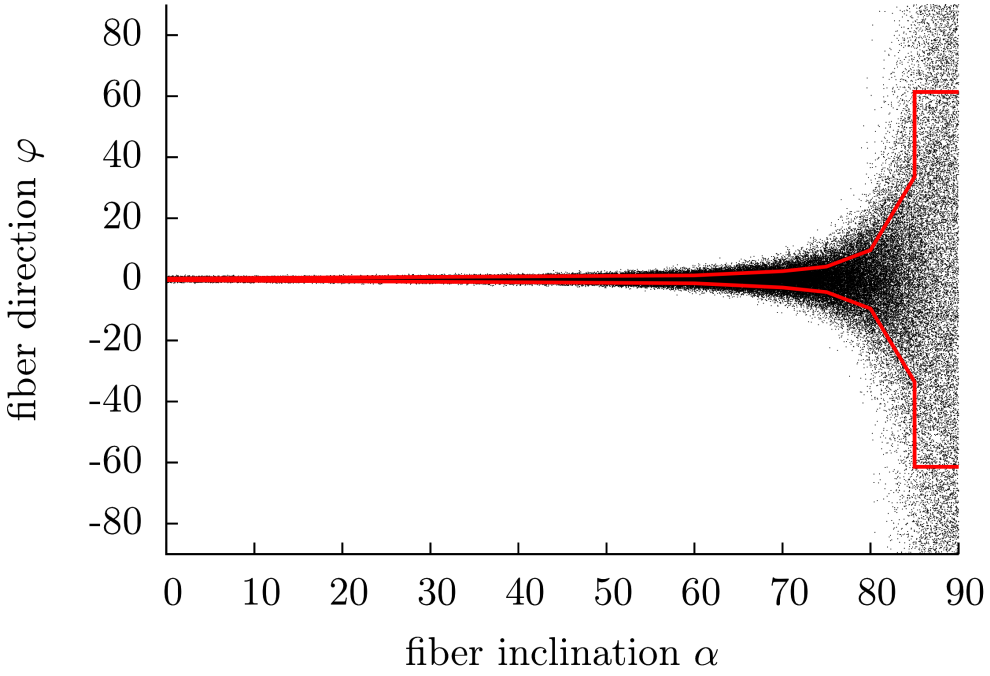

Figure 5.1: The observation likelihood of the in-plane fiber direction φ was approximated piecewise by normal distributions (for $|\alpha| \leq 85°$) and a uniform distribution (for $|\alpha| > 85°$) from simulations (see Fig. 3.9a). The red line represents standard deviations of the approximating normal distributions, and the 68.2-%-quantile in case of the uniform distribution.

over from Arulampalam et al. [2]. It relies on the estimated effective sample size N_{eff}, a measure for degeneration. If it falls below a fixed threshold N_T, all particles are resampled with a probability according to their current weight. This implies, that particles with a very low weight are probably replaced by duplicates of particles with a very high weight. The complete particle filter algorithm is given in Algorithm 1.

Algorithm 1 Particle filter

for $i \leftarrow 1$, N **do**
  $x_0^i \leftarrow y^0$ *//initialize particle* x_0^i
  $w_0^i \leftarrow N^{-1}$ *//initialize weight* w_0^i
end for
while fiber is not at end **do**
  $x_k^i \sim p(x_k^i | x_{k-1}^i)$ *//propagate particles by sampling from the prior distribution*
  $y_k \leftarrow$ fiber orientation at current position *//get measurement*
  $w_k^i \leftarrow w_{k-1}^i \cdot p(x_k^i | y_k)$ *//propagate weight*
  $w_k^i \leftarrow w_k^i / \sum_{i=1}^N w_k^i$ *//normalize weight*
  $N_{\text{eff}} \leftarrow \frac{1}{\sum_{i=1}^N (w_k^i)^2}$ *//approximate effective sample size*
  if $N_{\text{eff}} < N_T$ **then**
    RESAMPLE($\{x_k^i, w_k^i\}_{i=1}^N$) *//perform systematic resampling*
  end if
end while

5.3 Evaluation on Synthetic Data

The crossing and kissing fiber arrangements, which were simulated in Section 3.3, are used again here to evaluate tractography. 500 seed points were randomly placed inside the vector field (Fig. 5.2) and used as starting points for tractography. The tracts reconstructed by the particle filter were compared to those reconstructed by a streamline algorithm. Tracking was restricted to two dimensions in order to simplify the assessment of errors of the direction angle. As argued before, the inclination angle is biased by unknown fiber

Algorithm 2 Systematic resampling algorithm

$c_0 \leftarrow w_k^0$ *//construct cumulative distribution function (cdf)*
for $i \leftarrow 1, N$ **do**
  $c_i \leftarrow c_{i-1} + w_0^i$
end for
$i \leftarrow 1$
$u_0 \sim \mathcal{U}[0, N^{-1}]$ *//draw a sample from a uniform distribution*
for $j \leftarrow 1, N$ **do**
  $u_j \leftarrow u_0 + j \cdot (N^{-1})$
  while $u_j > c_i$ **do** *//keep particle i, if cdf at index i*
  //is higher than uniform probability
    $i \leftarrow i + 1$
  end while
  $x_k^j \leftarrow x_k^i$ *//replace particle j by particle i*
  $w_k^j \leftarrow N^{-1}$ *//set weight to N^{-1}*
end for

mixture and unknown myelination. The restriction to two dimensions also simplifies visualization. The streamline algorithm interpolates the fiber orientation at the current position of the vector field, ignoring the inclination angle, and steps forward in this direction. The particle filter determines direction and inclination angle at each position, but the steps are projected onto the two-dimensional plane. Streamline and particle tracking were performed with the same set of 500 seed points and the same step length ($0.3 \cdot 64\,\mu\text{m} \approx 20\,\mu\text{m}$). Particle filtering was performed with 100 particles and a threshold of the approximated effective sample size $N_T = \frac{2}{3}N = 67$. The standard deviation σ_φ of the prior density was varied between 2° and 0.2°. Accordingly, the maximum angular deviation $\Delta\varphi$ was varied between 5° and 20° for the streamline algorithm, which seems to comprise the most dynamic changes. For objective evaluation, four target areas (Fig. 5.3) at the endings of the fiber branches were defined, and the combinations of reached target areas were determined for each fiber. In this way, the number of fibers that crossed, bended and did not reach more than one target area were determined. The particle filter relies on random samples, which causes the resulting fiber tracts to vary slightly

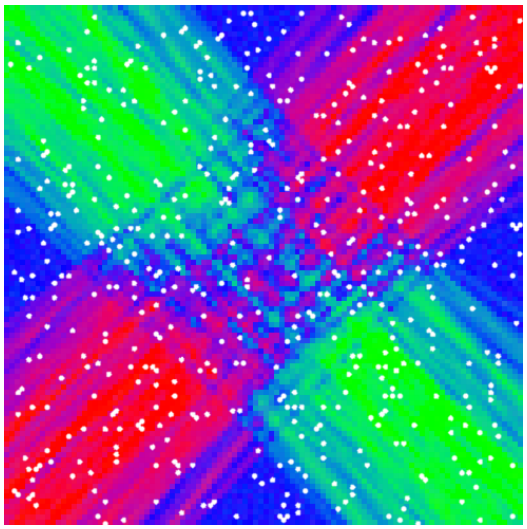

Figure 5.2: The 500 seed points that were used for tractography, are shown on the fiber orientation map of the crossed fiber arrangement (see Fig. 3.15a). The seed points were sampled from a uniform distribution. Local tractography algorithms such as streamline algorithms or particle filters need a starting point for each fiber to be tracked.

between repeated calls. Therefore, the number of crossed, bended and too short fibers was averaged over multiple repeated calls.

5.3.1 Results

In the crossing fiber arrangement, the fibers reconstructed by the particle filter algorithm generally appear less bended than the fibers reconstructed by the streamline algorithm (Fig. 5.4(a)-(b)). The streamline algorithm also created several degenerated fiber paths (Fig. 5.4c), i.e. fibers, that run into the center of the crossing and return to the same branch that they came from, or fibers that take a zig-zag path through the crossing. With decreasing standard deviation σ_φ for the particle filter and decreasing maximum $\Delta\varphi$ for the streamline algorithm, less fibers bended inconsistently to the neighboring target regions (Fig. 5.5). However, streamline tracking always created more bended fibers than crossing ones. Particle tracking yielded more crossing than bending fibers for $\sigma_\varphi < 1°$. The results in Fig. 5.4 are shown for $\sigma_\varphi = 1°$ and

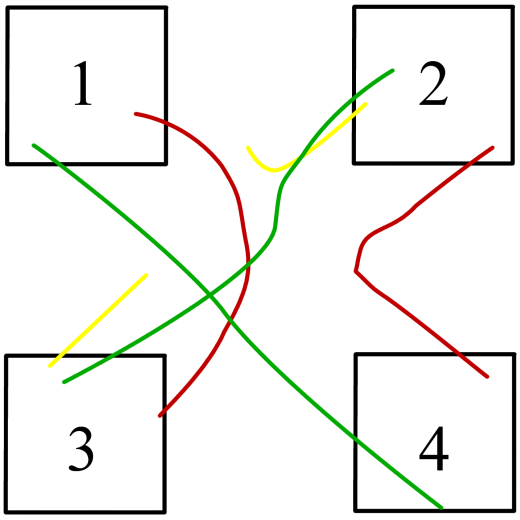

Figure 5.3: The target areas are used to evaluate the course of the tracked fibers. If two diagonal target areas are reached, the fibers are assumed to cross (green). If two neighboring target areas are reached, then the fibers are assumed to bend (red). If less than one target area is reached, the fiber is assumed to end too early (yellow).

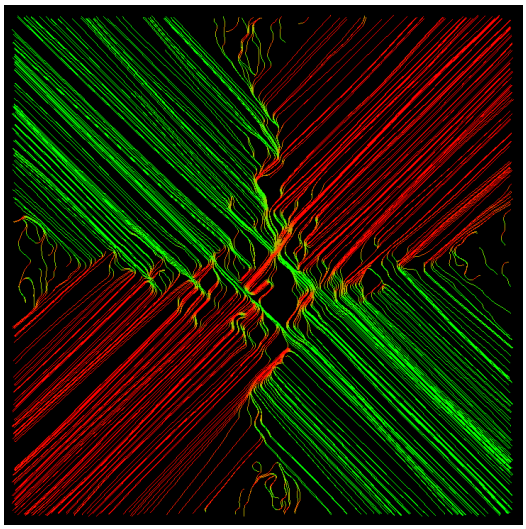

(a) Streamline with maximum $\Delta\varphi = 10°$

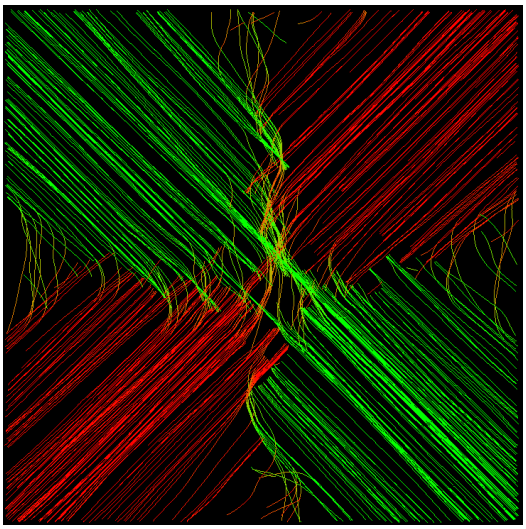

(b) Particle filter with $\sigma_\varphi = 1°$

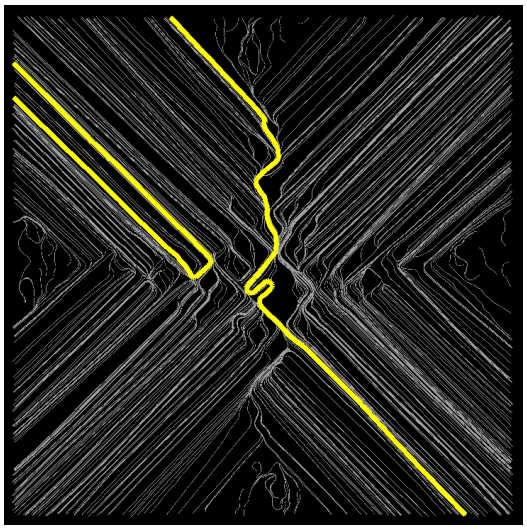

(c) Degenerated streamline

Figure 5.4: The fiber tracts of a synthetic fiber crossing arrangement appear less bended, when reconstructed by a particle filter, compared to the reconstruction with a streamline tractography algorithm. The streamline tractography algorithm creates several degenerated fiber tracts, that strongly diverge from the true fibers, two of them are highlighted.

$\Delta\varphi = 10°$. These parameters give a good trade-off between bended, too short and crossed fibers for each case.

In the kissing fiber arrangement, the results of streamline tractography and particle filter appear very similar (Fig. 5.6). The results are shown for $\sigma_\varphi = 1°$ and $\Delta\varphi = 10°$ as before. The evaluation of reached target regions on the synthetic kissing fiber arrangement does not show large differences, neither between both tracking approaches, nor between different values of σ_φ or maximum $\Delta\varphi$ (Fig. 5.7). Particle tracking with $\sigma_\varphi = 1°$ reconstructed 5% less bending fibers, than streamline tractography.

5.3.2 Discussion

In the crossing fiber arrangement, a considerable reduction of bended and therefore incorrect fibers was achieved by tractography with a particle filter. The additional specifications of a fiber model improved the trade-off between correctly crossing fibers, incorrectly bending fibers and too short fibers. A good choice seems to be $\sigma_\varphi = 1°$. In the kissing fiber arrangement, streamline tractography and particle filter tractography perform very similar. The streamline tractography achieves slightly more correctly bending fibers compared to the particle filter tractography. The choice of $\sigma_\varphi = 1°$ is also suitable for the kissing fiber arrangement.

As noted before, the prior density is a heuristic choice, commonly utilized to ensure smoothness of the reconstructed fiber tracts. In the course of real fibers, the distribution of fiber orientation changes is difficult to assess. A fiber was tracked manually on a histologic section to find a plausible fiber model (Fig. 5.8). The histologic section was imaged with a polarizing microscope, with an in-plane resolution of $1.6\,\mu$m. At this scale, the fiber architecture becomes visible in the image contrast. The manually tracked fiber was interpolated by line segments of a constant step length ($30\,\mu$m). The sequence of direction changes was analyzed in the manually tracked fiber. The histogram of direction changes does not display a normal distribution (Fig. 5.9), which was also tested and rejected by a Shapiro Wilk test. In addition, the sequence of direction changes is highly autocorrelated (Fig. 5.10). Probably, this example fiber is not representative for all fibers in the human

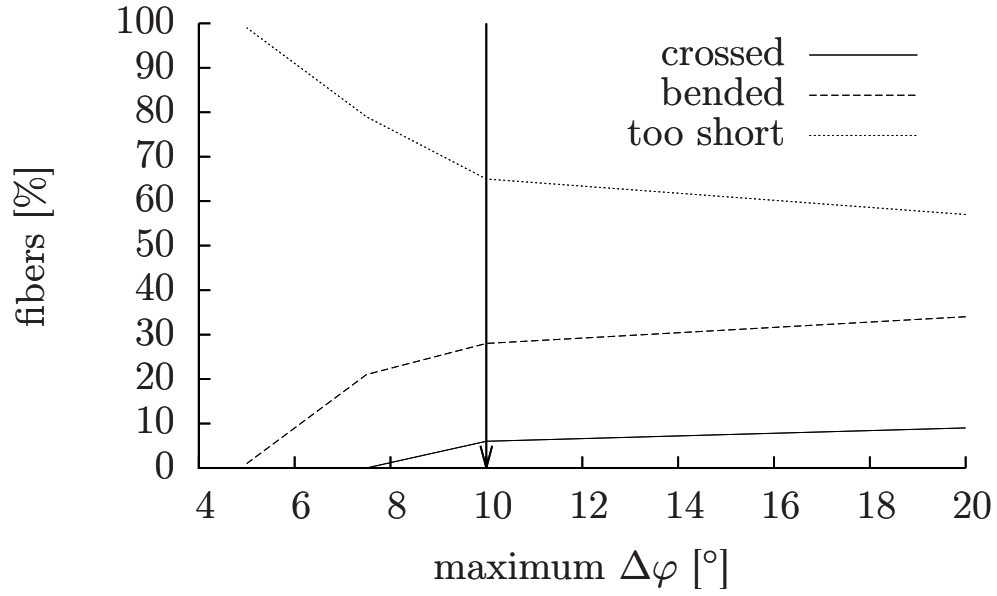

(a) Streamline

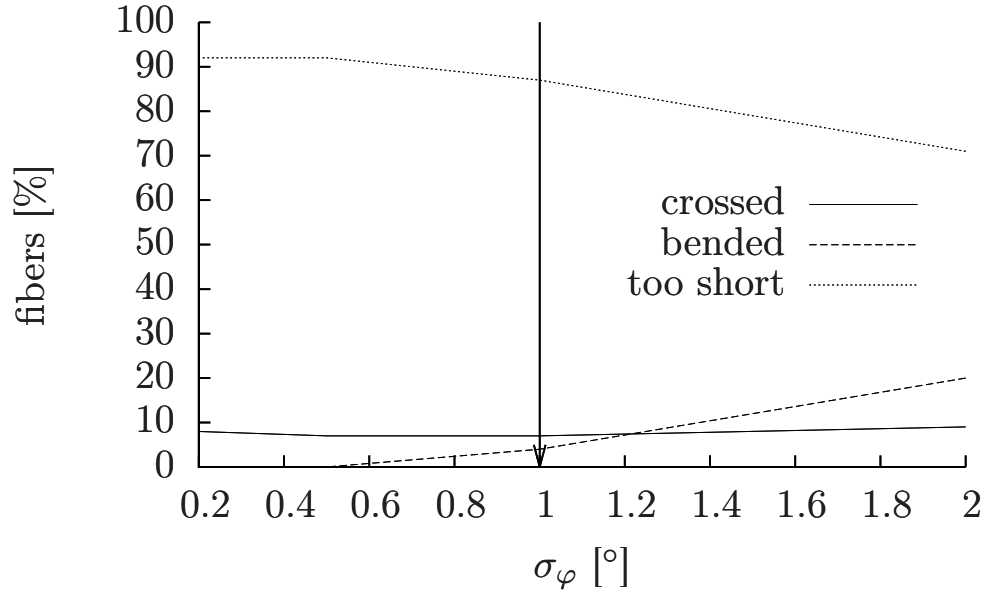

(b) Particle filter

Figure 5.5: The results of tractography were evaluated by counting the reached target regions. In the crossing fiber arrangement, the reconstructed fibers should rather cross than bend. This is achieved with a particle filter with $\sigma_\varphi < 1°$, but not by the streamline algorithm. The results for $\sigma_\varphi = 1°$ and $\Delta\varphi = 10°$ are shown in Fig. 5.4.

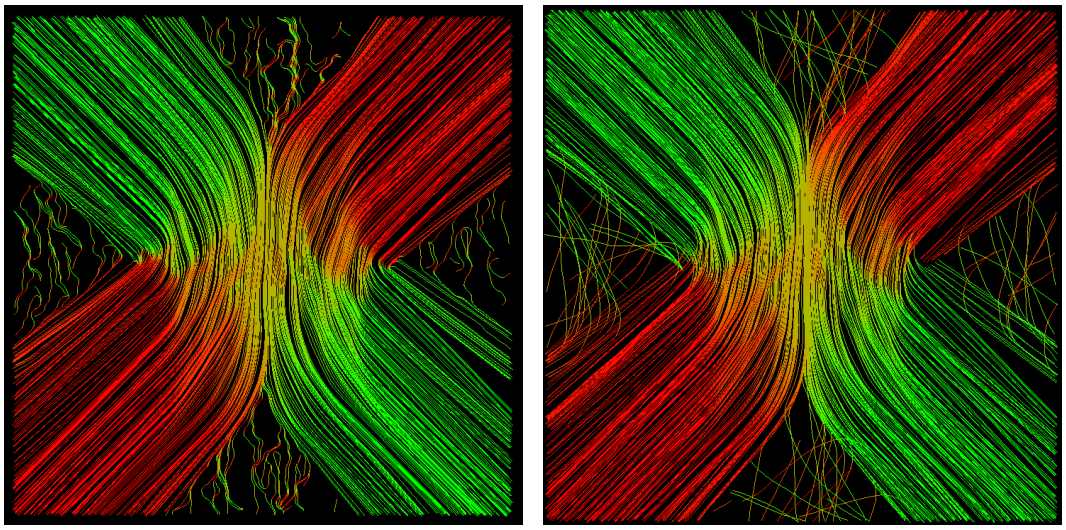

(a) Streamline with maximum $\Delta\varphi = 10°$ (b) Particle filter with $\sigma_\varphi = 1°$

Figure 5.6: The fiber tracts of a synthetic fiber kissing arrangement appear very similar, when reconstructed by a particle filter, and by streamline tractography.

brain, but it shows, that the heuristic choice of the fiber model cannot be validated easily and should be reconsidered.

The synthetic fiber crossing consists of 450 crossing fibers. Both tracking algorithms only reconstruct a small set of fibers that completely cross to the opposite side. As shown in Chapter 3, multiple fiber orientations interfere with each other. Fiber orientations, that compose the minority of the mixed fiber orientations are occluded by other fiber orientations and are therefore lost. This problem increases with decreasing resolution in z-direction, i.e. with increasing section thickness.

The streamline algorithm can be parametrized by a maximum $\Delta\varphi$ as a stop criterion. A very strict stop criterion can prevent sharp turns, which arise when the tracking algorithm leaves a fiber tract and accidentally jumps to a different one. However, this does not allow to continue fiber tracts through regions with increased measurement uncertainty. In this point, the particle filter is clearly superior to the streamline tracking algorithm.

Although tractography algorithms can overcome random errors in the

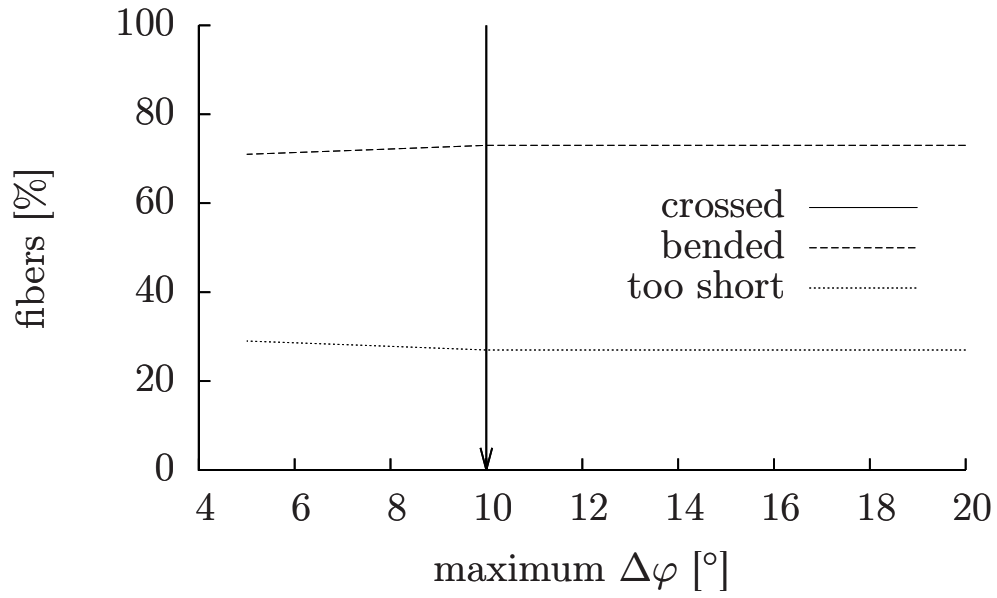

(a) Streamline

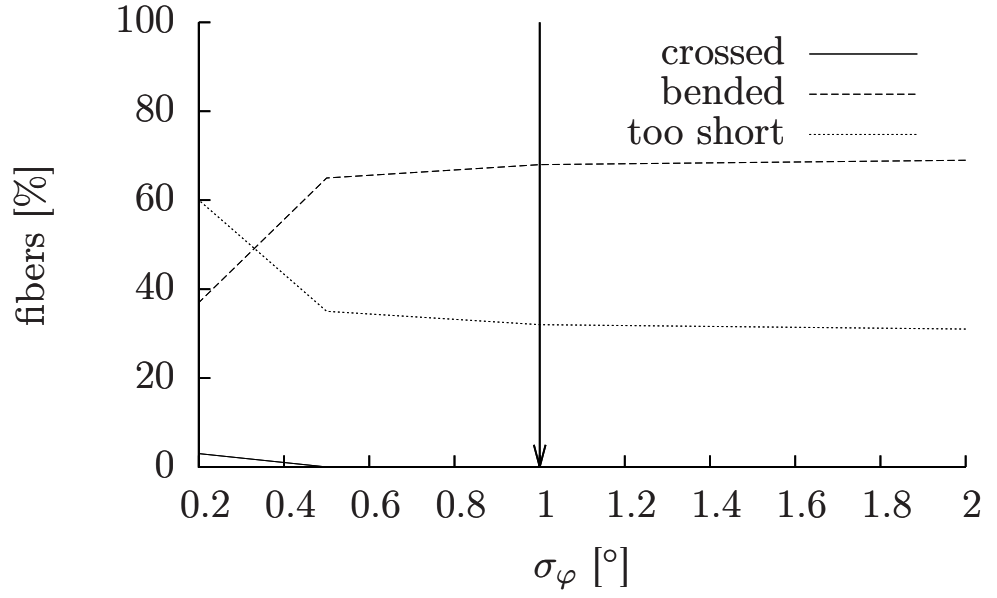

(b) Particle filter

Figure 5.7: The results of tractography were evaluated by recording the reached target regions. In the kissing fiber arrangement, the reconstructed fibers should bend to a neighboring target region. Both tracking approaches created less than 1% crossing fibers. The particle filter created slightly more fibers, that ended too early and did not reach a second target region. The results for $\sigma_\varphi = 1°$ and $\Delta\varphi = 10°$ are shown in Fig. 5.6.

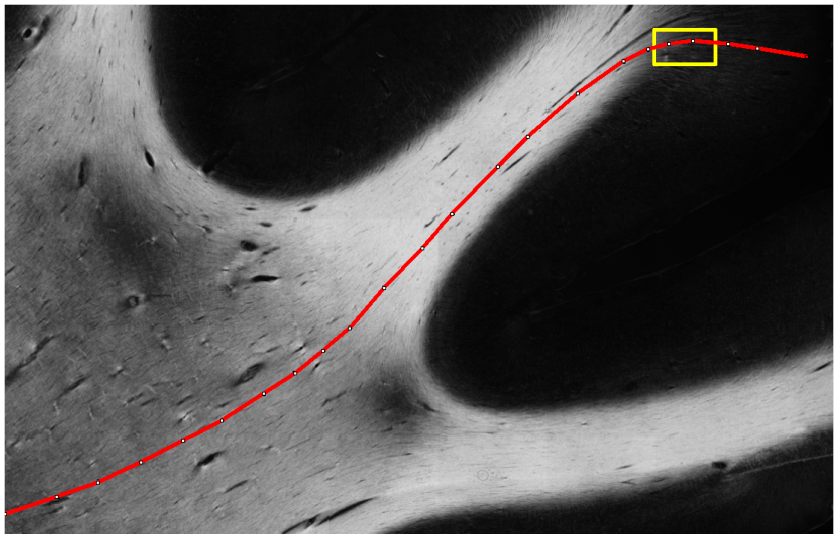

(a) Manually tracked fiber

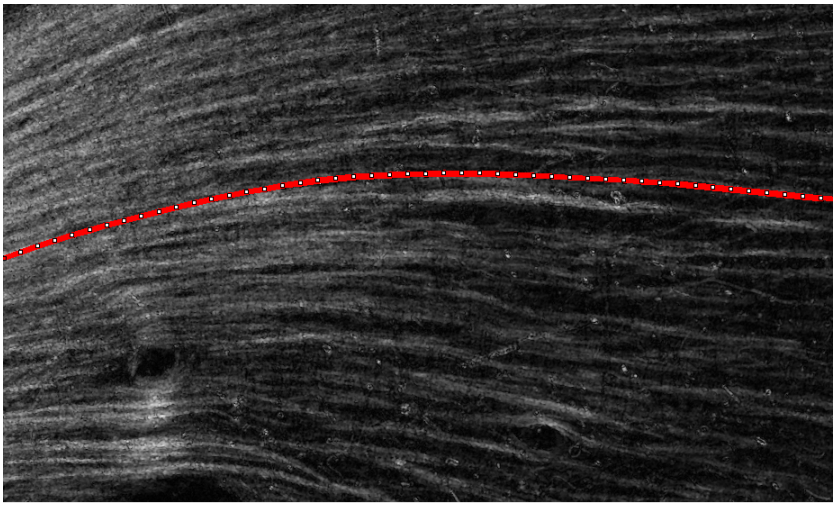

(b) 1 step = 30 μm

Figure 5.8: (a) An image was acquired with a polarizing microscope and a fiber course was defined by manual placed points and an interpolating spline curve. (b) This is a magnification of the yellow box in (a). The manually placed curve was approximated by linear segments with a fixed step length (20 px $\approx$ 30 μm). The sequence of fiber direction changes $\Delta\varphi_k$ was analyzed to validate a linear fiber propagation model with normal distribution.

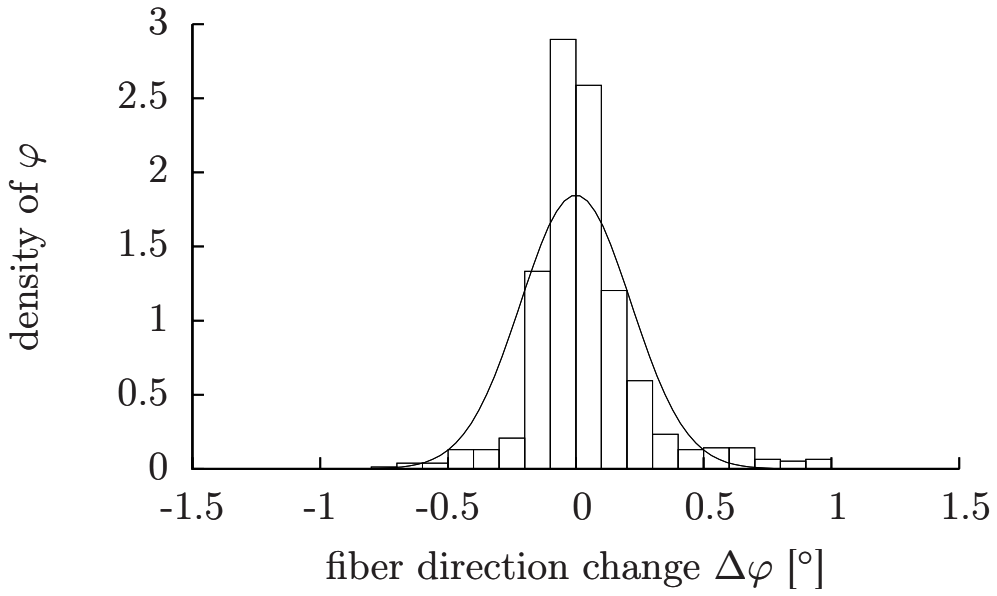

Figure 5.9: The histogram of fiber direction changes is symmetric with a single peak, but it is not normally distributed. This was also rejected by a Shapiro Wilk test for normality.

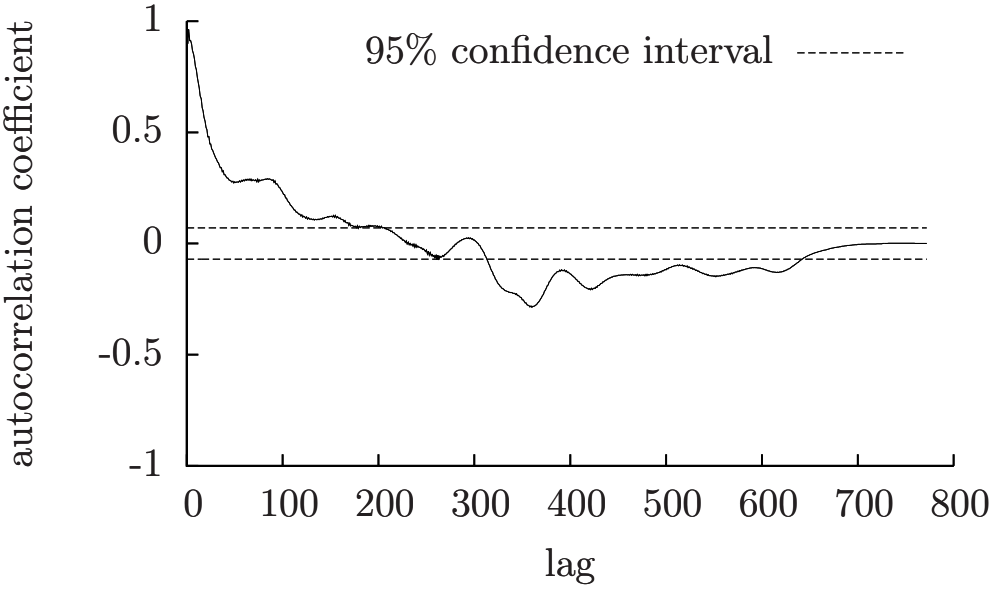

Figure 5.10: The autocorrelation plot displays significant autocorrelation of the fiber direction change for lags up to 206 and between 313 and 642. This suggests, that a linear model is not sufficient to model fiber propagation.

vector field, systematic errors of the inclination sign cannot be solved thereby. Systematic errors must be minimized beforehand. Additional measurements of the fiber mixture and the specific tissue birefringence would be needed for this, and these corrections are critical for three-dimensional tracking on PLI data in the future.

The evaluation presented here is limited. The synthetic data set, although simulated with many details, may not reflect all measurement errors correctly. For better evaluation, a phantom is needed, or a tissue sample with a well known fiber architecture. The presented particle filter algorithm as well as the evaluation was restricted to two dimensions and therefore does not allow any conclusions about a suitable measurement model for the inclination angle. The fiber model, if it is found justifiable for the in-plane direction angle, can be of course transferred to the out-of-plane inclination angle, because the course of a fiber does not depend on the sectioning plane. Another open issue for three-dimensional tractography based on PLI data are potential errors in the vector field by insufficient registration. The sectioning process applies strong deformations or even damage to the brain tissue, which cannot be completely compensated by image registration. The errors, that arise thereby have not been analyzed here.

The advantages and disadvantages of particle filter tractography compared to streamline tractography based on DW-MRI are generally the same when transferred to PLI data. The resulting fiber tracts are associated with a degree of certainty and tracts with high uncertainty are not continued. This prevents or at least reduces the detection of incorrect fiber tracts. Furthermore, the particle filter is able to track multiple deviating fiber tracts simultaneously. In the current implementation, the most probable fiber tract is selected when a stop criterion is met, but the intermediate particle states allow the derivation of a connectivity matrix, which describes the probability of a connection between any seed point and any voxel. The computational demand of particle filter tractography compared to streamline tractography is noticeable. The computation time was increased by factor 83. If this increase is acceptable, this raises the question, whether the expected further increase in computation time needed for global tractography would also be acceptable. This should be explored in future studies.

Clearly, the presented tractography algorithm based on particle filtering, is not able to handle all problems that arise with 3D-PLI data. The reconstructed fiber tracts often do not correspond to the true fiber tracts. However, the improvement in comparison to streamline tractography is visible. Especially seriously degenerated tracts are avoided by use of the particle filter. Considering the wide range of algorithmic ideas for fiber tracking on DW-MRI data, there is quite a chance, that another tractography approach could achieve further improvements.

Chapter 6

Conclusions and Outlook

Until now, PLI tractography was restricted to streamline methods without awareness of the reliability of the reconstructed fiber tracts. In this work, sources of errors and uncertainties were systematically investigated by simulation of typical fiber arrangements. The simulation demonstrated the influence of fiber mixture on the out-of-plane fiber inclination, which cannot be handled without further sources of information. It demonstrated the influence of inhomogeneous myelination on very steep and very flat inclination angles. It was shown that the reliability of the in-plane fiber direction angle is influenced by the signal amplitude, i.e. the measured inclination angle.

For the first time, the derivation of the inclination sign from tilted measurements has been evaluated. On real data, this derivation does not seem to be robust for all pixels. The tilting process was simulated on a synthetic data set in order to identify potential sources of errors. A Markov random field approach improved the derivation of the correct sign by including prior knowledge about spatial continuity and the relation between in-plane and out-of-plane angles. The approach for determining the inclination sign was the first one to combine measurements and coherence constraints, while both of these approaches have been pursued separately before. An alternative smoothness weighting was evaluated, but it did not yield better results. Other smoothness weighting functions or optimization schemes could be examined in the future.

The influence of the inclination angle on the direction angle, which was

shown by simulation, was used to improve tractography. Direction angles that were found with high inclination angles were considered as uncertain and were complemented by prior knowledge about fiber continuity. The implementation of a particle filter propagating uncertainty during tractography clearly improved the results in a crossing fiber arrangement. Besides the particle filter, many alternatives for tractography exist. The particle filter is an advantageous choice, because it is able to propagate uncertainty without restrictions to normal distributions. However, other probabilistic algorithms may need less resources and should be evaluated as alternatives. Especially interesting is the applicability of global tractography algorithms to large 3D-PLI data sets.

The accurate and reliable determination of the out-of-plane fiber inclination seems to be the most critical aspect in 3D-PLI at the moment. Several ideas exist to approach this issue. The transmittance modality contains information about the myelination of the examined tissue. The inclusion of the transmittance value in the calculation of the inclination angle could correct the resulting inclination angle considerably.

Another source of error in the inclination angle is the unknown degree of fiber mixture. By using the more general Müller Stokes formalism for polarimetry instead of the Jones calculus [45], more information about the tissue sample could be inferred. The Stokes parameters are known to contain information about parallelism in a birefringent sample. This could provide the needed information to distinguish steep fibers from mixed fibers, which both possess low retardation values.

Extended measurements of tilted specimen could also supply additional information about the absolute inclination angle. A higher tilting amplitude could yield observable changes in the in-plane fiber direction and provide an independent source of estimation of the inclination angle. However, the tilting amplitude is limited by the degree of interpolation that is needed when transforming the tilted image onto the flat position. By increasing the number of tilting directions, the derivation of the inclination sign could become more robust. Slight inaccuracies in the back-projection could also cause problems with the derivation of the inclination sign. This effect must be evaluated more closely in order to justify the use of smoothing in favor of measured data at

critical pixels. The second most critical issue in PLI is section registration. This problem was not analyzed in the scope of this work, but it is obvious that misregistered brain sections will introduce significant errors to the results of tractography. The study of registration errors will become more important, as soon as the inclination angle becomes more accurate. Tractography over long distances, across multiple sections, is not reasonable until then.

Until now, PLI tractography has been limited to small data sets of a few millimeters or a few megabyte. When the regions of interest are expanded and the measurements are carried out on the high resolving polarizing microscope, the availability of high performance computing is crucial. This affects data storage, data access and computation time. Typical data sets easily exceed the main memory of a standard PC. Further developments of PLI tractography must consider data management as an essential challenge. Whether an algorithm can stay below reasonable time limits or not will depend on whether it can be parallelized. So far, this is an aspect that has not received much attention in the DW-MRI community, but it must be approached in PLI now.

This work exclusively investigated white matter. In gray matter, the myelination is substantially lower, which strongly influences the determination of the inclination angle. Especially, the transition region of white to gray matter, where the myelination gradually changes, poses new challenges to the determination of the correct reference value r_{ref}.

The advantages of 3D-PLI for mapping the connectome is the intermediate scale between DW-MRI and electron microscopy, and the availability of a three-dimensional fiber orientation. Especially in gray matter, where DW-MRI is not able to resolve fiber orientations reliably, 3D-PLI can provide unique information. 3D-PLI also has the potential to support the interpretation of DW-MRI measurements. Due to the reasons mentioned above, 3D-PLI is not able to serve as a gold standard for DW-MRI, yet. However, both modalities can benefit from a comprehensive comparison of common tissue samples.

The present work shows an important analysis of the reliability and accuracy of the fiber orientation determined by 3D-PLI and considerably improved the PLI inclination sign ambiguity and the quality of reconstructed fiber tracts. This is the basis for the further development of PLI tractography, which aims for the reliable reconstruction of fiber tracts in the human brain.

Appendix

Derivation of the Data Energy

The absolute difference between oppositely tilted inclination angles can be expressed as

$$
\begin{aligned}
& \alpha^{\psi\pm180^\circ} - \alpha^{\psi} \\
= \;& 2 \cdot \tfrac{\alpha^{\psi\pm180^\circ} - \alpha^{\psi}}{2} && / \;\; |\tfrac{\alpha^{\psi\pm180^\circ} - \alpha^{\psi}}{2}| \leq |\tau| \\
& && \text{for small } |\tau| : \\
& && \tau \approx \sin(\tau) \\
\approx \;& 2 \cdot \sin\left(\tfrac{\alpha^{\psi\pm180^\circ} - \alpha^{\psi}}{2}\right) && / \;\; \cos(\alpha) \neq 0 \\
= \;& \tfrac{2}{\cos(\alpha)} \cdot \sin\left(\tfrac{\alpha^{\psi\pm180^\circ} - \alpha^{\psi}}{2}\right) \cdot \cos(\alpha) && / \;\; \alpha^{\psi\pm180^\circ} - \alpha = \alpha - \alpha^{\psi} \\
& && \text{(changes in opposite} \\
& && \text{tilts are symmetric)} \\
= \;& \tfrac{2}{\cos(\alpha)} \cdot \sin\left(\tfrac{\alpha^{\psi\pm180^\circ} - \alpha^{\psi}}{2}\right) \cdot \cos(\tfrac{\alpha^{\psi\pm180^\circ} + \alpha^{\psi}}{2}) && / \;\; \sin x - \sin y = \\
& && 2 \cdot \sin\left(\tfrac{x-y}{2}\right) \cdot \cos\left(\tfrac{x+y}{2}\right) \\
& && \text{(addition theorem)} \\
= \;& \tfrac{1}{\cos(\alpha)} \cdot [\sin(\alpha^{\psi\pm180^\circ}) - \sin(\alpha^{\psi})] && / \;\; \alpha^{\psi} = \arcsin(\\
& && \sin(\tau)\cos(\alpha)\cos(\varphi - \psi) + \\
& && \cos(\tau)\sin(\alpha)) \\
= \;& \tfrac{1}{\cos(\alpha)} \cdot [\sin(\tau)\cos(\alpha)\cos(\varphi - \psi \mp 180^\circ) + \cos(\tau)\sin(\alpha) - \\
& \sin(\tau)\cos(\alpha)\cos(\varphi - \psi) - \cos(\tau)\sin(\alpha)] \\
= \;& \tfrac{1}{\cos(\alpha)} \cdot [-2 \cdot \sin(\tau) \cdot \cos(\alpha) \cdot \cos(\varphi - \psi)] \\
= \;& -2 \cdot \sin(\tau) \cdot \cos(\varphi - \psi)
\end{aligned}
$$

Bibliography

[1] I. Aganj, C. Lenglet, N. Jahanshad, E. Yacoub, N. Harel, P. M. Thompson, and G. Sapiro. A Hough transform global probabilistic approach to multiple-subject diffusion MRI tractography. *Medical Image Analysis*, 15(4):414–425, August 2011.

[2] M. S. Arulampalam, S. Maskell, N. Gordon, and T. Clapp. A tutorial on particle filters for online nonlinear/non-gaussian Bayesian tracking. *IEEE Transactions On Signal Processing*, 50(2):174–188, February 2002.

[3] Y. Assaf and P. J. Basser. Composite hindered and restricted model of diffusion (CHARMED) MR imaging of the human brain. *NeuroImage*, 27(1):48–58, August 2005.

[4] H.-E. Assemlal, D. Tschumperle, L. Brun, and K. Siddiqi. Recent advances in diffusion MRI modeling: Angular and radial reconstruction. *Medical Image Analysis*, 15(4):369–396, August 2011.

[5] H. Axer, M. Axer, T. Krings, and D. Graf von Keyserlingk. Quantitative estimation of 3-D fiber course in gross histological sections of the human brain using polarized light. *Journal of Neuroscience Methods*, 105(2):121–131, February 2001.

[6] M. Axer, K. Amunts, D. Gräßel, C. Palm, J. Dammers, H. Axer, U. Pietrzyk, and K. Zilles. A novel approach to the human connectome: Ultra-high resolution mapping of fiber tracts in the brain. *NeuroImage*, 54(2):1091–1101, January 2011.

[7] M. Axer, D. Gräßel, M. Kleiner, J. Dammers, T. Dickscheid, J. Reckfort, T. Hütz, B. Eiben, U. Pietrzyk, K. Zilles, and K. Amunts. High-

resolution fiber tract reconstruction in the human brain by means of three-dimensional polarized light imaging (3D-PLI). *Frontiers in Neuroinformatics*, 5(34):1–13, December 2011.

[8] R. Bammer, B. Acar, and M. E. Moseley. In vivo MR tractography using diffusion imaging. *European Journal of Radiology*, 45(3):223 – 234, 2003.

[9] P. J. Basser and D. K. Jones. Diffusion-tensor MRI: theory, experimental design and data analysis - a technical review. *NMR in Biomedicine*, 15(7-8):456–467, November 2002.

[10] P. J. Basser, J. Mattiello, and D. Le Bihan. Estimation of the effective self-diffusion tensor from the NMR spin echo. *Journal of Magnetic Resonance. Series B*, 103(3):247–254, March 1994.

[11] P. J. Basser, S. Pajevic, C. Pierpaoli, J. Duda, and A. Aldroubi. In vivo fiber tractography using DT-MRI data. *Magnetic Resonance in Medicine*, 44(4):625–632, October 2000.

[12] C. Beaulieu. The basis of anisotropic water diffusion in the nervous system - a technical review. *NMR in Biomedicine*, 15(7-8):435–455, 2002.

[13] T. E. Behrens, H. Johansen-Berg, M. W. Woolrich, S. M. Smith, C. A. Wheeler-Kingshott, P. A. Boulby, G. J. Barker, E. L. Sillery, K. Sheehan, O. Ciccarelli, A. J. Thompson, J. M. Brady, and P. M. Matthews. Non-invasive mapping of connections between human thalamus and cortex using diffusion imaging. *Nature Neuroscience*, 6(7):750–757, July 2003.

[14] T. E. J. Behrens, H. Johansen-Berg, S. Jbabdi, M. F. S. Rushworth, and M. W. Woolrich. Probabilistic diffusion tractography with multiple fibre orientations: What can we gain? *NeuroImage*, 34(1):144–155, January 2007.

[15] T. E. J. Behrens and O. Sporns. Human connectomics. *Current Opinion in Neurobiology*, 22(1):144–153, February 2012.

[16] H. Benveniste and S. Blackband. MR microscopy and high resolution small animal MRI: applications in neuroscience research. *Progress in Neurobiology*, 67(5):393–420, August 2002.

[17] J. I. Berman, S. Chung, P. Mukherjee, C. P. Hess, E. T. Han, and R. G. Henry. Probabilistic streamline q-ball tractography using the residual bootstrap. *NeuroImage*, 39(1):215–222, August 2008.

[18] J. Bioucas-Dias and G. Valadao. Phase unwrapping via diversity and graph cuts. In *15th International Conference on Systems, Signals and Image Processing*, Bratislava, Slovak Republic, June 2008.

[19] M. Björnemo, A. Brun, R. Kikinis, and C.-F. Westin. Regularized stochastic white matter tractography using diffusion tensor MRI. In T. Dohi and R. Kikinis, editors, *Medical Image Computing and Computer Assisted Intervention (MICCAI)*, volume 2488 of *Lecture Notes in Computer Science*, pages 435–442. Springer, September 2002.

[20] E. Boros, P. L. Hammer, and X. Sun. Network flows and minimization of quadratic pseudo-boolean functions. Technical Report RRR 17-1991, Rutgers Center for Operations Research (RUTCOR), Piscataway, NJ, USA, May 1991.

[21] Y. Boykov and V. Kolmogorov. An experimental comparison of min-cut/max-flow algorithms for energy minimization in vision. *IEEE Transactions on Pattern Analysis and Machine Intelligence*, 26(9):1124–1137, 2004.

[22] Y. Boykov, O. Veksler, and R. Zabih. Fast approximate energy minimization via graph cuts. *IEEE Transactions on Pattern Analysis and Machine Intelligence*, 23(11):1222–1239, 2001.

[23] Y. Y. Boykov and M. P. Jolly. Interactive graph cuts for optimal boundary & region segmentation of objects in N-D images. In *IEEE International Conference On Computer Vision (ICCV)*, Vancouver, Canada, July 2001.

[24] M. D. Budde and J. A. Frank. Examining brain microstructure using structure tensor analysis of histological sections. *NeuroImage*, 63(1):1–10, October 2012.

[25] U. Bürgel, K. Amunts, L. Hoemke, H. Mohlberg, J. M. Gilsbach, and K. Zilles. White matter fiber tracts of the human brain: Three-dimensional mapping at microscopic resolution, topography and intersubject variability. *NeuroImage*, 29(4):1092–1105, February 2006.

[26] B. de Campos Vidal, M. L. Silviera Mello, A. C. Caseiro-Filho, and C. Godo. Anisotropic properties of the myelin sheath. *Acta Histochemica*, 66:32–39, 1980.

[27] S. Y. Chen, H. Tong, and C. Cattani. Markov models for image labeling. *Mathematical Problems in Engineering*, (814356):1–18, 2012.

[28] Y. Cointepas, C. Poupon, D. Le Bihan, and J.-F. Mangin. A spin glass based framework to untangle fiber crossing in MR diffusion based tracking. In T. Dohi and R. Kikinis, editors, *Medical Image Computing and Computer Assisted Intervention (MICCAI)*, volume 2488 of *Lecture Notes in Computer Science*, pages 475–482. Springer, 2002.

[29] T. E. Conturo, N. F. Lori, T. S. Cull, E. Akbudak, A. Z. Snyder, J. S. Shimony, R. C. McKinstry, H. Burton, and M. E. Raichle. Tracking neuronal fiber pathways in the living human brain. *Proceedings of the National Academy of Sciences of the United States of America*, 96(18):10422–10427, August 1999.

[30] J. Dauguet, T. Delzescaux, F. Cond, J.-F. Mangin, N. Ayache, P. Hantraye, and V. Frouin. Three-dimensional reconstruction of stained histological slices and 3D non-linear registration with in-vivo MRI for whole baboon brain. *Journal of Neuroscience Methods*, 164(1):191–204, 2007.

[31] J. Dauguet, S. Peled, V. Berezovskii, T. Delzescaux, S. K. Warfield, R. Born, and C.-F. Westin. Comparison of fiber tracts derived from

in-vivo DTI tractography with 3D histological neural tract tracer reconstruction on a macaque brain. *NeuroImage*, 37(2):530–538, August 2007.

[32] G. Demoment. Image reconstruction and restoration: overview of common estimation structures and problems. *IEEE Transactions on Acoustics, Speech and Signal Processing*, 37(12):2024 –2036, December 1989.

[33] M. Descoteaux, R. Deriche, T. R. Knosche, and A. Anwander. Deterministic and probabilistic tractography based on complex fibre orientation distributions. *IEEE Transactions on Medical Imaging*, 28(2):269–286, 2009.

[34] A. Doucet, N. de Freitas, and N. Gordon, editors. *Sequential Monte Carlo Methods in Practice*. Springer, 2001.

[35] D. G. Duru and M. Oezkan. Fiber tracking: A recursive stack algorithmic approach. In *International Conference of the IEEE Engineering in Medicine and Biology Society (IEMBS)*, Lyon, France, August 2007.

[36] D. C. van Essen and K. Ugurbil. The future of the human connectome. *NeuroImage*, 62(2):1299–1310, August 2012.

[37] Y. Feng and Z. Wang. Ant colony optimization for global white matter fiber tracking. In Y. Tan, Y. Shi, Y. Chai, and G. Wang, editors, *Advances in Swarm Intelligence*, volume 6728 of *Lecture Notes in Computer Science*, pages 267–276. Springer, 2011.

[38] M. Feuerstein, H. Heibel, J. Gardiazabal, N. Navab, and M. Groher. Reconstruction of 3-D histology images by simultaneous deformable registration. In G. Fichtinger, A. Martel, and T. Peters, editors, *Medical Image Computing and Computer Assisted Intervention (MICCAI)*, volume 6892 of *Lecture Notes in Computer Science*, pages 582–589, Toronto, Canada, September 2011. Springer.

[39] P. Fillard, M. Descoteaux, A. Goh, S. Gouttard, B. Jeurissen, J. Malcolm, A. Ramirez-Manzanares, M. Reisert, K. Sakaie, F. Tensaouti,

T. Yo, J.-F. Mangin, and C. Poupon. Quantitative evaluation of 10 tractography algorithms on a realistic diffusion MR phantom. *NeuroImage*, 56(1):220–234, May 2011.

[40] P. Fillard, C. Poupon, and J.-F. Mangin. A novel global tractography algorithm based on an adaptive spin glass model. In G.-Z. Yang, D. Hawkes, D. Rueckert, A. Noble, and C. Taylor, editors, *Medical Image Computing and Computer-Assisted Intervention (MICCAI)*, volume 5761 of *Lecture Notes in Computer Science*, pages 927–934, London, UK, September 2009. Springer.

[41] M. A. Fischler and R. C. Bolles. Random sample consensus: a paradigm for model fitting with applications to image analysis and automated cartography. *Communications of the ACM*, 24(6):381–395, June 1981.

[42] O. Friman, G. Farneback, and C.-F. Westin. A Bayesian approach for stochastic white matter tractography. *IEEE Transactions on Medical Imaging*, 25(8):965–978, 2006.

[43] S. V. Gangnus, S. J. Matcher, and I. V. Meglinski. Monte Carlo modeling of polarized light propagation in biological tissues. *Laser Physics*, 14(6):886–891, June 2004.

[44] S. Geman and D. Geman. Stochastic relaxation, gibbs distributions, and the Bayesian restoration of images. *IEEE Transactions on Pattern Analysis and Machine Intelligence*, 6(6):721–741, 1984.

[45] N. Ghosh and I. A. Vitkin. Tissue polarimetry: concepts, challenges, applications, and outlook. *Journal of Biomedical Optics*, 16(11):110801-1–110801-29, November 2011.

[46] C. Gössl, L. Fahrmeir, B. Putz, L. M. Auer, and D. P. Auer. Fiber tracking from DTI using linear state space models: Detectability of the pyramidal tract. *NeuroImage*, 16(2):378–388, June 2002.

[47] G. F. Göthlin. Die doppelbrechenden Eigenschaften des Nervengewebes. *Kungliga Svenska Vetenskapsakademiens Handlingar*, 51(1):1–92, 1913.

[48] M. Grabe. *Measurement Uncertainties in Science and Technology*. Springer, 2005.

[49] R. W. Guillery, C. A. Mason, and J. S. Taylor. Developmental determinants at the mammalian optic chiasm. *The Journal of Neuroscience*, 15(7):4727–4737, July 1995.

[50] W. Guo, Q. Zeng, Y. Chen, and Y. Liu. Using multiple tensor deflection to reconstruct white matter fiber traces with branching. In *IEEE International Symposium on Biomedical Imaging: Macro to Nano*, Arlington, VA, USA, April 2006.

[51] P. Hagmann, L. Cammoun, X. Gigandet, S. Gerhard, P. E. Grant, V. Wedeen, R. Meuli, J.-P. Thiran, C. J. Honey, and O. Sporns. MR connectomics: Principles and challenges. *Journal of Neuroscience Methods*, 194(1):34–45, December 2010.

[52] P. Hagmann, L. Jonasson, P. Maeder, J.-P. Thiran, V. J. Wedeen, and R. Meuli. Understanding diffusion MR imaging techniques: From scalar diffusion-weighted imaging to diffusion tensor imaging and beyond. *Radiographics*, 26(suppl 1):S205–S223, October 2006.

[53] P. L. Hammer, P. Hansen, and B. Simeone. Roof duality, complementation and persistency in quadratic 0-1 optimization. *Mathematical Programming*, 28(2):121–155, 1984.

[54] J. M. Hammersley and P. Clifford. Markov field on finite graphs and lattices. unpublished manuscript, 1971.

[55] W. Hanke, R. Römer, and G. Dehnhardt. Visual fields and eye movements in a harbor seal (phoca vitulina). *Vision Research*, 46(17):2804–2814, September 2006.

[56] P. Hansen and D. O'Leary. The use of the L-curve in the regularization of discrete ill-posed problems. *SIAM Journal on Scientific Computing*, 14(6):1487–1503, November 1993.

[57] P. C. Hansen. The L-curve and its use in the numerical treatment of inverse problems. In P. Johnston, editor, *Computational Inverse Problems in Electrocardiology*, Advances in Computational Bioengineering, pages 119–142. WIT Press, 2000.

[58] H. A. Haroon and G. J. Parker. Using the wild bootstrap to quantify uncertainty in fibre orientations from q-ball analysis. In *Proceedings of the International Society of Magnetic Resonance in Medicine*, page 903, 2007.

[59] R. He, M. Mehta, and P. A. Narayana. Color coding for visualization of the directional information of dti. In *International Conference of the IEEE Engineering in Medicine and Biology Society (IEMBS)*, volume 1, pages 1857–1859, 2004.

[60] E. Hecht. *Optics*. Addison-Wesley, fourth edition, August 2001.

[61] R. Heidemann, A. Anwander, T. Feiweier, C. Eichner, R. Luetzkendorf, J. Bernarding, T. Knösche, and R. Turner. Sub-millimeter diffusion MRI at 7T: Does resolution matter? In *Proceedings of the International Society of Magnetic Resonance in Medicine*, page 1877, 2012.

[62] D. L. G. Hill, P. G. Batchelor, M. Holden, and D. J. Hawkes. Medical image registration. *Physics in Medicine and Biology*, 46:R1–R45, 2001.

[63] M. Hlawitschka and G. Scheuermann. HOT-lines: Tracking lines in higher order tensor fields. In *IEEE Visualization*, pages 27–34, Minneapolis, MN, USA, October 2005.

[64] D. Imperati, I. Frosio, M. Tittgemeyer, and N. A. Borghese. Prediction correction tractography through statistical tracking. In *IEEE Nuclear Science Symposium and Medical Imaging Conference*, pages 4140–4146, October 2009.

[65] S. Jbabdi and H. Johansen-Berg. Tractography: Where do we go from here? *Brain Connectivity*, 1(3):169–183, 2011.

[66] S. Jbabdi, M. W. Woolrich, J. L. R. Andersson, and T. E. J. Behrens. A Bayesian framework for global tractography. *NeuroImage*, 37(1):116–129, August 2007.

[67] G. Jeffery. Architecture of the optic chiasm and the mechanisms that sculpt its development. *Physiological Reviews*, 81(4):1393–1414, October 2001.

[68] B. Jeurissen, A. Leemans, D. K. Jones, J.-D. Tournier, and J. Sijbers. Probabilistic fiber tracking using the residual bootstrap with constrained spherical deconvolution. *Human Brain Mapping*, 32(3):461–479, March 2011.

[69] D. K. Jones and C. Pierpaoli. Confidence mapping in diffusion tensor magnetic resonance imaging tractography using a bootstrap approach. *Magnetic Resonance in Medicine*, 53(5):1143–1149, 2005.

[70] R. C. Jones. A new calculus for the treatment of optical systems. *Journal of the Optical Society of America*, 31(7):500–503, July 1941.

[71] S. J. Julier and J. K. Uhlmann. Unscented filtering and nonlinear estimation. *Proceedings of the IEEE*, 92(3):401–422, March 2004.

[72] E. Jurrus, M. Hardy, T. Tasdizen, T. P. Fletcher, P. Koshevoy, C.-B. Chien, W. Denk, and R. Whitaker. Axon tracking in serial block-face scanning electron microscopy. *Medical Image Analysis*, 13:180–188, 2009.

[73] N. Kang, J. Zhang, E. S. Carlson, and D. Gembris. White matter fiber tractography via anisotropic diffusion simulation in the human brain. *IEEE Transactions on Medical Imaging*, 24(9):1127 –1137, September 2005.

[74] M. Kleiner, M. Axer, D. Gräßel, J. Reckfort, U. Pietrzyk, K. Amunts, and T. Dickscheid. Classification of ambiguous nerve fiber orientations in 3D polarized light imaging. In N. Ayache, H. Delingette, P. Golland, and K. Mori, editors, *Medical Image Computing and Computer Assisted*

Intervention (MICCAI), volume 7510 of *Lecture Notes in Computer Science*, pages 206–213. Springer, 2012.

[75] J. Klingler. Facilitate the macroscopic preparation of the brain through the freezing process [original title: Erleichterung der makroskopischen Präparation des Gehirns durch den Gefrierprozess]. *Schweizer Archiv für Neurologie und Psychiatrie*, 36(2):247–256, 1935.

[76] C. Köbbert, R. Apps, I. Bechmann, J. L. Lanciego, J. Mey, and S. Thanos. Current concepts in neuroanatomical tracing. *Progress in Neurobiology*, 62(4):327–351, November 2000.

[77] M. A. Koch, D. G. Norris, and M. Hund-Georgiadis. An investigation of functional and anatomical connectivity using magnetic resonance imaging. *NeuroImage*, 16(1):241–250, May 2002.

[78] V. Kolmogorov and C. Rother. Minimizing nonsubmodular functions with graph cuts - a review. *IEEE Transactions on Pattern Analysis and Machine Intelligence*, 29(7):1274–1279, July 2007.

[79] V. Kolmogorov and R. Zabih. What energy functions can be minimized via graph cuts? *IEEE Transactions on Pattern Analysis and Machine Intelligence*, 26(2):147–159, February 2004.

[80] B. W. Kreher, I. Mader, and V. G. Kiselev. Gibbs tracking: A novel approach for the reconstruction of neuronal pathways. *Magnetic Resonance in Medicine*, 60(4):953–963, 2008.

[81] L. Larsen and L. Griffin. Can a continuity heuristic be used to resolve the inclination ambiguity of polarized light imaging? In M. Sonka, I. Kakadiaris, and J. Kybic, editors, *Computer Vision and Mathematical Methods in Medical and Biomedical Image Analysis*, volume 3117 of *Lecture Notes in Computer Science*, pages 365–375. Springer, 2004.

[82] L. Larsen, L. D. Griffin, D. Graessel, O. W. Witte, and H. Axer. Polarized light imaging of white matter architecture. *Microscopy Research and Technique*, 70(10):851–863, October 2007.

[83] M. Lazar and A. L. Alexander. Bootstrap white matter tractography (BOOT-TRAC). *NeuroImage*, 24(2):524–532, January 2005.

[84] M. Lazar, D. M. Weinstein, J. S. Tsuruda, K. M. Hasan, K. Arfanakis, M. E. Meyerand, B. Badie, H. A. Rowley, V. Haughton, A. Field, and A. L. Alexander. White matter tractography using diffusion tensor deflection. *Human Brain Mapping*, 18(4):306–321, 2003.

[85] T. B. Leergaard, N. S. White, A. de Crespigny, I. Bolstad, H. D'Arceuil, J. G. Bjaalie, and A. M. Dale. Quantitative histological validation of diffusion MRI fiber orientation distributions in the rat brain. *PLoS ONE*, 5(1):e8595, January 2010.

[86] S. Lienhard, J. G. Malcolm, C.-F. Westin, and Y. Rathi. A full bi-tensor neural tractography algorithm using the unscented kalman filter. *EURASIP Journal on Advances in Signal Processing*, 77:1–10, 2011.

[87] J. Lindemeyer. Rekonstruktion von Nervenfaserverläufen im menschlichen Gehirn. Diploma thesis, University of Wuppertal, 2009. WU D 09-09.

[88] D. G. Lowe. Distinctive image features from scale-invariant keypoints. *International Journal of Computer Vision*, 60(2):91–110, November 2004.

[89] J. G. Malcolm, O. Michailovich, S. Bouix, C.-F. Westin, M. E. Shenton, and Y. Rathi. A filtered approach to neural tractography using the Watson directional function. *Medical Image Analysis*, 14(1):58–69, February 2010.

[90] J. G. Malcolm, M. E. Shenton, and Y. Rathi. Neural tractography using an unscented Kalman filter. In J. L. Prince, D. L. Pham, and K. J. Myers, editors, *Information Processing in Medical Imaging*, volume 5636 of *Lecture Notes in Computer Science*. Springer, July 2009.

[91] J. G. Malcolm, M. E. Shenton, and Y. Rathi. Two-tensor tractography using a constrained filter. In G.-Z. Yang, D. Hawkes, D. Rueckert,

A. Nobel, and C. Taylor, editors, *Medical Image Computing and Computer Assisted Intervention (MICCAI)*, volume 5761 of *Lecture Notes in Computer Science*, pages 894–902. Springer, 2009.

[92] J. G. Malcolm, M. E. Shenton, and Y. Rathi. Filtered multitensor tractography. *IEEE Transactions on Medical Imaging*, 29(9):1664–1675, September 2010.

[93] S. Mori, B. J. Crain, V. P. Chacko, and P. C. van Zijl. Three-dimensional tracking of axonal projections in the brain by magnetic resonance imaging. *Annals of Neurology*, 45(2):265–269, February 1999.

[94] S. Mori and P. C. M. van Zijl. Fiber tracking: principles and strategies - a technical review. *NMR in Biomedicine*, 15(7-8):468–480, November 2002.

[95] E. J. Mufson, D. R. Brady, and J. H. Kordower. Tracing neuronal connections in postmortem human hippocampal complex with the carbocyanine dye DiI. *Neurobiology of Aging*, 11(6):649–653, November 1990.

[96] P. Mukherjee, J. I. Berman, S. W. Chung, C. P. Hess, and R. G. Henry. Diffusion tensor MR imaging and fiber tractography: Theoretic underpinnings. *American Journal of Neuroradiology*, 29(4):632–641, 2008.

[97] L. A. Pajdzik and A. M. Glazer. Three-dimensional birefringence imaging with a microscope tilting-stage. i. uniaxial crystals. *Journal of Applied Crystallography*, 39(3):326–337, June 2006.

[98] C. Palm, M. Axer, D. Graessel, J. Dammers, J. Lindemeyer, K. Zilles, U. Pietrzyk, and K. Amunts. Towards ultra-high resolution fibre tract mapping of the human brain - registration of polarised light images and reorientation of fibre vectors. *Frontiers in Human Neuroscience*, 4(9):1–16, April 2010.

[99] C. Palm, A. Vieten, D. Salber, and U. Pietrzyk. Evaluation of registration strategies for multi-modality images of rat brain slices. *Physics in Medicine and Biology*, 54(10):3269, 2009.

[100] G. Parker, C. Wheeler-Kingshott, and G. Barker. Distributed anatomical brain connectivity derived from diffusion tensor imaging. In M. Insana and R. Leahy, editors, *Information Processing in Medical Imaging*, volume 2082 of *Lecture Notes in Computer Science*, pages 106–120. Springer, 2001.

[101] M. Perrin, C. Poupon, Y. Cointepas, B. Rieul, N. Golestani, C. Pallier, D. Riviere, A. Constantinesco, D. Le Bihan, and J. F. Mangin. Fiber tracking in q-ball fields using regularized particle trajectories. In *Information Processing in Medical Imaging*, volume 3565 of *Lecture Notes in Computer Science*, pages 52–63, 2005.

[102] T. J. Petros, A. Rebsam, and C. A. Mason. Retinal axon growth at the optic chiasm: To cross or not to cross. *Annual Review of Neuroscience*, 31:295–315, 2008.

[103] D. Peuskens, J. van Loon, F. van Calenbergh, R. van den Bergh, J. Goffin, and C. Plets. Anatomy of the anterior temporal lobe and the frontotemporal region demonstrated by fiber dissection. *Neurosurgery*, 55(5):1174, 2004.

[104] J. Pontabry and F. Rousseau. Probabilistic tractography using q-ball modeling and particle filtering. In G. Fichtinger, A. Martel, and T. Peters, editors, *Medical Image Computing and Computer Assisted Intervention (MICCAI)*, volume 6892 of *Lecture Notes in Computer Science*, pages 209–216. Springer, 2011.

[105] V. B. Pujari, H. Jimbo, N. Dange, A. Shah, S. Singh, and A. Goel. Fiber dissection of the visual pathways: analysis of the relationship of optic radiations to lateral ventricle: a cadaveric study. *Neurology India*, 56(2):133–137, 2008.

[106] A. A. Qazi, A. Radmanesh, L. O'Donnell, G. Kindlmann, S. Peled, S. Whalen, C.-F. Westin, and A. J. Golby. Resolving crossings in the

corticospinal tract by two-tensor streamline tractography: method and clinical assessment using fMRI. *NeuroImage*, 47:T98–T106, 2009.

[107] K. Rasband, M. Hardy, and C.-B. Chien. Generating x: Formation of the optic chiasm. *Neuron*, 39(6):885–888, September 2003.

[108] Y. Rathi, O. Michailovich, M. E. Shenton, and S. Bouix. Directional functions for orientation distribution estimation. *Medical Image Analysis*, 13(3):432–444, June 2009.

[109] M. Reisert, I. Mader, C. Anastasopoulos, M. Weigel, S. Schnell, and V. Kiselev. Global fiber reconstruction becomes practical. *NeuroImage*, 54(2):955–962, January 2011.

[110] P. Savadjiev, J. S. W. Campbell, G. B. Pike, and K. Siddiqi. 3D curve inference for diffusion MRI regularization and fibre tractography. *Medical Image Analysis*, 10(5):799–813, October 2006.

[111] P. Savadjiev, Y. Rathi, J. G. Malcolm, M. E. Shenton, and C.-F. Westin. A geometry-based particle filtering approach to white matter tractography. In T. Jiang, N. Navab, J. P. W. Pluim, and M. A. Viergever, editors, *Medical Image Computing and Computer Assisted Intervention (MICCAI)*, volume 6362 of *Lecture Notes in Computer Science*. Springer, 2010.

[112] C. E. Saxer, J. F. de Boer, B. H. Park, Y. Zhao, Z. Chen, and J. S. Nelson. High-speed fiber-based polarization-sensitive optical coherence tomography of in vivo human skin. *Optics Letters*, 25(18):1355–1357, September 2000.

[113] W. J. Schmidt. Doppelbrechung der Markscheide der Nervenfasern. *Zeitschrift für Zellforschung und mikroskopische Anatomie*, 23:657–676, 1935.

[114] R. Schnabel. Zur mikroskopischen Untersuchung optisch anisotroper Strukturen des Nervensystems mit circular polarisiertem Licht. *Acta Neuropathologica*, 7:180–184, 1966.

[115] K K. Seunarine, P. A. Cook, M. G. Hall, K. V. Embleton, G. J. M. Parker, and D. C. Alexander. Exploiting peak anisotropy for tracking through complex structures. In *IEEE International Conference on Computer Vision*, pages 1–8, Rio de Janeiro, Brazil, October 2007.

[116] G. M. Shepherd and C. Koch. *The synaptic organization of the brain*, chapter Introduction to synaptic circuits, page 7. Oxford University Press, third edition, 1990.

[117] A. J. Sherbondy, R. F. Dougherty, M. Ben-Shachar, S. Napel, and B. A. Wandell. ConTrack: Finding the most likely pathways between brain regions using diffusion tractography. *Journal of Vision*, 8(9):15, 1–16, July 2008.

[118] A. J. Sherbondy, M. C. Rowe, and D. C. Alexander. MicroTrack: An algorithm for concurrent projectome and microstructure estimation. In *Medical Image Computing and Computer Assisted Intervention (MICCAI)*, volume 6361 of *Lecture Notes in Computer Science*, 2010.

[119] M. Singh and C.-W. Wong. Independent component analysis-based multifiber streamline tractography of the human brain. *Magnetic Resonance in Medicine*, 64(6):1676–1684, December 2010.

[120] O. Sporns. *Diffusion MRI*, chapter The Human Connectome: Linking Structure and Function in the Human Brain, pages 309–332. Elsevier, 2009.

[121] O. Sporns, G. Tononi, and R. Kotter. The human connectome: A structural description of the human brain. *PLOS Computational Biology*, 1(4):e42, September 2005.

[122] E. O. Stejskal and J. E. Tanner. Spin diffusion measurements: Spin echoes in the presence of a time-dependent field gradient. *Journal of Chemical Physics*, 42:288–292, January 1965.

[123] K. E. Stephan, L. Kamper, A. Bozkurt, G. A. P. C. Burns, M. P. Young, and R. Kötter. Advanced database methodology for the collation of connectivity data on the macaque brain (CoCoMac). *Philosophical*

Transactions of the Royal Society of London. Series B: Biological Sciences, 356(1412):1159–1186, 2001.

[124] R. Szeliski, R. Zabih, D. Scharstein, O. Veksler, V. Kolmogorov, A. Agarwala, M. Tappen, and C. Rother. A comparative study of energy minimization methods for markov random fields with smoothness-based priors. *IEEE Transactions on Pattern Analysis*, 30(6):1068–1080, 2008.

[125] E. Tardif and S. Clarke. Intrinsic connectivity of human auditory areas: a tracing study with DiI. *European Journal of Neuroscience*, 13(5):1045–1050, March 2001.

[126] J.-D. Tournier, S. Mori, and A. Leemans. Diffusion tensor imaging and beyond. *Magnetic Resonance in Medicine*, 65(6):1532–1556, June 2011.

[127] D. S. Tuch, T. G. Reese, M. R. Wiegell, N. Makris, J. W. Belliveau, and V. J. Wedeen. High angular resolution diffusion imaging reveals intravoxel white matter fiber heterogeneity. *Magnetic Resonance in Medicine*, 48(4):577–582, October 2002.

[128] D. S. Tuch, M. R. Wiegell, T. G. Reese, J. W. Belliveau, and V. J. Wedeen. Measuring cortico-cortical connectivity matrices with diffusion spectrum imaging. *Magnetic Resonance in Medicine*, 9:502, 2001.

[129] U. Türe, M. G. Yasargil, A. H. Friedman, and O. Al-Mefty. Fiber dissection technique: lateral aspect of the brain. *Neurosurgery*, 47(2):417, 2000.

[130] M. C. van Turnhout, S. Kranenbarg, and J. L. van Leeuwen. Modeling optical behavior of birefringent biological tissues for evaluation of quantitative polarized light microscopy. *Journal of Biomedical Optics*, 14(5):054018–1 – 054018–11, 2009.

[131] S. K. de Visser de Visser, J. C. Bowden, E. Wentrup-Byrne, L. Rintoul, T. Bostrom, J. M. Pope, and K. I. Momot. Anisotropy of collagen fibre alignment in bovine cartilage: comparison of polarised light microscopy and spatially resolved diffusion-tensor measurements. *Osteoarthritis and Cartilage*, 16(6):689–697, 2008.

[132] R. S. Vorburger, C. Reischauer, and P. Boesiger. BootGraph: Probabilistic fiber tractography using bootstrap algorithms and graph theory. *NeuroImage*, 66(0):426–435, February 2013.

[133] V. J. Wedeen, R. P. Wang, J. D. Schmahmann, T. Benner, W. Y. I. Tseng, G. Dai, D. N. Pandya, P. Hagmann, H. D'Arceuil, and A. J. de Crespignya. Diffusion spectrum magnetic resonance imaging (DSI) tractography of crossing fibers. *NeuroImage*, 41(4):1267–1277, July 2008.

[134] D. Weinstein, G. Kindlmann, and E. Lundberg. Tensorlines: advection-diffusion based propagation through diffusion tensor fields. In *IEEE Visualization*, pages 249–253, San Francisco, CA, USA, October 1999.

[135] G. Welch and G. Bishop. An introduction to the Kalman filter. Technical report, Department of Computer Science. University of Carolina at Chapel Hill, 2006.

[136] D. J. Wu and K. L. Boyer. Markov random field based phase demodulation of interferometric images. *Computer Vision and Image Understanding*, 115(6):759–770, 2011.

[137] X. Wu, Q. Xu, L. Xu, J. Zhou, A. W. Anderson, and Z. Ding. Genetic white matter fiber tractography with global optimization. *Journal of Neuroscience Methods*, 184(2):375 – 379, 2009.

[138] P.-T. Yap, J. H. Gilmore, W. Lin, and D. Shen. Longitudinal tractography with application to neuronal fiber trajectory reconstruction in neonates. In *Medical Image Computing and Computer Assisted Intervention (MICCAI)*, volume 6892 of *Lecture Notes in Computer Science*, pages 66–73, 2011.

[139] F. Zhang, E. R. Hancock, C. Goodlett, and G. Gerig. Probabilistic white matter fiber tracking using particle filtering and von Mises-Fisher sampling. *Medical Image Analysis*, 13(1):5–18, February 2009.

[140] L. Zhukov and A. H. Barr. Oriented tensor reconstruction: Tracing neural pathways from diffusion tensor MRI. In *IEEE Visualization*, pages 387 – 394, Boston, MA, USA, October 2002.